Corrosion Behaviour of Advanced Fe-Based Bulk Metallic Glasses

Dissertation

zur Erlangung des akademischen Grades

Doktoringenieur (Dr.-Ing.)

vorgelegt

der Fakultät Maschinenwesen

der Technischen Universität Dresden

von

Petre Flaviu Gostin

geb. am 29.06.1981

in Bukarest, Rumänien

1. Gutachter: Prof. Dr. Ludwig Schultz
2. Gutachter: Prof. Dr. Jürgen Eckert

Tag der Verteidigung: 08.04.2011

Date of defence: 08 April 2011

The members of the thesis committee:
Prof. Dr.-Ing. Christoph Leyens
Prof. Dr. rer. nat. Ludwig Schultz
Prof. Dr.-Ing. Jürgen Eckert
PD Dr. Ing. habil. Oliver Gutfleisch
Prof. Dr.-Ing. habil. Rüdiger Lange

Abstract

Early developed non-bulk Fe-based glasses, e.g. Fe-Cr(-Mo)-metalloid(s), exhibit extraordinary corrosion resistance, but low glass formation ability (GFA). Newly developed bulk glass-forming Fe-based alloys have on the contrary high GFA, but also very different compositions and therefore their corrosion behaviour is expectedly not similar. Fundamental investigations regarding corrosion behaviour were performed for one of the most prominent bulk glassy alloy, namely $(Fe_{44.3}Cr_5Co_5Mo_{12.8}Mn_{11.2}C_{15.8}B_{5.9})_{98.5}Y_{1.5}$. Particularly, the free corrosion and the anodic polarization behaviour, the passivation ability and the pitting susceptibility have been assessed in electrolytes with varying pH values and anion species concentrations. Due to its monolithic single phase microstructure this alloy has a much lower corrosion rate in acids than a two-phase conventional steel (DIN X210Cr12) with much higher content of passivating Cr, i.e. 11.4 at. %. However, the high concentration of electrochemically active Mn and B as well as the unfavourably high Mo to Cr concentration ratio determine a higher corrosion rate of this bulk glassy alloy in strong alkalis and also a very poor passivation ability in acids. On the contrary, the high content of Mo has a positive influence on the pitting resistance by inhibiting very effectively the propagation of pits occurring at Y_2O_3 inclusions. Detailed microscopic analysis investigations by HRSEM and in-situ AFM revealed the formation of characteristic morphological features at the micro- and nanometre scale on the surface of samples exposed to acidic solutions. These were explained by selective dissolution of active elements, e.g. Mn, B. This study demonstrated the necessity to investigate the corrosion properties of newly developed bulk glass-forming Fe-based alloys - they are not per-se highly corrosion resistant, but their corrosion behaviour depends on their particular chemical composition.

Kurzfassung

Früh entwickelte, nicht-massive amorphe Eisenbasislegierungen, z.B. Fe-Cr(-Mo)-Metalloid(e), zeigen bemerkenswerte Korrosionsbeständigkeit, aber niedrige Glasbildungsfähigkeit (englisch: glass-forming ability, GFA). Neu entwickelte massiv-glasbildende Eisenbasislegierungen haben im Gegenteil eine höhere GFA, aber auch sehr unterschiedliche Zusammensetzungen und deshalb ist ihr Korrosionverhalten wie zu erwarten nicht änlich. Grundlegende Untersuchungen des Korrosionsverhaltens einer der bekanntesten massiven amophen Legierung, nämlich $(Fe_{44.3}Cr_5Co_5Mo_{12.8}Mn_{11.2}C_{15.8}B_{5.9})_{98.5}Y_{1.5}$, wurden

vorgenommen. Insbesondere wurde das Augenmerk auf das freie Korrosions- und das anodische Polarisationsverhalten, die Passivierungseigenschaften und die Anfälligkeit gegenüber Lochfraß in Elektrolyten mit verschiedenen pH-Werten und Anionenkonzentrationen gerichtet. Aufgrund ihres einphasig monolitischen Gefüges zeigt diese Legierung in Säuren eine viel niedrigere Korrosionsgeschwindigkeit als die eines zweiphasigen herkömmlichen Stahls (DIN X210Cr12) mit viel höherem Gehalt an passivierendem Cr, d.h. 11.4 at. %. Der höhere Gehalt an electrochemisch aktivem Mn und B sowie das nachteilige Verhältnis von Mo zu Cr Konzentration sind für eine höhere Korrosionsgeschwindigkeit dieser massiven amorphen Legierung in konzentrierten Alkalien sowie eine geringere Passivierungsfähigkeit in Säuren verantwortlich. Der hohe Gehalt an Mo hat jedoch einen positiven Einfluss auf die Lochfraßbeständigkeit - er hindert sehr wirksam das Wachstum der an Y_2O_3-Einschlüssen gebildeten Löcher. Detaillierte mikroskopische Untersuchungen durch HRSEM und in-situ AFM zeigten die Bildung charakteristischer Morphologien im Mikrometer- und Nanometerbereich auf der Oberfläche von Proben, die starken Säure ausgesetzt waren. Dieses wurde durch selektive Auflösung aktiver Elemente, z.B. Mn, B, erklärt. Diese Arbeit unterstreicht die Notwendigkeit, die Korrosionseigenschaften der neu entwickelten, massivglasbildenden Eisenbasislegierungen zu untersuchen - diese sind nicht per-se ‘hochkorrosionsbeständig’, stattdessen hängt ihr Korrosionsverhalten vielmehr von ihrer besonderen chemischen Zusammensetzung ab.

Contents

1 Introduction

Fe-based bulk metallic glasses (BMGs) are regarded as having a high potential for industrial applications due to the high availability and relatively low cost of the main alloying element, Fe, and their outstanding properties, e.g. high strength, elastic modulus and hardness, in part very good magnetic properties, and expected high corrosion resistance, which are not achievable by conventional crystalline alloys [1–6]. Recently, their previous size limitation has been greatly overcome by the discovery, that minor additions of rare earth elements significantly improve their glass formation ability (GFA) [1, 7, 8]. Furthermore, by adding small amounts of rare earth elements, commercial raw materials and low vacuum conditions (even air atmosphere) may be used to successfully fabricate some Fe-based bulk glassy alloys [7, 9–12]. These practical advantages contribute to further lowering of the costs of these alloys [13]. However, limited environmental stability can dramatically determine the applicability of any material, but this aspect was so far scarcely assessed for this new class of Fe-based bulk glassy alloys. One of the most prominent examples at the time of beginning of this work (2007), $(Fe_{44.3}Cr_5Co_5Mo_{12.8}Mn_{11.2}C_{15.8}B_{5.9})_{98.5}Y_{1.5}$, also entitled as 'structural amorphous steel', was chosen to fundamentally study the corrosion behaviour. This glassy alloy with maximum sample thickness of 12 mm has high thermal stability ($T_g = 804\,\mathrm{K}$), high strength (~ 3 GPa) and hardness (1224 HV), and is non-ferromagnetic at ambient temperatures ($T_c = \sim 55\,\mathrm{K}$) [1].

In the early days of amorphous metals, a large number of research studies had been devoted to the development of Fe-based amorphous alloys with excellent corrosion-resistant properties [14]. It was especially observed that several of those can exhibit corrosion resistance superior to that of stainless steels. For example, exceptional resistance was demonstrated for amorphous Fe-Cr-Mo-metalloid alloys with distinct compositions which passivate spontaneously even in hot concentrated hydrochloric acid [14] or Fe-Ni-Cr-Mo-B alloys which exhibit excellent passivation behaviour in acid solutions up to 250°C [15]. But this first generation of amorphous Fe-based alloys possessed only low glass forming ability and thus, could be obtained only as thin or small products e.g. ribbons, foils, flakes, powders or films. In order to overcome the size limitation of this first generation, the second generation of alloys that are bulk glass-formers was recently developed. However, most of them were predominantly designed for attaining other properties, e.g. for combining high GFA and excellent mechanical

performance, rather than for corrosion resistance. Therefore, these alloys have substantially different compositions compared to earlier ones, e.g. they contain reactive Mn, and have usually lower concentrations of beneficial Cr and P [16]. Although those compositional variations are expected to have quite a critical influence on long term stability under applicative conditions, the corrosion behaviour of bulk glassy Fe-based alloys has been scarcely studied so far. The global aim of this work was to fundamentally analyze the corrosion behaviour of the bulk glassy $(Fe_{44.3}Cr_5Co_5Mo_{12.8}Mn_{11.2}C_{15.8}B_{5.9})_{98.5}Y_{1.5}$ alloy in different aqueous environments at room temperature. More specifically, the following aspects have been considered: free corrosion, anodic polarization behaviour, passivation ability and pitting susceptibility. Additionally, as explained in the next two paragraphs, some more detailed investigations were performed.

Ideally, amorphous alloys are regarded as being structurally and chemically homogeneous, i.e. they are free from secondary phases or inclusions which could initiate galvanic or localized corrosion processes [17]. However, in practice the presence of defects in cast samples can not be completely avoided, at least in commercial production. Not surprisingly, several studies revealed that some BMGs have high pitting susceptibility and pits are initiated at the interface between such defects and the surrounding matrix [18]. Furthermore, amorphous alloys can be regarded as single-phase solid solutions, often exceeding the solubility limits of alloying elements at equilibrium. Obviously, this characteristic yields differences in their behaviour compared to equilibrium crystalline alloys. Also, their higher concentration of metalloids compared to conventional crystalline alloys can significantly alter their corrosion behaviour, depending on the nature of the metalloids and on the other constituent elements of the alloy [19]. Therefore, in order to identify the corrosion performance of a glassy alloy clearly, a direct comparison to that of relevant crystalline states is indispensable. The following aspects were considered for comparison: anodic polarization behaviour, passivation ability and pitting behaviour.

For classical crystalline metals and alloys, the morphology of corroded surfaces is strongly influenced by structural factors such as crystal orientation, grain boundaries, precipitates etc. The surface morphology is determined by locally varying corrosion rates. Sites which are corroding at a higher rate will appear as valleys, while those corroding at a lower rate will appear as hills. Depending on their orientation, grains of polycrystalline alloys have different corrosion rates. Grain boundaries and precipitates can also exhibit different corrosion rates [20]. In addition to determining the morphology of corroding surfaces, heterogeneities in the material are often recognized as preferential sites for initiation of corrosion, especially pitting corrosion [21]. Contrary to crystalline alloys, amorphous alloys are principally missing those structural particularities and therefore, they are thought as chemically and structurally homogeneous materials. The questions arise then: how is an active corrosion process on the surface of such a homogeneous amorphous alloy initiated and how does the morphology of such a corroding

surface evolve? In order to analyze this, morphological studies by using in-situ and ex-situ observation techniques are required. Only few such studies have been reported for metallic glasses so far. For example, Green et al. [22] studied in-situ the initial stages of pitting on $Zr_{50}Cu_{40}Al_{10}$ surfaces with the help of optical microscopy. In another study, Wang et al. [23] used atomic force microscopy (AFM) to characterize and compare the morphology of amorphous and crystalline $Ni_{50}Nb_{50}$ surfaces in order to understand the breakdown of passive films. In the case of Fe-based glasses, observations of morphology evolution of corroded surfaces have been limited to ex-situ SEM investigations of alloy surfaces mainly subjected to pitting or crevice corrosion [24–30]. In a separate chapter, it will be demonstrated, based on newly established in-situ AFM studies, that active dissolution reactions yield characteristic morphological features of the glassy alloy surface on the micro- and nanometre scale.
This way a comprehensive description of the active dissolution behaviour, the passivation ability and the pitting behaviour of this new bulk-glass forming Fe-based alloy will be given and the underlying reaction mechanisms will be discussed. This case study allows to draw some generalized conclusions of the principal corrosion activity of new Fe-based BMGs – and problems related to that – and to evaluate their corrosion performance and application potential as long term stable engineering material in comparison to conventional Fe-based alloys.

2 Theoretical background

2.1 Metallic glasses

2.1.1 Fundamental considerations on glass formation

Crystalline alloys are characterized by an ordered arrangement of atoms which extends much beyond one unit cell. It is therefore said to have short, medium and long range order (SRO, MRO and LRO). When a crystalline alloy melts, it loses its LRO and usually the packing of atoms becomes less dense and the mobility of atoms increases. Correspondingly, the volume is higher while the viscosity is lower in the liquid state than in the solid crystalline state. In the case of pure metals, the variation of these properties with temperature as well as of other properties such as enthalpy and entropy is discontinuous [31]. Above the melting temperature, the liquid is in a state of equilibrium. When cooled, the liquid will crystallize again after it undercooled below the equilibrium crystallization temperature necessary to overcome the energy barrier for formation of nuclei. Properties such as volume and viscosity will vary discontinuously upon crystallization as shown in Fig. 2.1. However, some metallic melts, if cooled rapidly enough, will not undergo crystallization, but instead they will freeze in a liquid-like structural state known as amorphous or glassy state. In this case, as the liquid is cooled to lower and lower temperatures, the driving force for nucleation is continuously increasing while the mobility of atoms is continuously decreasing which is reflected in the continuous increase of viscosity as shown in Fig. 2.1(b). The decrease in mobility accompanies a decrease of free volume of the liquid which is reflected by a continuous decrease of volume as shown in Fig. 2.1(a). Below the equilibrium melting temperature, the liquid – now called *supercooled liquid*, is no longer in stable equilibrium, but in metastable equilibrium. If crystallization is prevented long enough, the liquid will eventually 'freeze'. In this regime, the temperature dependence of volume and viscosity will change its trend (Fig. 2.1). Conventionally, it is considered that the undercooled melt becomes a *glass* when its viscosity reaches the value of 10^{12} Pa·s. Below this freezing regime, called *the glass transition*, the structure remains virtually unchanged and volume and viscosity depend only slightly on temperature. The glass transition does not take place at a distinct temperature, but in a temperature interval called *glass transition range*. The *glass transition temperature*, T_g, is determined by the intersection

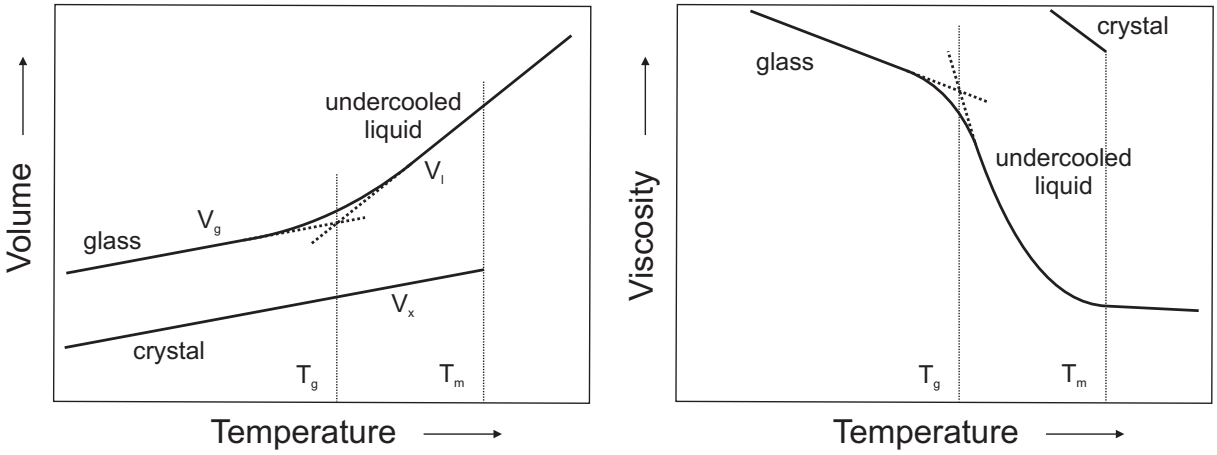

Figure 2.1: Dependency of (a) volume and (b) viscosity of an alloy in the undercooled liquid, glassy and crystalline states.

point of the extrapolated dependencies of some properties, e.g. volume, in the undercooled liquid region and in the glass region as shown by the dotted lines in Fig. 2.1(a). T_g is not a thermodynamically defined temperature and it depends on the cooling rate. The higher the cooling rate is, the higher the T_g value will be. According to Fig. 2.1(a) it is deduced that the volume of the glass, V_g, will be higher when produced with a higher cooling rate and more free volume remains trapped in the atomic structure. This means that also the final structural state of the glass depends on the cooling rate. It also results that the glass does not have a fixed free enthalpy, but this depends also on the cooling rate. The glass will then tend to release the extra-energy that it stored and achieve a reference glassy state which has minimum energy. This reference glassy state corresponds to the minimum cooling rate for which the undercooled liquid can be vitrified.

2.1.2 Glass forming ability of metallic alloys

The ability of an alloy to be obtained in a glassy state during undercooling of a melt is called *the glass forming ability* (GFA). It results from the discussion in section 2.1.1 that the ability to form a glass is higher, the more the undercooled liquid is stabilized against crystallization. From a fundamental perspective, this can be analyzed under severals aspects which are addressed in the following.

Thermodynamic aspects Figure 2.2 shows a schematic representation of the temperature dependence of the free enthalpy for a liquid alloy (L) and for the corresponding crystalline solid (S). Upon cooling the liquid alloy, it will solidify as a crystalline solid at the melting

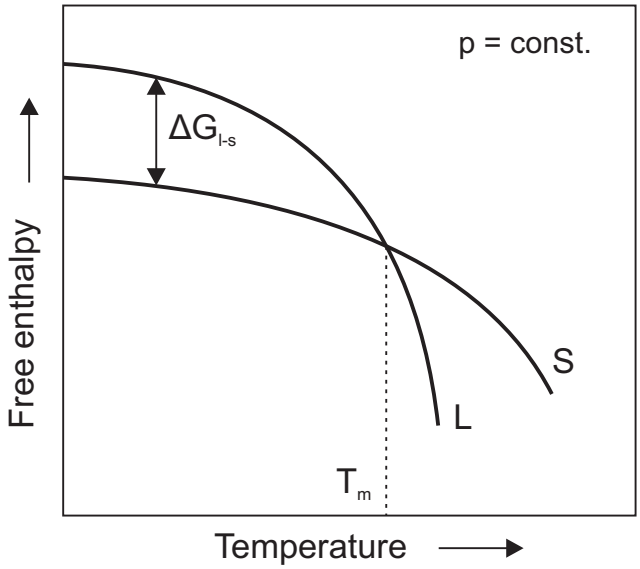

Figure 2.2: Schematic representation of free enthalpy of the liquid and crystalline solid states in dependence of temperature at constant external pressure.

temperature T_m. With further decrease of temperature the free enthalpy will follow curve S. However, for some conditions e.g. rapid cooling, the liquid state of the alloy will persist at temperatures below the melting temperature (the undercooled liquid state). This state has a higher energy than the crystalline state. Therefore the system naturally tends to achieve the crystalline state. In order to prevent this and to maintain the undercooled liquid state to lower temperatures, the driving force for crystallization ΔG_{l-s} must be low. As the temperature of the system decreases, the undercooled liquid will eventually freeze in a solid glassy state as explained in section 2.1.1. In conclusion, it is more favourable to have lower ΔG_{l-s} for achieving higher undercooling and therefore high GFA. By definition, $\Delta G_{l-s} = \Delta H_f - T \cdot \Delta S_f$, where ΔH_f is the enthalpy of fusion and ΔS_f is the entropy of fusion. It results that ΔG_{l-s} is small when ΔH_f is small and ΔS_f is large. ΔH_f is low for low melting temperatures and therefore, for compositions at and close to deep eutectics. ΔS_f is high for alloys with many constituent elements.

Kinetic aspects Crystallization takes place by crystal nucleation followed by crystal growth. In order to minimize the tendency for crystallization and therefore, increase the GFA, the rate of nucleation should be low. Turnbull [32] derived an equation for the nucleation rate, I, in the case of homogeneous nucleation from an undercooled melt assuming identical composition of melt and nuclei and spherical shape of nuclei:

$$I = \frac{k}{\eta} \exp \frac{-b\alpha^3\beta}{T_r(\Delta T_r)^2} \qquad \text{eq. (2.1)}$$

where k is a kinetic constant, η is the viscosity of the undercooled melt, b is a geometric constant, α and β are parameters related to the solid/liquid interfacial energy γ_{s-l}, and to the entropy of fusion S_m, respectively, T_r is the reduced temperature $\frac{T}{T_m}$, and ΔT_r is the reduced undercooling $\frac{T_m - T}{T_m}$. When the term $\alpha^3\beta$ is large, the nucleation rate, I, will be low. This is so when the interfacial energy, γ_{s-l}, is large, the fusion enthalpy, δH_f, is low and the fusion entropy, δS_m, is large. It also results from eq. (2.1) that the higher the undercooling is, the higher the nucleation rate and therefore, the tendency for crystallization. Finally, the nucleation rate I depends on the viscosity of the undercooled melt, η, which changes dramatically during undercooling. In accordance with eq. (2.1), if the viscosity of the undercooled melt, η, is high, the tendency for nucleation is lower and therefore, the GFA is high.
Another way of expressing the kinetics of glass formation is with the help of time-temperature-transformation (TTT) diagrams which are determined isothermally or with the help of continuous-cooling-transformation (CCT) diagrams. Such a diagram is shown schematically in Fig. 2.3. When a melt is cooled below the melting temperature, T_m, it becomes an undercooled melt as shown in Fig. 2.3. This domain is limited on the right-hand side by the *crystallization 'nose'*, which limits at its left-hand side the domain of crystalline phases. In order to prevent crystallization, the cooling has to be done as fast as to avoid intersecting the cooling curve with the domain for crystalline phases. Depending on the position of the *crystallization nose* with respect to the time axis, the required cooling rates for preventing crystallization can be very different. The more the nose is shifted to longer time scales, the higher is the GFA. Glassy alloys of the first generation require very high cooling rates, e.g. 10^6 K/s, and are produced by *rapid quenching* techniques, while new bulk glass formers do

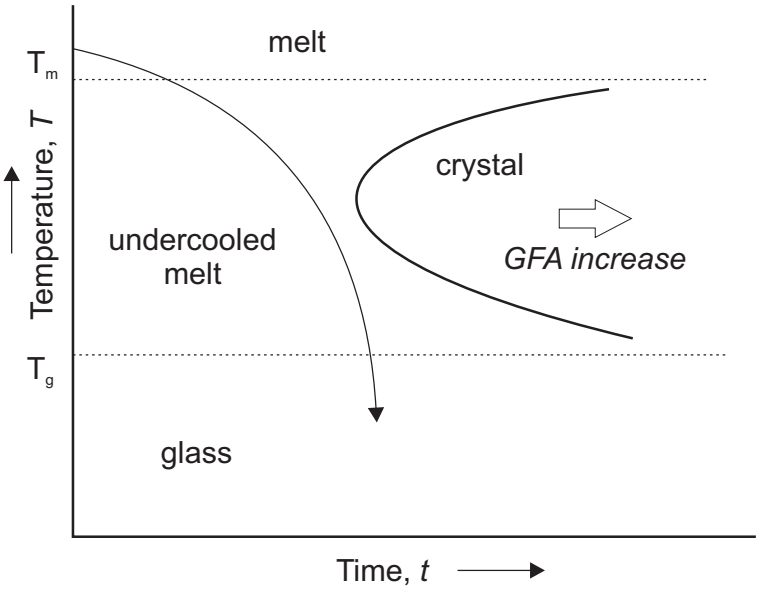

Figure 2.3: Schematic TTT/CCT diagram with cooling curve.

not require very high cooling rates, e.g. 1 K/s, and can be produced by slow cooling like Cu mould casting.

Structural aspects As stated in section 2.1.1 the atomic arrangement of a glass is similar to that of the undercooled melt. It was stated by several authors that in order to stabilize this arrangement and to prevent rearrangements to an ordered crystalline structure, size mismatches between the constituent atoms over certain values are necessary. Actually, Cahn and Greer stated that the atomic size is the single factor that plays the major role in determining GFA [33]. Already in the sixties, it was discovered that a sufficient atomic size mismatch is necessary for preventing the formation of a crystalline structure [34]. A critical value of ∼15% was found to fit the results [33]. This value was later confirmed by Simpson and Hodkinson in their simulation study [35]. Calculations of the microscopic stress level at the scale of individual atom groups in dependence of solute concentration showed that, while the strain energy in a crystalline phase increases steadily with solute concentration, it does not vary much in a glass [33]. It was concluded that beyond a critical solute content, a glassy phase would be more favourable than a crystalline one. Another approach takes into consideration the free volume which supports atomic motion. Therefore, the less free volume is present in the undercooled melt, the least atomic motion takes place which is necessary for crystal growth. Thus, according to Yavari [36], if the volume change during melting is low, the melt contains little free volume and consequently, the GFA is higher.

Empirical rules Stabilization of the supercooled liquid state to the disadvantage of crystalline phases, meaning higher GFA, involves, according to a summary of Inoue [37], *three empirical rules*: (i) the alloy has to be multi-component consisting of more than three elements, (ii) significant atomic size mismatches of over ∼12 % among the main three elements, and (iii) negative heats of mixing among the main three elements.

GFA criteria High GFA ability enables a glass to be formed from the melt with a relatively slow cooling rate. However, as explained above, if the melt cools too slowly crystallization occurs. The minimum cooling rate for which a glass can still be obtained is called *critical cooling rate* R_c. It follows that the lower the critical cooling rate, R_c, the larger is the thickness of a glassy sample that could be obtained. The largest thickness of the sample that is still glassy is called *maximum sample thickness*, D_{max}. However, using two parameters for evaluating GFA in the empirical search for new alloy compositions with high GFA is a lengthy and costly way because it requires several casting trials with various cooling rates. Therefore, to quantify the GFA several criteria derived from the thermal properties of known systems have been proposed [38]. The most frequently used criteria are: (i) the reduced glass transition

temperature, $T_{rg} = T_g/T_l$, (ii) the supercooled liquid range, $\Delta T_x = T_x - T_g$, and (iii) the parameter $\gamma = T_x/(T_g + T_l)$, where T_g, T_x, and T_l are the glass transition temperature, the onset of crystallization temperature and the liquidus temperature, respectively. The higher the reduced glass transition temperature T_{rg} is, the higher is the GFA. The value of this parameter takes values in the interval 0.4–0.7 for known metallic glasses [39]. For bulk glass forming alloys, defined as having a D_{max}>1 mm, T_{rg} is >0.5. A high ΔT_x simply means a higher resistance of a glassy state/undercooled liquid to crystallization. Typical values for recent Fe-based BMGs are in the interval 40–50 K [38]. However these two criteria, T_{rg} and ΔT_x, are limited in thoroughly expressing the GFA. The T_{rg} criterion reflects the formation conditions of a glass, but not the thermal stability of that glass. On the contrary, the ΔT_x criterion considers only the thermal stability, but not the formation conditions. The γ-parameter instead considers both these aspects. Typical γ values for BMGs are in the interval 0.35–0.5. Table 2.1 shows exemplarily the values of these three parameters for several BMGs including some Fe-based alloys. It can be seen that the Fe-based BMGs together with the Co-based ones have the highest T_g and T_x values meaning that they are stable and can be used in a larger temperature interval. However, Fe-based BMGs do not have the best GFA, e.g. they have lower D_{max} values than some Pd- and Zr-based BMGs and lower T_{rg} and γ values than most of the other BMG systems. Their resistance to crystallization expressed by ΔT_x can be classified as average.

Table 2.1: Values of the three criteria, T_{rg}, ΔT_x and γ, for selected BMGs [38].

Alloy composition	T_g, K	T_x, K	T_l, K	D_{max}, mm	T_{rg}	ΔT_x, K	γ
$Cu_{50}Zr_{43}Al_7$	721	792	1176	4	0.6131	71	0.4175
$Mg_{58.5}Cu_{30.5}Y_{11}$	422	496	762	9	0.5538	74	0.4189
$La_{62}Cu_{12}Ni_{12}Al_{14}$	423	452	744	12	0.5686	29	0.3873
$Pd_{40}Cu_{30}Ni_{10}P_{20}$	577	656	836	72	0.6901	79	0.4642
$Ti_{50}Zr_{15}Cu_9Ni_8Be_{18}$	622	662	1009	6	0.6165	40	0.4059
$Co_{48}Cr_{15}Mo_{14}C_{15}B_6Er_2$	848	933	1394	10	0.6083	85	0.4162
$Zr_{41.2}Ti_{13.8}Cu_{12.5}Ni_{10}Be_{22.5}$	623	672	996	50	0.6255	49	0.4151
$[(Fe_{0.5}Co_{0.5})_{0.75}B_{0.2}Si_{0.05}]_{96}Nb_4$	820	870	1397	5	0.5870	50	0.3924
$Fe_{41}Co_7Cr_{15}Mo_{14}C_{15}B_6Y_2$	838	875	1436	16	0.5836	37	0.3848
$Fe_{48}Cr_{15}Mo_{14}C_{15}B_6Er_2$	844	880	1446	8	0.5837	36	0.3843
$Fe_{65.5}Cr_4Mo_4Ga_4P_{12}C_5B_{5.5}$	745	806	1322	3	0.5635	61	0.3899
$(Fe_{44.3}Cr_5Co_5Mo_{12.8}Mn_{12}C_{15.8}B_{5.9})_{98.5}Y_{1.5}$	813[a]	861[a]	1410[a]	12[b]	0.5766	48	0.3873

[a] From Ref. [40]. [b] From Ref. [1]

2.1.3 Structure of metallic glasses

The atomic arrangement of metallic glasses does not exhibit any long range order (LRO) with translational symmetry as it is characteristic for conventional crystalline materials. However, they do have short- to medium-range ordered states (SRO, MRO). SRO develops over the first coordination shell in distance which is usually <0.5 nm. MRO refers to over-next neighbour arrangements and extends further to distances of over 1 nm [41]. In the case of a monolithic glass, the SRO and MRO control its properties, such as the initiation of plastic flow. Understanding how the atoms are packed in metallic glasses is not straightforward. Initially, structural models were proposed in order to describe the arrangement of atoms in metallic glasses. However, these models, like Bernal's dense random packing of hard spheres [42] or Gaskell's model based on trigonal prismatic structural units [43], have many limitations and are now regarded as unsatisfactory. The present understanding is that, at the atomic level, glasses are organized in cluster-like structural units [44, 45]. These are geometrically different, not identical in topology. Although there are more possibilities for the geometry of these 'clusters' (topological SRO), their chemical order is clearly defined, namely they are centred in a solute atom. As an example, Fig. 2.4 shows the packing of several neighbouring solute-centered quasi-equivalent clusters sharing one or more atoms for three metallic glasses. It can be seen that although the various clusters are topologically different, they all have a solute atom at the center.

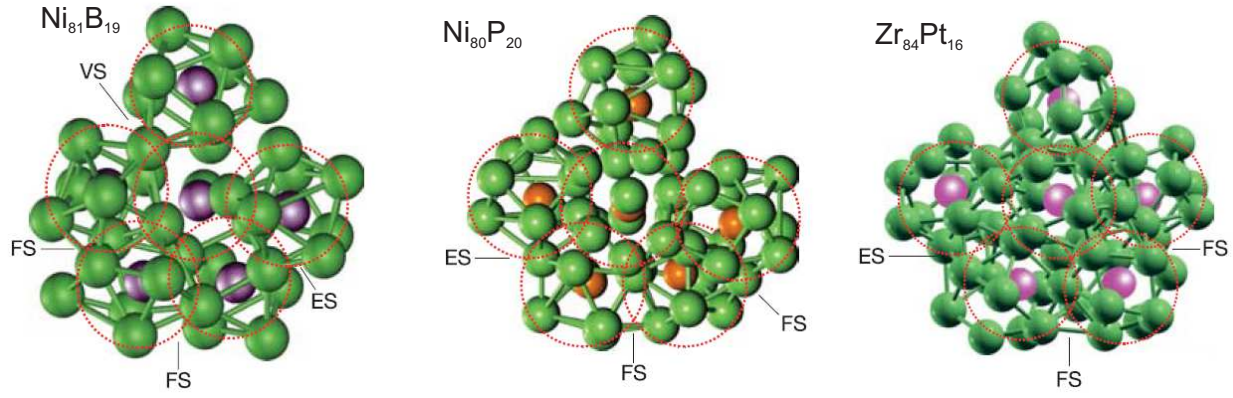

Figure 2.4: The packing of the solute-centred quasi-equivalent clusters in $Ni_{81}B_{19}$, $Ni_{80}P_{20}$ and $Zr_{84}Pt_{16}$. FS, ES and VS denote face-sharing, edge-sharing and vertex-sharing, respectively. The red dashed circles delineate the clusters [44].

Going further, in the medium-range scale, these quasi-equivalent clusters form a superior level packing giving rise to MRO. There is not yet complete agreement on the type of packing of clusters in metallic glasses. For example, for systems with icosahedral SRO units, e.g. Zr-based, Miracle proposed f.c.c and h.c.p. MRO packing [45], while Sheng et al. stated that an icosahedral packing of SRO clusters is more favourable [44].

According to Inoue [5], the atomic configurations differ among the metal-metal, metal-metalloid and Pd-metalloid type alloys. The glassy structure in the case of metal-metal type glasses in Zr-, Hf- and Ti-based systems is composed of icosahedral clusters, while the metal-metalloid-type glassy alloys in Fe-TM(Ln)-B and Co-TM-B (TM = Zr, Hf, Nb, Ta) systems have a long-range network-like structure consisting of trigonal prisms [39]. As shown in Fig. 2.5, the trigonal prisms that form the network-like structure are connected densely with each other in an edge-sharing mode through multi-bonding atoms of TM or Ln. The atomic arrangement of metal-metalloid type glasses is addressed here in more detail since the alloy studied in this work is of this type. One of the first studies in this regard

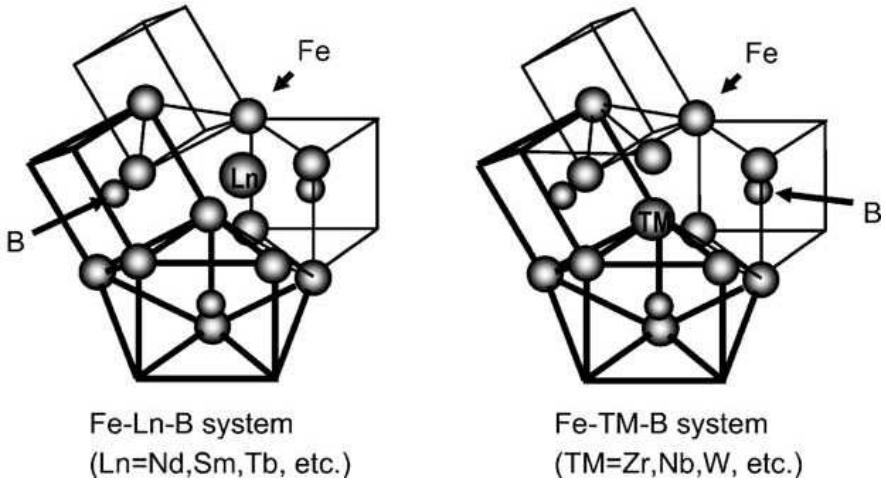

Figure 2.5: Schematic illustration of atomic configurations in Fe-Ln-B and Fe-TM-B (TM = Zr, Hf, Nb, Ta) glassy alloys [39].

was conducted by Gaskell [43], who proposed an atomic structural model based on trigonal prismatic units which have a metalloid atom at the centre and six metal atoms at the vertices. Further, these units are connected randomly sharing edges. This structure is similar to that of crystalline borides, carbides, phosphides and silicides which form when typical metal-metalloid glasses are provoked to crystallize. This is an argument which sustains the validity of this model. However, since that time compositions of metal-metalloid glasses have become increasingly more complex and therefore, more evolved descriptions than Gaskell's model were required. Nakamura et al. [46], investigated the structure of $Fe_{70}M_{10}B_{20}$ (M = Cr, W, Nb, Zr and Hf) amorphous alloys by X-ray diffraction, anomalous X-ray scattering and extended X-ray absorption fine structure, and concluded that the local atomic structure consists of similar structural units as in Gaskell's model. B atoms sit at the centre of the prisms and Fe atoms sit at the vertices while M atoms replace some of the Fe atoms. Another study focused on the more complex alloy composition $Fe_{70\text{-}x}Co_{10}Ln_xB_{20}$ (x = 0 and 3, Ln = Sm, Tb and Dy) [47]. This study agrees on the trigonal prism-like ordering proposed by Nakamura et al. for the $Fe_{70}M_{10}B_{20}$ glasses. However, it was additionally stated that the Ln

atoms determine a disordering of the larger range network formed by these prisms. The Ln atoms are expected to sit between the prisms, but further experimental studies regarding especially the neighborhood of Ln atoms are required to clarify this. Experimental structural studies of the more recent bulk metallic glasses like the one studied in this work are very difficult because of their high number of component elements. A simplified application of the present knowledge of the atomic structure of metal-metalloid glasses to the bulk glassy $(Fe_{44.3}Cr_5Co_5Mo_{12.8}Mn_{11.2}C_{15.8}B_{5.9})_{98.5}Y_{1.5}$ alloy would give the following: the structure is formed of trigonal prisms which have Fe, Cr, Co, Mo and Mn at their vertices, C or B atoms at the centre and neighboring prisms share edges to form a network-like structure while Y atoms sit between the prisms. Having a principle idea about the atomic structure of the glass under investigation is an important prerequisite for the explanation of corrosion phenomena at the nanoscale as it will be demonstrated at the end of this work.

2.1.4 Properties of metallic glasses

As shown in section 2.1.3, amorphous alloys have unique structural features. Additionally, they have unusual compositions with constituent concentrations often beyond the solubility limits of the related crystalline phases. It is therefore expected, and this is actually the case, that they exhibit unusual properties. In the following, thermal, mechanical and soft magnetic properties are addressed. Their corrosion behaviour is considered in more detail in a separate section (see section 2.2).

Thermal behaviour Upon continuous heating, metallic glasses exhibit a reverse of undercooling events which took place during their formation (see section 2.1.1). One experimental method frequently used to study the thermal behaviour of metallic glasses is differential scanning calorimetry (DSC). In this experiment the sample is continuously heated with a given rate and the difference in the amount of heat required to increase the temperature of the sample and that of a reference sample is measured as a function of temperature. In this way, endo- and exothermic events can be detected. Figure 2.6 shows a schematic DSC curve for a metallic glass. An endothermic event sets in at a certain temperature regime which is attributed to the glass transition into the state of an undercooled melt. The mostly considered onset temperature is a characteristic temperature and it is called the glass transition temperature T_g. The undercooled liquid state will be stable until crystallization will occur which is marked in the DSC curve by an exothermic event, as seen in Fig. 2.6, starting at the onset temperature T_x. Crystallization may take place sequentially meaning that more crystalline phases are formed and this is marked by the presence of more exothermic peaks in the DSC curve. Nevertheless, a single peak does not mean that a single crystalline phase was crystallized. One peak can correspond to the crystallization of more phases. The temperature range

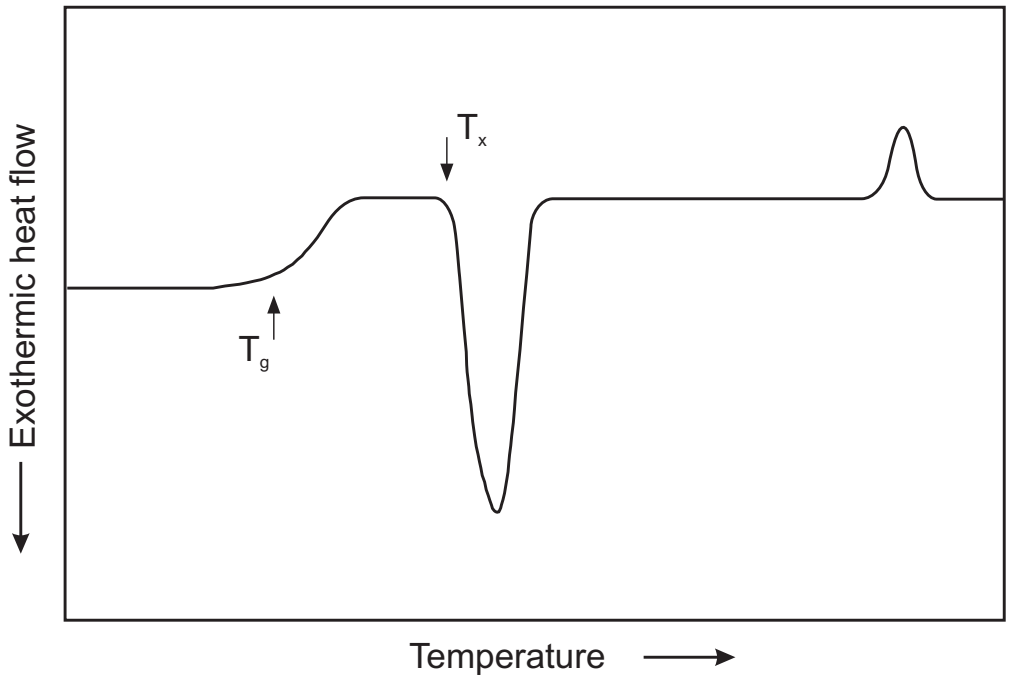

Figure 2.6: Schematic DSC curve for a metallic glass.

in which the undercooled liquid state is present is called the supercooled liquid region and is usually denoted by the symbol ΔT_x ($\Delta T_x = T_x - T_g$). A large ΔT_x value can mean that the undercooled liquid state is highly resistant against crystallization which in turn indicates a high GFA (see section 2.1.1). Further heating of the metallic glass leads to its melting which is detectable in the DSC curve as one or more endothermic peak(s) (Fig. 2.6). This knowledge of the thermal behaviour of metallic glasses can be utilized, e.g. for the development of BMG composites with crystalline phase(s) formed by heat treatment of the BMG, for thermoplastic forming of BMG samples on the macro- and microscale utilizing the softening effect which occurs in the supercooled liquid regime [48].

Mechanical properties Metallic glasses exhibit a very different mechanical behaviour depending on their viscosity which in turn depends on temperature as explained in 2.1.1. While at temperatures below the glass transition temperature ($T < T_g$) the viscosity is very high and the deformation is inhomogeneous via shear band formation, at temperatures higher than the glass transition temperature (but lower than the first crystallization temperature) deformation takes place by a homogeneous flow mechanism [49]. At $T \ll T_g$ metallic glasses exhibit very high strength values, a relatively low Young's modulus and a high elastic strain limit. Figure 2.7 shows fracture strength and E-modulus values for a series of bulk glassy alloys and comparatively, for some conventional alloys [50]. As it can be seen, Fe-based BMGs have a much higher strength than conventional crystalline Fe-based alloys, e.g. super high-strength steels. As well, it can be seen that BMGs have an elastic strain limit of around 0.02 which

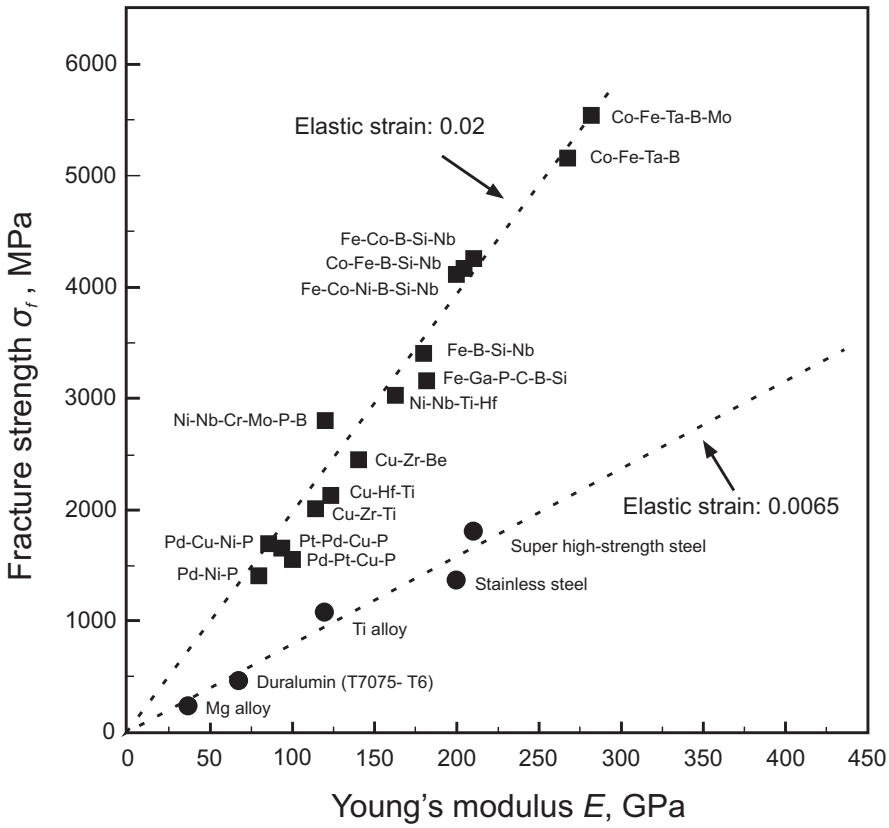

Figure 2.7: Relationship between tensile or compressive fracture strength and E-modulus for some bulk glassy alloys and comparatively for some conventional crystalline alloys [50].

is higher than the one corresponding to conventional crystalline alloys, i.e. 0.0065. However, a big disadvantage of metallic glasses in general is their lack of macroscopic plasticity at temperatures below the glass transition temperature which severely limits their application. There is however microscopic plastic deformation occurring in metallic glasses. The fracture surfaces of metallic glasses usually exhibit a vein-like morphology which is typical for 'ductile fracture', but this is on a much finer scale than in materials which fracture after significant macroscopic deformation. On the contrary, at $T > T_g$ (and $< T_x$), considerable macroscopic plastic deformation is observed and this aspect is benefited from in thermoplastic forming as mentioned in the previous paragraph. Contrary to the inhomogeneous mechanism at low temperature where strain is concentrated locally in shear bands, in the case of a homogeneous flow mechanism each volume element undergoes the same strain [49].

Soft magnetic properties Ferromagnetism is characterized by spontaneous magnetization, i.e. the spins of all magnetic electrons in a material are spontaneously aligned parallel due to exchange interaction between neighbouring magnetic atoms which are in close contact. As the short range order of amorphous alloys does not significantly differ from that of crystalline alloys (see section 2.1.3), it follows that parallel alignment of electronic spins on a long

range scale is possible although there is no long range order of atoms. Some amorphous alloys have remarkable soft magnetic properties such as very low coercivity and losses. In general, the magnetic behavior of soft magnetic materials is governed by domain wall pinning at heterogeneities such as grain boundaries, precipitates and inclusions [51]. This explains the very low coercivity of some amorphous alloys which principally lack all of the above heterogeneities. Values of coercivity, H_c, for several Fe-based BMGs are given in Table 2.2. Additionally, values of Curie temperature, T_C, and saturation polarization, J_s, are given.

2.1.5 Recent Fe-based bulk metallic glasses

Compared with most other bulk glassy alloy systems such as Zr- and Pd-based bulk metallic glasses, the Fe-based ones offer some important advantages: much lower material costs, higher strength, better corrosion resistance, and higher thermal stability (the glass transition temperatures, T_g, are close to or above 900 K) [1]. The first Fe-based BMG, i.e. $Fe_{73}Al_5Ga_2P_{11}C_5B_4$, was developed in 1995 by Inoue et al. [52]. But up to 2004, a major obstacle to the feasibility of Fe-based bulk glasses was their limited GFA, i.e. the maximum diameter achievable at that time by Cu-mold casting was 4 mm [53]. This was greatly overcome by the discovery, that minor additions of rare earth elements significantly improve their GFA [1, 7, 8]. This improvement has several reasons: Y adjusts the composition closer to an eutectic [7], Y scavenges the O (oxygen) impurity from the alloy via the formation of yttrium oxides [7], Y destabilizes the metastable $Fe_{23}C_6$ phase which usually forms firstly when Fe-based BMGs devitrify [8]. Furthermore, by adding small amounts of rare earth elements, commercial raw materials and low vacuum conditions (even air atmosphere) may be used to successfully fabricate some Fe-based bulk glassy alloys [7, 9–12]. These practical advantages contribute to further lowering the cost of these alloys [13]. Due to these positive aspects, their potential for engineering applications significantly increased. At present, one major inconvenient of Fe-based bulk glasses remains their relatively high brittleness. Efforts are made to improve their ductility [54]. Table 2.2 shows a list of selected Fe-based bulk glasses and some main thermal, mechanical and magnetic characteristics. As it can be seen in the table, the alloy investigated in this work has one of the largest critical diameter. Still, up to the present, only one alloy, i.e. $Fe_{41}Co_7Cr_{15}Mo_{14}C_{15}B_6Y_2$, has a larger critical diameter, i.e. 16 mm. In terms of thermal and mechanical characteristics, the $(Fe_{44.3}Cr_5Co_5Mo_{12.8}Mn_{11.2}C_{15.8}B_{5.9})_{98.5}Y_{1.5}$ alloy has medium values compared to other Fe-based bulk glasses except for the elastic modulus which is the highest among the selected compositions. Depending on their composition their Curie temperature takes values in a large interval, i.e. $55 - 732\,\mathrm{K}$, meaning that at room temperature Fe-based BMGs can be soft-magnetic or non-ferromagnetic. The $(Fe_{44.3}Cr_5Co_5Mo_{12.8}Mn_{11.2}C_{15.8}B_{5.9})_{98.5}Y_{1.5}$ bulk metallic glass, which was subject of this study, is non-ferromagnetic at room temperature.

The bulk glassy $(Fe_{44.3}Cr_5Co_5Mo_{12.8}Mn_{11.2}C_{15.8}B_{5.9})_{98.5}Y_{1.5}$ alloy In 2004, Lu et al. [1] reported firstly on the bulk glass forming $(Fe_{44.3}Cr_5Co_5Mo_{12.8}Mn_{11.2}C_{15.8}B_{5.9})_{98.5}Y_{1.5}$ alloy. This was the most prospective among the first Fe-based glassy alloys of the so-called *bulk amorphous steels family* (BAS). Table 2.2 shows comparatively values for some characteristics of this alloy and other Fe-based bulk glassy alloys. For this particular composition a maximum amorphous sample thickness of 12 mm was obtained by Cu mold casting expressing its extremely high GFA. Its thermal behaviour was investigated by differential scanning calorimetry (DSC) and showed that at a heating rate of 0.33 K/s the glass transition temperature T_g is as high as 804 K [1] which was confirmed subsequently by Siegel, i.e. 813 K [40] and by Gostin et al. [55], i.e. 814.8 K (both measured at 0.33 K/s as well). Further thermal parameters are given in Table 2.2. Figure 2.8 shows the DSC curve of the bulk glassy $(Fe_{44.3}Cr_5Co_5Mo_{12.8}Mn_{11.2}C_{15.8}B_{5.9})_{98.5}Y_{1.5}$ alloy [55]. As seen in Fig. 2.8 the bulk glassy $(Fe_{44.3}Cr_5Co_5Mo_{12.8}Mn_{11.2}C_{15.8}B_{5.9})_{98.5}Y_{1.5}$ alloy has a complex crystallization sequence indicating that it devitrifies in multiple crystalline phases. Siegel conducted a systematic study

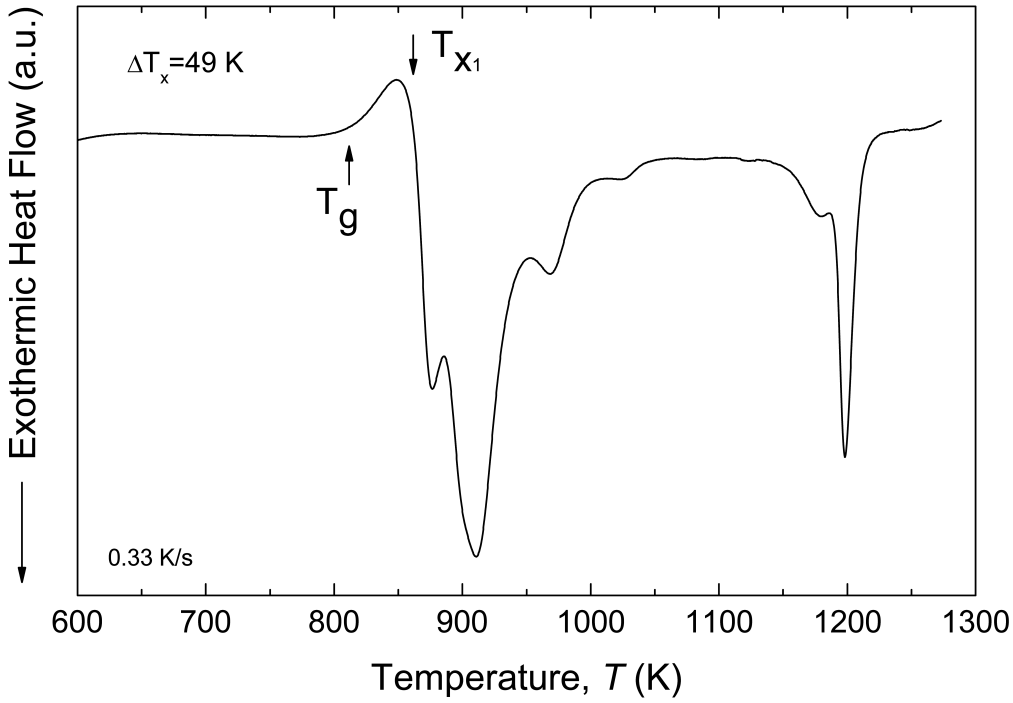

Figure 2.8: DSC curve of the bulk glassy $(Fe_{44.3}Cr_5Co_5Mo_{12.8}Mn_{11.2}C_{15.8}B_{5.9})_{98.5}Y_{1.5}$ alloy [55].

consisting of structural analysis by XRD and TEM of this bulk glassy alloy after various annealing treatments at temperatures above T_{x1} [40].

Table 2.2: Thermal, mechanical and magnetic properties of selected Fe-based bulk glasses.
(a) and (b) reported as 12 and 11.7 GPa, respectively. Transformed to HV considering a factor of 0.009807.

composition, at%	D_{max}, mm	T_g, K	ΔT_x, K	T_x, K	T_m, K	T_l, K	σ_y, GPa	σ_f, GPa	E, GPa	ϵ_{pl}, %	HV	T_C, K	J_s, T	H_c, A/m	Publ. Year	Ref.
$Fe_{73}Al_5Ga_2P_{11}C_5B_4$	1	732	53	785	-	-	-	-	-	-	-	606	1.26	82	1995	[52]
$Fe_{65.5}Cr_4Mo_4Ga_4P_{12}C_5B_{5.5}$	3	757	60	817	1251	-	2.82	2.8	161	0.15	-	-	0.78	62	2002	[56, 57]
$Fe_{30}Cr_{30}Mo_{15}C_{15}B_{10}$	1	940	69	1009	-	-	extraordinary corrosion resistance corrosion rate <10μm/year in 12M HCl								2002	[58]
$Fe_{41}Co_7Cr_{15}Mo_{14}C_{15}B_6Y_2$	16	838	50	888	1387	1437	-	3.5	-	-	1253	-	-	-	2005	[9]
$[(Fe_{0.5}Co_{0.5})_{0.75}B_{0.2}Si_{0.05}]_{96}Nb_4$	7.7	822	41	863	-	-	-	-	-	-	1223[a]	732	1.13	$\leq$20	2006	[59, 60]
$Fe_{66}Nb_4B_{30}$	2	845	31	876	-	1451	-	3.8	-	-	1193[b]	550	1	1.5	2006	[61, 62]
$Fe_{48}Cr_{15}Mo_{14}C_{15}B_6Er_2$	12	843	50	893	-	1443	-	4.2	213	0	-	-	-	-	2007	[54]
$(Fe_{0.432}Co_{0.288}B_{0.192}Si_{0.048}Nb_{0.04})_{96}Cr_4$	3	833	41	874		1416	3.9	4.01	200	0.70	1038	-	0.811	0.6	2008	[63]
$(Fe_{0.76}Si_{0.096}B_{0.096}P_{0.048})_{96}Cr_4$	3	773	54	827	1250	1370	-	-	-	-	-	-	1.29	2.4	2008	[64]
$Fe_{74}Mo_4P_{10}C_{7.5}B_{25}Si_2$	5	729	37	766	1211	1266	2.8	3.2	-	4.3	-	-	1.19	-	2009	[65]
$(Fe_{44.3}Cr_5Co_5Mo_{12.8}Mn_{12}C_{15.8}B_{5.9})_{98.5}Y_{1.5}$	12	804	-	-	1344	1411		3000	257	-	1224	55			2004	[1]
$(Fe_{44.3}Cr_5Co_5Mo_{12.8}Mn_{12}C_{15.8}B_{5.9})_{98.5}Y_{1.5}$	-	813	48	861	1349	1410	-	1200-1400	226	0	1218	-	-	-	2010	[40]
$(Fe_{44.3}Cr_5Co_5Mo_{12.8}Mn_{12}C_{15.8}B_{5.9})_{98.5}Y_{1.5}$	-	814.8	47.2	861	-	-	-	-	-	-	-	-	-	-	2009	[55]

When the annealing treatment is performed at a temperature above all crystallization events, e.g. 1273 K, so that the sample is completely devitrified, mainly three phases were detected: $M_{23}(B,C)_6$, $Mo_3(Co,Fe)_3C$ and $Mo_{12}(Co,Fe)_{22}C_{10}$. According to the original paper [1], at room temperature this alloy has a compressive strength of ∼3 GPa. Subsequent measurements performed on as many as 30 samples revealed that its compressive strength takes values in a wide interval, i.e. $1.2 - 4$ GPa [40]. Furthermore, this bulk glassy alloy is very hard (1224 HV). However, a big disadvantage of this alloy is that it is very brittle. Rod samples with cross-section >3 mm diameter produced by Cu-mold injection break apart when taken out of the mold due to strong internal stresses which may be caused by cooling rate gradients [40]. This effect is more pronounced at larger diameters of the rod. The rods with diameter of 3 mm as the one used in this work, did not have this problem. Although its extreme brittleness severely limits its applicability, due to its unusual composition and high GFA, this BMG is a very interesting target for fundamental studies of properties.

2.2 Corrosion of amorphous and crystalline alloys

The environmental stability of a material is a determining factor for its applicability. Without stability in the environment to which the material is exposed during service, no otherwise useful property can be exploited. Degradation of materials can be brought about by various processes such as dry oxidation, aqueous corrosion, a combination of these and mechanical stresses, etc. [66]. Among these, this thesis will address exclusively aqueous corrosion reactions at room temperature. The compositional and structural particularities of glassy alloys as compared to the crystalline ones, can determine significant differences in corrosion rates and mechanisms. These will be discussed fundamentally in this section. The main particularities that can affect corrosion processes of metastable alloys are: thermodynamic metastability, particular composition, e.g. metalloid content, and chemical homogeneity and defect structure. Firstly, a basic approach is done in terms of mixed potential theory. In this theory [67], any electrochemical corrosion reaction can be divided in partial oxidation and reduction reactions which occur delocalized at the electrode surface. Under free corrosion or open circuit conditions, meaning that no polarization is applied to the electrode, the rate of the oxidation reactions must be equal to the rate of the reduction reactions. In Fig. 2.9, this is shown for the simple case of an unnoble metal, M, immersed and actively dissolving in an acid electrolyte. In this example, there are two electrode reactions: one is eq. (2.2), the metal electrode reaction, and the other one is eq. (2.3), the hydrogen electrode reaction.

$$M \underset{\text{red.}}{\overset{\text{ox.}}{\rightleftharpoons}} M^{z+} + ze^{-} \qquad \text{eq. (2.2)}$$

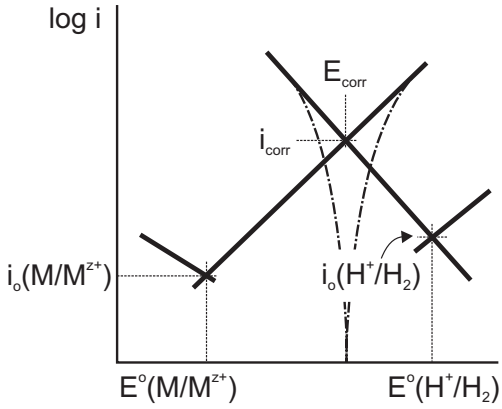

Figure 2.9: Schematic i-E curves for partial reactions of charge transfer type and resulting mixed corrosion reaction (dashed dot line) for an unnoble metal in an acid solution.

$$\mathrm{H_2} \underset{\text{red.}}{\overset{\text{ox.}}{\rightleftharpoons}} 2\,\mathrm{H^+} + 2\,\mathrm{e^-} \qquad \text{eq. (2.3)}$$

where z is the valence of the metal ion. Both reactions are characterized by equilibrium potentials $E^o_{M/M^{z+}}$ and $E^o_{H^+/H_2}$, and exchange current densities $i_o^{M/M^{z+}}$ and $i_o^{H^+/H_2}$. At equilibrium, each reaction will take place at equal rates in both directions, oxidation and reduction, and this rate is called exchange current density. When two reactions with different equilibrium potential take place on the same electrode, as is the case in corrosion, the potential of that electrode will self-regulate to a value between the equilibrium values of those reactions. This potential is called corrosion potential, E_{corr}. Since the potential is no longer equal to the equilibrium potential of either of the component reactions, either oxidation or reduction of each component reaction will be enhanced while the other one is retarded. In the above given example of an unnoble metal, M, immersed in an acid electrolyte, schematically illustrated in Fig. 2.9, the equilibrium potential of the metal reaction is less noble than the one of the hydrogen reaction, i.e. $E^o_{M/M^{z+}} < E^o_{H^+/H_2}$. Therefore, metal oxidation and hydrogen reduction will be favored. In accordance with the principle of charge conservation, no charge can be accumulated on the freely immersed electrode (free corrosion or open circuit condition). Therefore, the current density of metal oxidation has to be equal to that of hydrogen reduction. This value is the corrosion current density, i_{corr}.

2.2.1 The effect of metastability

The rate at which the metal oxidation reaction takes place as a function of polarization (the difference between the applied potential and the equilibrium potential) can be expressed according to the Tafel law [67]:

$$i_{anodic} = i_o \cdot \exp \frac{\beta \cdot z \cdot F \cdot \eta}{R \cdot T} \qquad \text{eq. (2.4)}$$

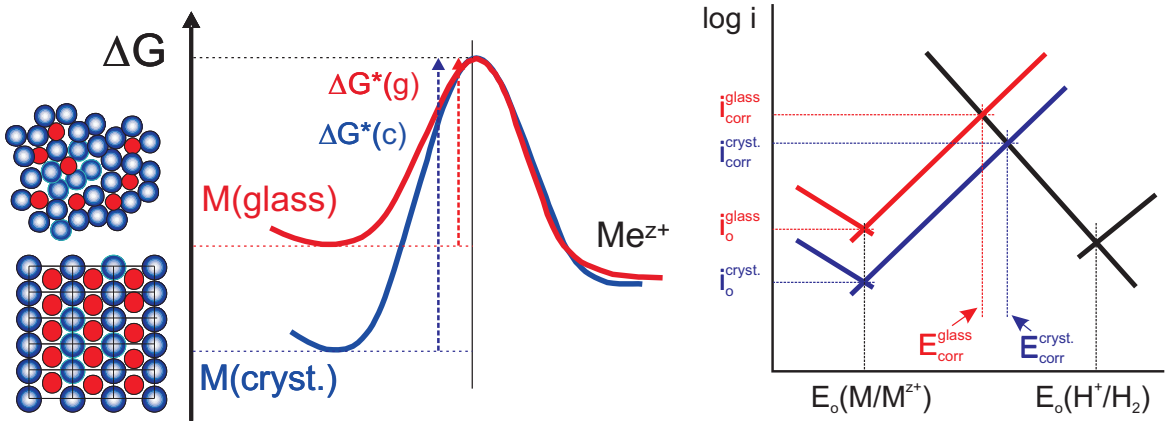

(a) (b)

Figure 2.10: a) Schematic representation of the free energy at the interface metal/electrolyte for crystalline and glassy alloys; b) schematic i-E curves for glassy and crystalline alloys when ΔG^* is the predominant factor.

where β is the symmetry factor, z is the valence of the metal ion, F is the Faraday constant, η represents the overpotential, R is the gas constant, and T represents the temperature. The exchange current density of the metal charge transfer reaction, i_o, is in turn expressed as [68]:

$$i_o = z \cdot F \cdot \frac{k \cdot T}{h} \cdot \frac{\alpha \cdot N_s}{N_A} \cdot \exp(-\frac{\Delta G^*}{R \cdot T}) \qquad \text{eq. (2.5)}$$

where $\frac{k \cdot T}{h}$ is a frequency factor (about $10^{12}\,\mathrm{sec}^{-1}$), k is the Boltzmann constant, h is the Plank constant, ΔG^* is the electrochemical free energy of activation, N_s the number of atoms per unit surface area (about $10^{15}\,\mathrm{sec}^{-2}$), N_A is Avogadro's number, and α is the fraction of the total number of surface atoms which are considered to be electrochemically active sites, i.e. sites which are likely to be candidates for removal by dissolution. In crystalline metals, α is a function of the crystallographic orientation (ledge and kink density, etc.), the density of dislocations emerging at the free surface, the grain size, etc. According to basic considerations of Latanision et al. [68], when comparing a glassy and a crystalline alloy with the same composition, the glass may be expected to have a smaller α value. Additionally, ΔG^* may be lower for a glassy metal surface than for a crystalline alloy. As shown schematically in Fig. 2.10(a), the atoms at a glassy metal surface are in non-equilibrium configuration and, therefore, sit on higher energy levels than corresponding atoms on a crystalline alloy surface. This ultimately translates to a lower free energy of activation, ΔG^*, for glassy alloys. Figure 2.10(b) shows the effect on the polarization curve, if ΔG^* is the dominant factor. According to eq. (2.5) a lower ΔG^* value determines a higher exchange current density, i_o, which in turn determines a higher corrosion current density, i_{corr}. This can be expected for many glassy alloys with AN unnoble main component, but it is hard to detect experimentally

because crystalline counterparts of glassy alloys comprise mostly multiple crystalline phases and therefore galvanic effects will be superimposed. Heusler and Huerta proved this for Ni_2B and Co_3B which they managed to produce in both the glassy and the single-crystalline states [69]. However, for few alloys, e.g. FeCrPC, the opposite was observed. This is arguably due to α playing the major role [68]. But no clear proof is given for the assumed smaller α of glassy alloys as compared to crystalline ones. It is also noted in Fig. 2.10(b) that the corrosion potential, E_{corr} is shifted to less noble values.

2.2.2 The effect of metalloids

Cathodic kinetics can also be different in the case of glassy alloys as compared to crystalline ones. Similarly to anodic reactions, assuming Tafel behaviour, the rate of cathodic reduction can be described by [67]:

$$i_{cathodic} = i_o \cdot \exp \frac{(1-\beta) \cdot z \cdot F \cdot \eta}{R \cdot T} \qquad \text{eq. (2.6)}$$

and [68]:

$$i_o = z \cdot F \cdot \frac{k \cdot T}{h} \cdot C_s \cdot V_s \cdot \exp(-\frac{\Delta G^*}{R \cdot T}) \qquad \text{eq. (2.7)}$$

where C_s is the concentration of the electroactive species in the double layer per unit volume and V_s is the volume of the double layer. No information regarding the influence of structure on the free energy of activation for reduction reactions was found in the literature. Perhaps more important for the cathodic kinetics is a high content of metalloids which is typical for metal-metalloid glasses rather than their metastable state. The exchange current density for the hydrogen reduction reaction is much lower on metalloid surfaces (typically $10^{-13}\,\mathrm{A \cdot cm^{-2}}$) than on noble (typically $10^{-3}\,\mathrm{A \cdot cm^{-2}}$) or transition metal surfaces ($10^{-6}\,\mathrm{A \cdot cm^{-2}}$) [68]. As shown in Fig. 2.11, the corrosion rate of a metalloid-containing glass is expected to be lower than that of a similar crystalline alloy without metalloids. In consequence, the corrosion potential is expected to be more active.

The increased reactivity of the glassy state may also be responsible for a better passivating ability [17]. In general, for passive film formation prior active dissolution is necessary for the accumulation of beneficial metallic ions and anions like OH^- at the alloy/electrolyte interface which precipitate as solid oxides or hydroxides when the solubility limit is reached. Indeed, starting with the revolutionary finding of Naka et al. in 1974 [70], it was repeatedly found that in order to passivate, glassy Fe-based alloys require lower concentrations of passivating elements than conventional crystalline alloys [17].

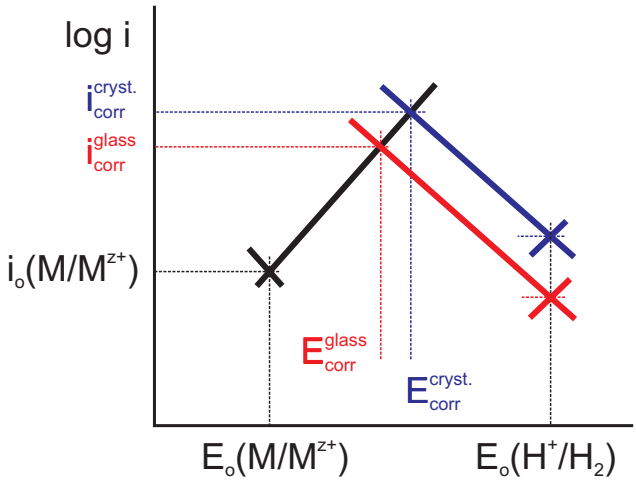

Figure 2.11: Schematic i-E curves for glassy and crystalline alloys showing the influence of metalloids.

As it is stated at the beginning of this section, when making an approach in terms of the mixed potential theory, the particular high concentration of metalloids of many metallic glasses can play a major role for cathodic kinetics. Additionally, the metalloids can have another important effect. The hydrogen evolution reaction occurs in two main steps [68]: firstly, atomic hydrogen (adatoms) is formed at the electrode surface by an electrochemical reduction reaction and, secondly, molecular hydrogen is formed by the combination of hydrogen adatoms. The metalloids inhibit the combination reaction and, therefore, an increased amount of adsorbed atomic hydrogen remains on the glassy alloy surface [68]. This in turn might dramatically enhance the probability of hydrogen being absorbed by the alloy. Not surprisingly, studies show that some metallic glasses are susceptible to severe hydrogen embrittlement [68]. Finally, metalloids affect the kinetics of passivation and the passive film composition. Various metalloids, e.g. P, C, B, Si, have different contributions to these aspects of passivity. Many studies have been performed in this direction, but since most of these focused on Fe-based alloys, details will be given in the next section dedicated entirely to the corrosion of Fe-based glasses.

2.2.3 The influence of chemical homogeneity

A well-known often used argument for an expected high corrosion resistance of metallic glassy alloys is their single-phase nature. Ideally, metallic glasses are regarded as being physically and chemically homogeneous, i.e. free from structural defects like grain boundaries or dislocations, secondary phases or inclusions. This idealized image of metallic glasses was argued to cause benefits such as the formation of laterally uniform passive films and the absence of active surface sites which could act as preferential spots for localized corrosion initiation [17]. As

well, the absence of secondary phases excludes the possibility of galvanic corrosion, a type of corrosion often observed for multiphase alloys [71]. However, in practice the presence of heterogeneities in cast samples cannot be completely avoided especially in commercial production. Examples comprise gas pockets formed by entrapment of gas bubbles during production [72] and small crystallites formed due to the presence of oxygen in the melt [73]. Several studies revealed that these heterogeneities or their interface with the glassy matrix act as pit initiation sites [27, 74–76]. In addition to the above mentioned heterogeneities, Vishwanadh et al. reported in a recent study [75] that there is a gradient of MRO in the cross-section of a rod sample of the bulk glassy $Zr_{52}Ti_6Al_{10}Cu_{18}Ni_{14}$ alloy and this also influences the corrosion behaviour. The gradient of MRO is due to the cross-sectional cooling rate gradient. The degree of MRO was determined by fluctuation microscopy. It was observed that the periphery of the cross-section of the rod has a lower degree of MRO than the centre. Microcell measurements in 0.25 M H_2SO_4 + 0.025 M NaCl and in 0.025 M HCl at three locations along the cross-section of the rod showed a decreasing anodic current density with increasing distance from the centre. It was stated that this can be an effect of the degree of MRO, i.e. the lower the degree of MRO, the lower the anodic current density.

Corrosion morphology Another interesting aspect regarding the corrosion of glassy alloys is their corrosion morphology. For classical crystalline metals and alloys, the morphology of corroded surfaces is strongly influenced by structural factors such as crystal orientation, grain boundaries, precipitates, etc. The surface morphology is determined by locally varying corrosion rates. Zones which are corroding at a higher rate will appear as valleys, while those corroding at a lower rate will appear as hills. Depending on their orientation, grains of polycrystalline alloys have different corrosion rates as well as grain boundaries and precipitates corresponding to their varying active dissolution tendency [20]. In addition, heterogeneities in crystalline materials are often recognized as preferential sites for the initiation of localized corrosion, especially pitting corrosion [21]. As mentioned earlier, contrary to crystalline alloys, amorphous alloys are principally missing those structural particularities and therefore, the questions arise: (i) how is an active corrosion process on the surface of such a homogeneous glassy alloy initiated and (ii) how does the morphology of such a corroding surface evolve? In order to analyze this, morphological studies using in-situ and ex-situ observation techniques with high resolution are required. Only few such studies have been reported for metallic glasses. For example, Green et al. [22] studied in-situ the initial stages of pitting on a glassy $Zr_{50}Cu_{40}Al_{10}$ surface by optical microscopy. In another study, Wang at al. [23] used atomic force microscopy (AFM) to characterize and compare the morphology evolution of amorphous and crystalline $Ni_{50}Nb_{50}$ surfaces in order to understand the breakdown of passive films. In the case of Fe-based glasses, morphology observations of corroded surfaces have been limited to ex-situ SEM

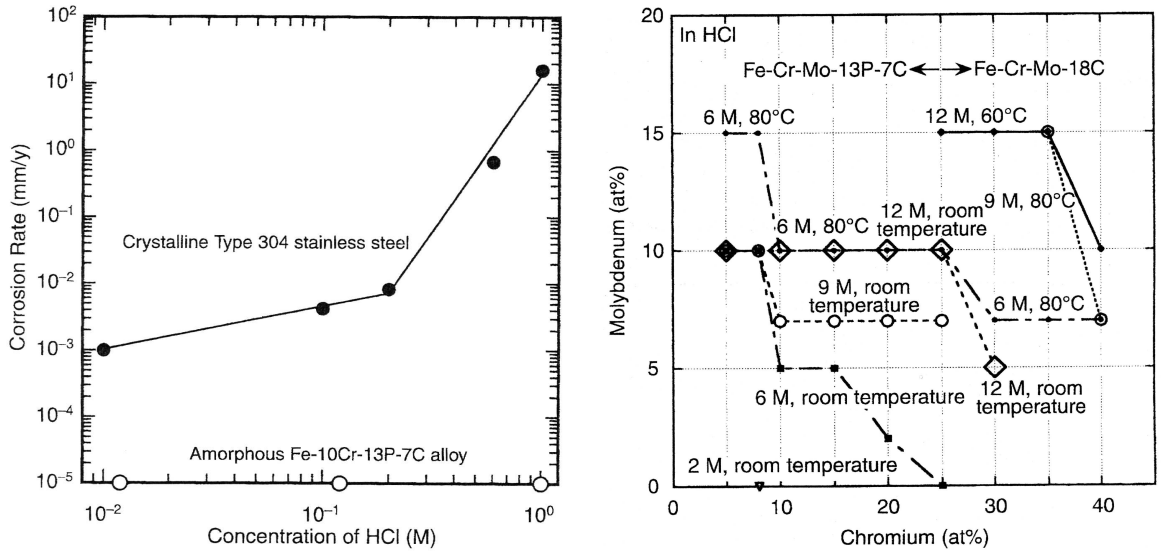

(a) (b)

Figure 2.12: (a) Corrosion rates of the amorphous Fe-10Cr-13P-7C alloy and the grade 304 stainless steel in HCl of various concentrations at room temperature [70], and (b) Critical concentrations of Cr and Mo necessary for spontaneous passivation of glassy Fe-Cr-Mo-metalloid alloys in HCl of various concentrations and temperatures [14].

investigations of alloys like $Fe_{70}Cr_{10}P_{13}C_7$ and $Fe_{50\text{-}x}Cr_{16}Mo_{16}C_{18}B_x$ (B = 4, 6 and 8), mainly subjected to pitting or crevice corrosion in chloride-containing solutions [24–30]. The present work addresses this important issue. Detailed investigations regarding the evolution of surface morphology during active dissolution have been conducted for the bulk glassy $(Fe_{44.3}Cr_5Co_5Mo_{12.8}Mn_{11.2}C_{15.8}B_{5.9})_{98.5}Y_{1.5}$ alloy studied in this work (see section 4.5.

2.3 Corrosion of Fe-based glasses

Among all known metallic glasses, the Fe-based systems have been investigated most intensively regarding their corrosion behaviour. The first fundamental study in the field of corrosion of metallic glasses was done on Fe-based glasses [70]. In this initial study, it was discovered that some amorphous alloys can achieve corrosion resistance superior to that of stainless steels. As it can be seen in Fig. 2.12(a) the glassy Fe-10Cr-13P-7C alloy did not corrode in 10^{-2}–10^{0} M HCl solutions while the conventional stainless steel grade 304 exhibited significant corrosion rates. Moreover, a similar glassy alloy with only 8 at.% of the passivating element Cr passivates spontaneously in 2 M HCl and does not suffer from pitting corrosion by anodic polarization [70]. Due to this initial encouraging finding, much effort was dedicated to further improving the passivation ability of those glassy alloys through composition opti-

mization. As a result, exceptional corrosion resistance was demonstrated for some alloys, e.g. Fe-Ni-Cr-Mo-B alloys which exhibit excellent passivating behaviour in acid solutions up to 250°C [15], or Fe-Cr-Mo-metalloid alloys (metalloids = P, C) with certain compositions which passivate spontaneously even in hot concentrated HCl [14]. As it can be seen in Fig. 2.12(b), given sufficient additions of Cr(25 at.%) and Mo (15 at.%), some glassy Fe-Cr-Mo-metalloid alloys passivate spontaneously even in 12 M HCl at 60°C. This is remarkable as no commercial crystalline metal except Ta can passivate spontaneously in HCl more concentrated than 1 M (at room temperature) [17]. But this first generation of glassy Fe-based alloys possesses low glass forming ability and thus, can be obtained only as thin or small products (thickness $\ll 1\,\mathrm{mm}$), e.g. ribbons, foils, flakes, powders or films. In order to overcome the size limitation of this first generation, a second generation of alloys that are bulk glass-formers with thickness $> 1\,\mathrm{mm}$ was recently developed. However, they were predominantly designed for other properties, e.g. for combining high GFA and excellent mechanical performance, rather than for corrosion resistance. Therefore, these alloys have substantially different compositions compared to the earlier ones, e.g. many of them contain Mn and have lower concentrations of Cr and P [16]. Although those compositional variations can have quite a critical influence, their corrosion behaviour was scarcely studied so far. Therefore, the present work focuses on one of the alloys of the newest generation as an example case and provides a starting point in understanding the complex behaviour of these multicomponent high-performance Fe-based bulk glassy alloys.

In the following, a summary of the previous research done in the field of corrosion of mainly non-bulk Fe-based glasses is given. In general, studies in this area comprise structural characterization of alloy samples, determination of corrosion and electrochemical parameters by weight-loss and polarization measurements, surface analytical studies to determine passive film compositions and some observations of local corrosion damage morphology.

In general, compared to pure Fe, simple Fe-metalloid glasses without a second metallic element, e.g. $Fe_{80}B_{20}$, $Fe_{75}B_{25\text{-}x}Si_x$, $Fe_{80}P_{13}C_7$, have lower corrosion resistance and also tend to show poorer ability to passivate during anodic polarization [17, 19, 77]. However, addition of many metallic elements, except Mn, improves their corrosion resistance. Figure 2.13 shows the effect of selected alloying element types and concentrations on the corrosion rate of the $Fe_{80}P_{13}C_7$ glass in 0.1 N HCl and 0.1 N H_2SO_4 solutions [24]. Hashimoto [17] stated that, depending on the role they play in increasing the corrosion resistance, they can be classified in three groups. The first group comprises Cr and Ti which form their own passive film and contribute to increased corrosion resistance by supporting a stable passive film. The second group includes elements which are more active than Fe, e.g. V, Mo, W. Their passive region is less pronounced than that of Fe and their passive films are less stable than those of Fe or Cr. Accordingly, passive films on Fe-based glasses contain a very low amount of oxidized species of those elements. They are however beneficial for passivation. In the active potential region of

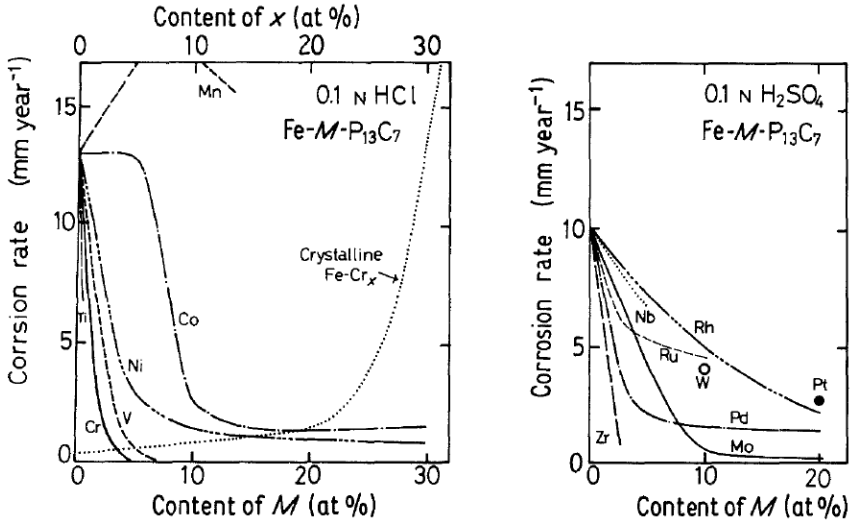

Figure 2.13: Influence of metallic element type and concentration on the corrosion rate of glassy $Fe_{80}P_{13}C_7$ in 0.1 N HCl and 0.1 N H_2SO_4 at 30°C [24].

these alloys, those elements decrease the active dissolution rate because they form corrosion product films which act as a diffusion barrier against dissolution. Moreover, they assist the accumulation of passivating species e.g. Fe, Cr, below the above mentioned corrosion product films, which results in improved passivation ability. However, as will be demonstrated later for the case of Mo, excess addition of those elements is sometimes detrimental. The third group includes metallic elements which are more noble than the main element Fe. These are Ni, Co, Cu, Ru, Rh, Pd, Pt, etc. In principle, upon immersion into a corrosive media, selective enrichment of the noble metals occurs on the surface which in turn decreases the overall anodic activity and dissolution rate of the glassy alloy. Also the cathodic activity increases. Consequently, both the free corrosion resistance and the passivation ability are increased by alloying with those elements.

The role of Cr A frequently used alloying element in Fe-based glasses, especially in those designed for corrosion resistance, is Cr. This element was found to be the most effective in improving the corrosion resistance by causing spontaneous passivation [17]. In general, compared to stainless steels which require at minimum 13 at.% Cr, glassy alloys require a smaller Cr content for achieving stable passivity. This was principally explained by the chemical homogeneity of the underlying alloy. In order to better understand the nature of these more stable passive films, numerous surface analytical investigations have been performed. The passive film on Cr-rich Fe-based glassy alloys, i.e. with $\geq$ 10 at.% Cr, was found to consist mainly of hydrated Cr oxyhydroxide, i.e. $CrO_x(OH)_{3-2x} \cdot nH_2O$, where n and x depend on the alloy composition and the conditions of formation. It is known that the film formed in air on Fe-Cr alloys, crystalline or glassy, is composed of an outer Fe-rich layer and an inner Cr-rich

layer. Anodic passivation leads to dissolution of Fe from the outer layer leaving the passive film enriched in Cr. The stability of a passive film is often related to its ratio of Cr and Fe species concentrations which depends on the concentration of Cr in the underlying alloy. For conventional stainless steels a significant enrichment of Cr species in the passive film occurs for concentrations of Cr in the alloy above 13 at.%. Remarkably, glassy Fe-Cr based alloys were observed to have a much higher ability to accumulate Cr species in their passive films, e.g. 97 % Cr^{3+} of cations in the passive film of the $Fe_{70}Cr_{10}P_{13}C_7$ alloy formed in 1 N HCl [14]. Addition of other metallic elements to Fe-Cr-metalloid glassy alloys can further improve the corrosion behaviour in some respects. Mo is often used to improve passivity and pitting resistance [78, 79]. Adding Mo does not change the concentration of Cr-oxyhydroxide in the passive film. However, it does assist passivation by favouring the accumulation of Cr species at the surface. In fact, as shown by Habazaki et al. [80], higher concentrations of Mo determine higher passivation rates and lower quantities of dissolved Cr during passivation. When a sufficient quantitity of Mo is added, i.e. 7 at.%, almost no Cr is dissolved when the alloy is potentiostatically polarized in the passive region. The passive film is formed directly from the air-formed film as a result of selective dissolution of a small quantity of Fe. However, an excess addition of this otherwise beneficial element can be detrimental [81, 82]. As it can be seen in Fig. 2.14, passive current density values of bulk glassy $Fe_{75\text{-}x\text{-}y}Cr_xMo_yC_{15}B_{10}$ alloys in 1 N HCl depend dramatically on the concentration of Cr and Mo. As well, it can be seen

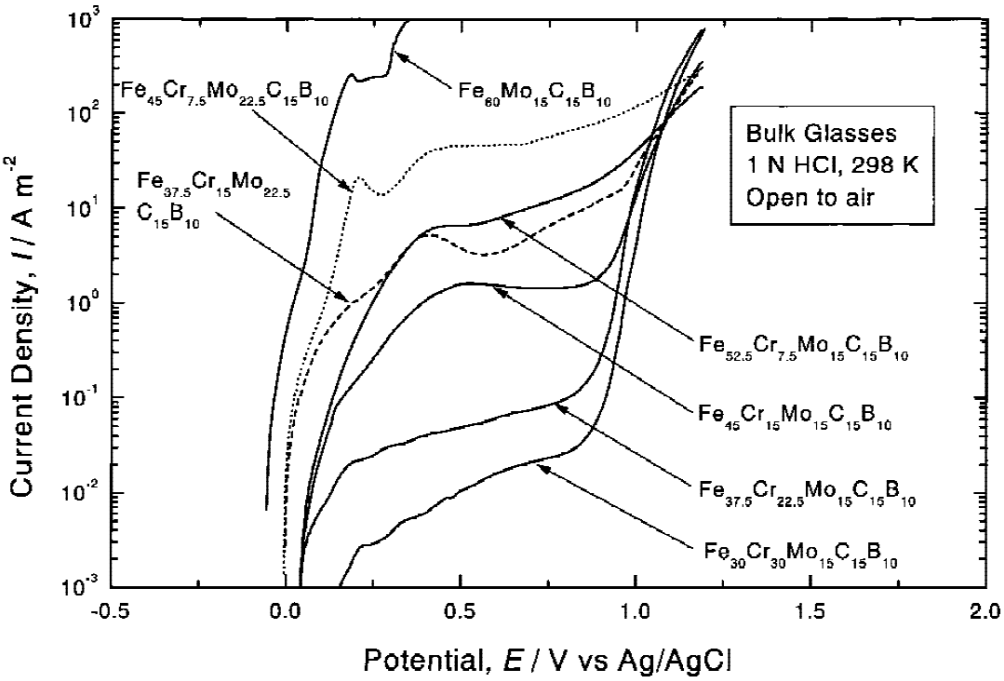

Figure 2.14: Anodic polarization curves of bulk glassy $Fe_{75-x-y}Cr_xMo_yC_{15}B_{10}$ alloys in 1 N HCl solution open to air at 298 K [82].

that, for constant Cr concentrations, higher Mo concentrations leads to higher passive cur-

rent densities meaning poorer protective ability of films. W has a similar beneficial influence at low concentrations [83]. There are however no data available for higher concentrations to confirm the detrimental effect at excess additions as it is the case for Mo.

The role of other metallic elements Additions of other metallic elements are especially beneficial in improving corrosion resistance when a small amount of *Cr* is present in Fe-P-C type glasses. This indicates that there is a synergistic effect between Cr and other metallic elements. It was shown that when replacing a few percents of Fe with Ti, Mn, Nb, V, W or Mo in the $Fe_{77}Cr_3P_{13}C_7$ glass the corrosion rate can become several times lower. Very interesting in this respect is that additions of 2 at.% of Mo, W, Ti or V to the above mentioned glass enable the measurement of a complete anodic polarization curve in 1 N HCl, i.e. up to and beyond the onset of the oxygen evolution reaction (otherwise, the glass with no extra alloying element is unstable in 1 N HCl). In order to have this ability, ferritic stainless steels require at least 30 at.% Cr, i.e. 10 times more than the glass [24].

Some attention was paid to the role of *Co* on corrosion reactions of Fe glasses, since Fe-Co-based glasses exhibit good soft magnetic properties [30, 50]. As shown in Fig. 2.13, an addition of Co to the glassy $Fe_{80}P_{13}C_7$ alloy is not as effective as an addition of Cr or other metallic elements such as V, Ni or Mo. On the contrary, Angelini et al. [30] found that Co increases the corrosion resistance of $Fe_{80-x}Co_xB_{10}Si_{10}$ glasses presumably due to the formation of protective films containing Co oxides. The increase is more pronounced when the pH value of the aggressive medium is lower. Another interesting finding of the same study is that increasing concentrations of Co determine an increase in the amount of B released into the solution.

It is obvious from Fig. 2.13 that *Mn* is the only element which actually deteriorates the corrosion resistance of the $Fe_{80}P_{13}C_7$ glass. Therefore, not much further effort was devoted to the investigation of the role Mn plays in corrosion reactions of those early glassy alloys. Surprisingly, a recent report dedicated to the study of the influence of Mn on magnetism and corrosion behaviour of the bulk glassy $(Fe_{44}Cr_{10}Mo_{12.5}Mn_{11}C_{15}B_6Y1.5)_{100-x}Mn_x$ (x=0, 2, 4, 8) alloy showed that increasing the Mn content improves the corrosion resistance in 1 M HCl, e.g. it increases the corrosion potential and lowers the corrosion current density [84].

Recently, it was discovered, as explained already in section 2.1.5 that the GFA of Fe-based glasses can be greatly improved by small additions of *rare earth elements*. Consequently, most of the recently developed Fe-based glassy alloys contain a few percents of those elements. Their effect on the corrosion behaviour of Fe-based BMGs was so far only scarcely studied. Recently, it was demonstrated that the stability of passive films grown on bulk glassy $Fe_{50-x}Cr_{15}Mo_{14}C_{15}B_6Y_x$ ($x = 0$, 0.5, 1, 1.5, 2) alloys is moderately influenced by the Y concentration. Addition of 2 at.% Y increases the open circuit potential by 100 mV and decreases

the passive current density more than 3 times [85, 86]. Y was found by X-ray photoelectron spectroscopy (XPS) to be present in the passive film of those alloys. It was also found by Mott-Schottky measurements that the semiconducting properties of the passive films vary with the Y content of the alloy. The effect of Y was therefore explained on the basis of doping theory. It was also suggested that Y can indirectly influence corrosion. Due to its high affinity for O it is often found to be segregated as Y oxide rich particles in the bulk glassy $Fe_{48}Cr_{15}Mo_{14}C_{15}B_6Y_2$ alloy [26]. These particles in turn act as initiation points for pitting. However, the dissolution of the alloy matrix was limited to the particle-near regions and did not propagate further as it is the case for typical pitting corrosion.

The role of metalloids In addition to the metallic constituents, most Fe-based glasses of the metal-metalloid type contain also a considerable amount (usually 15-25 at.%) of metalloids, e.g. B, C, Si and P. These elements are necessary for forming/stabilizing the glassy structure. But, besides this, they are of course expected to play an important role for corrosion since they have chemical properties which are principally different from those of metals. Compared to most conventional crystalline Fe-based alloys (steels), the concentration of metalloids in Fe-based glasses is much higher. As well, conventional steels are usually multiphase while the glasses are single phase materials. Therefore, the role of metalloids in corrosion reactions at such high metalloid concentrations was virtually unknown before the development of the first cast metallic glasses. In consequence, many reports on the topic were published especially in the 70-80's [87–90]. These focused mainly on the role of metalloids on the free corrosion rate, kinetics of passivation, composition of passive films and pitting corrosion. In the following, each common metalloid is discussed in detail.

One of the first studies compared the influence of B, C, Si and P on the corrosion rate of glassy $Fe_{70}Cr_{10}B_{13}X_7$ and $Fe_{70}Cr_{10}P_{13}X_7$ alloys [88]. As it can be seen in Fig. 2.15, the corrosion rate of the glassy Fe-Cr alloys progressively decreases by the addition of Si, B, C and P in 0.1 N H_2SO_4. Therefore, among the mentioned metalloids, P is the most effective for improving the corrosion resistance of Fe-based glasses containing Cr. It was revealed that this happens by promoting passivity [17, 89]. According to Naka et al. [88], P enhances the passivation ability by accelerating the dissolution rate in the active range and, therefore, promotes the enrichment of passivating species in the passive film. Later, Virtanen et al. and Elsener et al. [89, 90] discovered that P facilitates the active-passive transition by forming a porous $FePO_4$ pre-passive film on the alloy surface in the active domain. This pre-passive film blocks the active sites of the surface and accelerates the hydrogen evolution reaction. The formation of the actual passive Cr oxide layer takes place in the pores of the pre-passive layer. Phosphates are also incorporated in small concentrations in the passive film improving its stability against both dissolution and penetration of aggressive chlorides. It was also argued that the beneficial effect of P can be attributed to the enrichment of P underneath the passive film. This leads

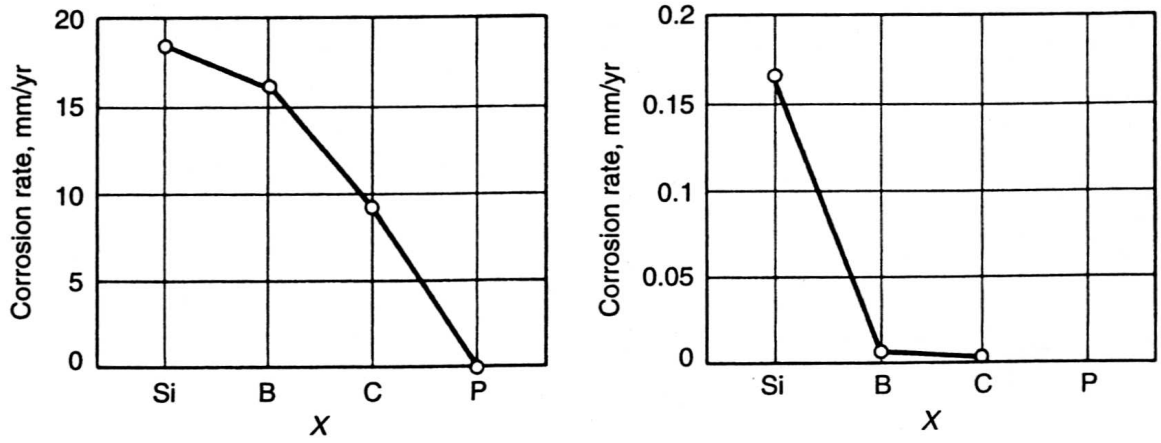

(a) (b)

Figure 2.15: Average corrosion rates estimated from the weight loss of amorphous (a) $Fe_{70}Cr_{10}B_{13}X_7$ and (b) $Fe_{70}Cr_{10}P_{13}X_7$ alloys in 0.1 N H_2SO_4 at 30 °C [88].

to a reduction of the ionic conductivity of the interface film/alloy, therefore enhancing the stability of the passive film. This sub-film enrichment in P was observed for example by Chattoraj et al. [91], and Elsener and Rossi [92].

According to Hashimoto [17], C does not greatly accelerate the formation of passive films on glassy alloys. However, it is not incorporated in the surface film since metal carbonates are generally soluble in aqueous solutions. Accordingly, C is considered to be the second most effective metalloid element in improving the corrosion resistance of glassy alloys if they contain a sufficient amount of passivating element. The ability of Si and B to accelerate the formation of a passive film is not high. These elements are usually present in the passive film as silicates and borates [17, 90]. Consequently, the passive film will have a lower concentration of Cr ions resulting in a lower protective ability. In the potential region of the active/passive transition the oxidized metalloids (SiO_4^{2-}, BO_2^-) together with cations form a more or less adherent, gel-like film with a high ionic conductivity which blocks the dissolution as a membrane inhibitor [90]. However, two studies were found to contradict the above stated general opinion. In the case of Si, it was observed that when replacing B in Fe-B and Fe-Ni-B, it actually enhances the stability of the passive film [77, 93, 94]. More recently, Pang et al. [25], performed a study on a series of $Fe_{50-x}Cr_{16}Mo_{16}C_{18}B_x$ glassy alloys and observed that, although oxidized B is present in the surface layer, it actually improves the passivation of these alloys by promoting Cr enrichment in the passive layer.

Pitting corrosion One of the most impressive characteristics of some metallic glasses is their very high resistance to localized corrosion. Particularly those Fe-Cr glasses which are resistant to general corrosion and especially those which contain both Cr and P exhibit excellent resistance to pitting corrosion. Furthermore, Mo improves the pitting resistance of both glassy

alloys and crystalline steels. Addition of 4 at.% Mo to glassy Fe-$Mo_xP_{13}C_7$ prevents pitting in 1 N HCl. It was argued that due to the enhanced reactivity of the amorphous state, rapid reformation of the passive film at regions, where it is damaged, takes place [95].
An important aspect regarding pitting corrosion is noted here with respect to the maximum attainable dimensions of glassy samples. In the case of the early Fe-based metallic glasses which were attainable only as samples with limited thickness ($\ll 1\,\mathrm{mm}$), e.g. ribbons, foils, films, investigations of pitting processes were affected by the fact that the pit growth in depth is prematurely stopped when the pit tip reaches the opposite surface. In the case of the more recent Fe-based *bulk* metallic glasses, pitting investigations can be confidently conducted because these alloys can be formed in samples with much larger thickness and, therefore, pitting processes are not affected by size limitations.
Finally, most of the fundamental corrosion studies on Fe-based glasses have been done on the earlier type. As explained above, the more recent type, the *bulky* Fe-based glasses, are different from their earlier versions in some respects, e.g. composition or thickness (affecting pitting). Therefore, corrosion processes of these newer alloys are expected to be different from those of their earlier versions. In consequence, new fundamental studies are required to understand the corrosion processes of Fe-based *bulk* glasses.

2.4 Corrosion of the constituent elements

A first approximate prediction of the corrosion behaviour of an alloy can be made starting from fundamental considerations on the corrosion behaviour of its individual constituent elements. A classical tool frequently employed in the study of corrosion in aqueous media are the potential-pH diagrams (Pourbaix diagrams) [96]. These diagrams are constructed on a thermodynamic basis for a given element and allow the prediction of the equilibrium states of all the possible reactions between this element, its ions and its solid and gaseous compounds in the presence of water. When the advantages and limitations of such diagrams are understood, valuable information can be made regarding corrosion reactions. Since these diagrams are based purely on thermodynamic considerations, additional information regarding the kinetics is necessary for a more realistic picture.

Fe As it can be seen in Fig. 2.16, the stability domain of Fe has no portion in common with that of H_2O and it is therefore a base metal. Its equilibrium potential is below that of hydrogen at all pH values and, consequently, it is unstable in the presence of H_2O and many aqueous non-oxidizing solutions. Upon immersion, Fe will corrode releasing Fe_2^+ with the evolution of hydrogen as a cathodic reaction. The dissolution reaction of Fe and other relevant reactions of this element and of other constituent elements are given in Table 2.3 (at

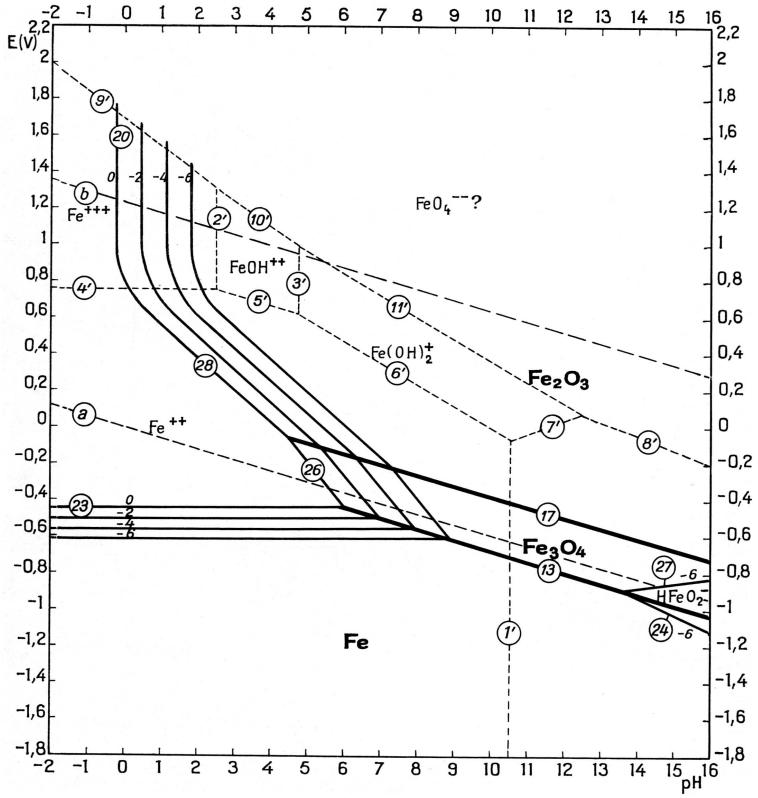

Figure 2.16: Potential-pH equilibrium diagram for the system Fe-H_2O, at 25°C (considering as solid substances only Fe, Fe_3O_4 and Fe_2O_3) [96].

the end of this chapter). This reaction is very vigorous in acid solutions, but its rate will decrease as the pH value of the solution increases. It will almost cease at pH values of 10-13 and Fe will become covered with a film of Fe oxides. At very high pH values, above 13, Fe will corrode in solutions free from oxidizing agents. As the equilibrium diagram in Fig. 2.16 shows, in the presence of oxidizing agents or upon application of an external anodic potential, Fe can passivate in acid solutions and in solutions with pH values higher than 13 if its potential is brought to values which are positive enough [96].

In acid solutions, e.g. 0.5 M H_2SO_4, the anodic polarization curve of Fe appears as the typical curve for an electrode with active-passive transition [71], as will be also shown later in this thesis (see section 3.3 and Fig. 3.1): starting with the corrosion potential, E_{corr}, there is an active dissolution range in which the current density, i, increases until it reaches the diffusion limit followed by a rapid decrease corresponding to passivation and then an increase corresponding to the oxygen evolution reaction and to transpassivation. With increasing pH value, both the passive and critical current densities, i_{pass} and i_{crit}, are decreasing gradually until, at pH 11.5, the active domain disappears completely and iron passivates spontaneously. However, the mechanism of passivation as well as the structure and composition of passive films on Fe depend on whether the solution is acid, neutral or alkaline [71]. While in

acid solutions Fe passivates in spite of the thermodynamic instability of its oxides by the incidental kinetic effect of slow dissolution of γ-Fe_2O_3 [97], Fe oxides are scarcely soluble in neutral and alkaline solutions. In acid solutions, the passive film is $3-5\,\mathrm{nm}$ in thickness and its composition is at best described as being disordered magnetite, $Fe_{3-\Delta}O_4$, with an Fe deficit, Δ, varying from $\Delta = 0$ at the Fe/oxide interface, where the oxide is magnetite, to $\Delta = 0.33$ at the oxide/solution interface, where it is maghemite, γ-Fe_2O_3 [98]. This oxide film is formed from a precursor salt layer, e.g. ferrous sulphate $FeSO_4$ layer. The mechanism of its formation is similar to the mechanism of direct growth of high-temperature oxide films. In weakly acid, neutral and alkaline solutions, the passive oxide film is formed stepwise: $Fe \longrightarrow FeOH \longrightarrow Fe(OH)_2 \longrightarrow \gamma$-$Fe_2O_3$ [71]. The alternative to this mechanism is rusting, producing, instead of protective barrier oxide films, non-protective porous layers of rust (simplified formula: FeOOH). Which of the two possibilities will occur depends on the solution composition, especially on the nature of the anions. In weakly acid solutions, the film has the same composition as the one formed in acid, but it is thickened by an outer porous hydroxide layer. In neutral and alkaline solutions a single inner Fe_3O_4 film with an additional outer hydroxide layer ($Fe(OH)_3$) is assumed [99].

Cr From Fig. 2.17, it is obvious that Cr is a very base metal since its domain of stability lies at much more negative potentials than that of H_2O. In acid solutions, it tends to decompose water with the evolution of hydrogen, releasing chromous ions, Cr^{2+}. In neutral and alkaline solutions, it tends to cover itself with chromic oxide, Cr_2O_3, or hydroxide, $Cr(OH)_3 \cdot n\,H_2O$ (when this is considered instead of the oxide). In the presence of very alkaline non-oxidizing solutions, it tends to dissolve as chromite ions CrO_2^- and CrO_3^{3-}. In solutions containing chloride ions, Cr is more easily attacked by both acid and alkaline solutions because the hydroxide $Cr(OH)_3 \cdot n\,H_2O$ has a higher solubility in such solutions (diagram not shown here). An essential point is that Cr establishes two clearly different states: an active state in which it is an extremely corrodible metal and a passive state in which it behaves similarly to a noble metal. This ability to strongly and stably passivate is what makes Cr so attractive as alloying element, e.g. for stainless steels. In this case $\sim$ 13 at.% Cr are at least required to attain complete coverage of surface with Cr oxide films. A change from one state to the other can be realized by modifying the oxidizing power of the contact solution or by anodic polarization. The oxidizing action of air is sufficient to bring Cr in the passive state [96].
Similar to Fe, in acid solutions Cr exhibits the typical anodic polarization curve of a passivable metal with a distinctly marked active-passive transition and a passive plateau with very low passive current density followed by a steep transpassive increase in current density due to metal dissolution and/or O_2 evolution. With increasing pH value, the active-passive transition shifts to less noble potentials. The thickness of the passive film in acid solutions

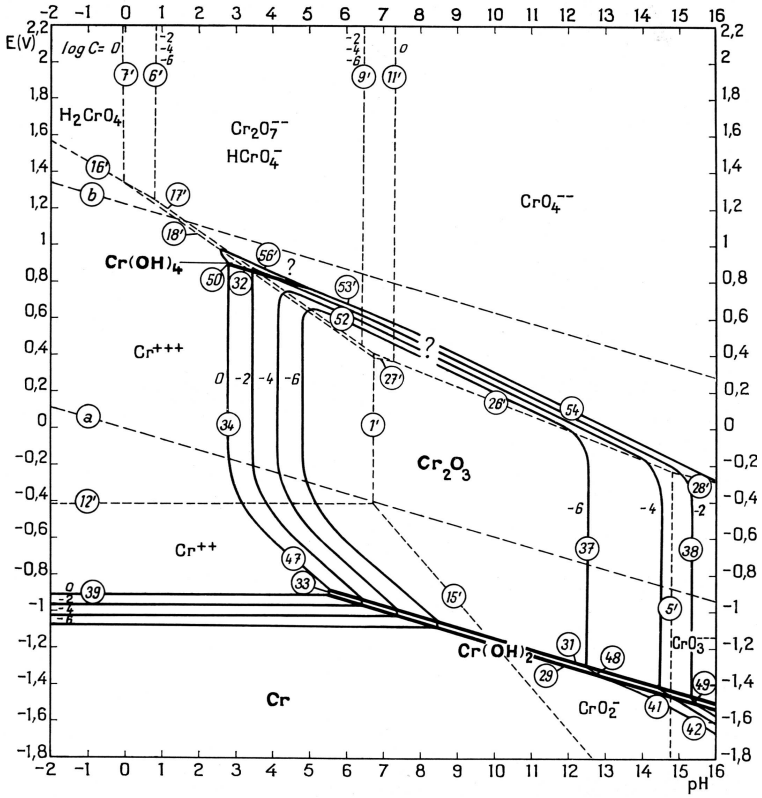

Figure 2.17: Potential-pH equilibrium diagram for the system Cr-H_2O, at 25°C (figure established considering anhydrous Cr_2O_3) [96].

is estimated to be $1-2\,\text{nm}$. The passive film is supposed to be the oxide Cr_2O_3 or the hydrated hydroxide $Cr(OH)_3 \cdot 0.3H_2O$. Since passivation was observed to be complete at potentials considerably more noble than the Cr/Cr_2O_3 equilibrium potential, it was concluded that passivation may be achieved by the oxidation of an oxidic precursor of lower valence. On pure Cr, anodic oxygen evolution cannot be observed, because of an early onset of transpassive rapid dissolution of the oxide Cr_2O_3 to hexavalent chromate ions, e.g. at pH 8, $Cr \longrightarrow Cr(OH)_2 \longrightarrow Cr_2O_3 \longrightarrow CrO_4^{2-}$.

Co The domain of thermodynamic stability of Co, as seen in Fig. 2.18, has an area in common with that of H_2O. Therefore, Co is considered to be a slightly noble metal, appreciably more noble than Fe. According to the diagram, the corrosion resistance of Co depends on the pH and the presence of oxidizing agents. Co is stable in neutral and alkaline solutions free from oxidizing agents, slightly corrodible in acid solutions free from oxidizing agents and very corrodible in acid or very alkaline solutions containing oxidizing agents. Neutral and slightly alkaline oxidizing solutions will cover Co with a film of oxide or hydroxide, e.g. $Co(OH)_2$, Co_3O_4. In practice, due to its large hydrogen overpotential, it is practically uncorroded by non-oxidizing acids [96]. Systematic investigations regarding the polarization behaviour and

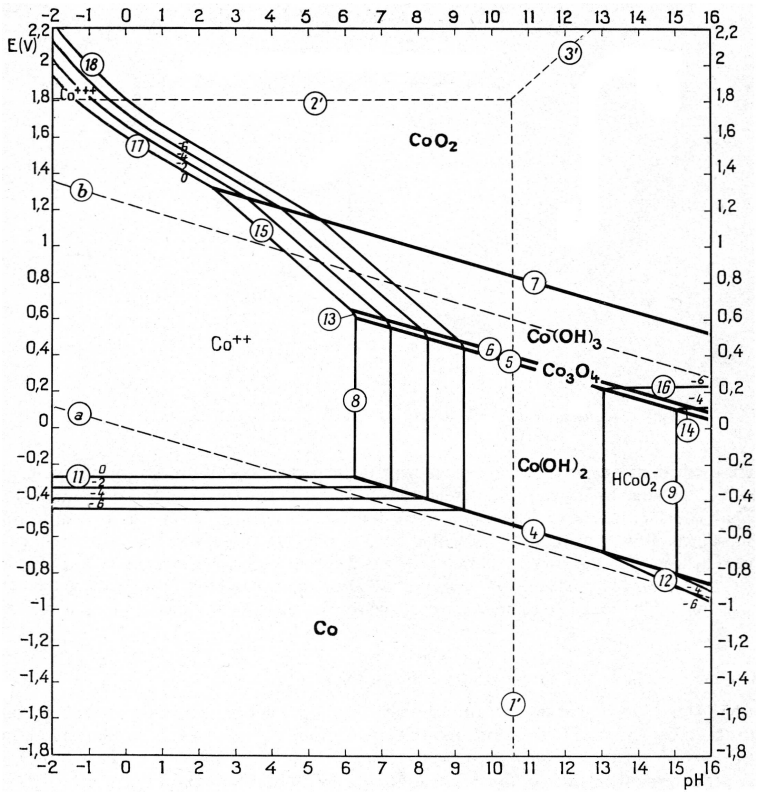

Figure 2.18: Potential-pH equilibrium diagram for the system Co-H_2O, at 25°C [96].

the composition of passive films on Co were conducted by Badawy et al. [100]. The native passive film on Co consists mainly of CoO or $CoO \cdot H_2O$. The passive film is unstable in acidic solutions. In neutral solutions the CoO is more stable. In basic solutions, anodic oxidation of Co results in the formation of $Co(OH)_2$, which is then further oxidized to Co_3O_4 and CoOOH at more noble potentials.

Mo As it can be seen in Fig. 2.19, Mo is a base metal as its domain of stability lies below that of H_2O at any pH value. In alkaline solutions, it has a weak tendency to decompose H_2O, dissolving in the hexavalent state as molybdate ions MoO_4^{2-}. In acid solutions, it tends to dissolve as Mo^{3+} ions under the evolution of hydrogen. In the presence of neutral and slightly acid or alkaline solutions, it tends to cover itself with tetravalent dioxide MoO_2 [96]. Mo is a vital alloying element in stainless steels used for applications in very aggressive corrosive environments. This is mainly due to its notorious ability to diminish the susceptibility to pitting and crevice corrosion. However, the mechanism through which this element promotes localized corrosion resistance is still not fully understood. Several mechanisms were proposed to explain the observed localized corrosion behavior of Mo containing stainless steels [79, 101, 102]. The formation of Mo salts in the oxide film has been suggested to improve the localized corrosion resistance of Mo containing stainless steels by lowering the solubility of the layer.

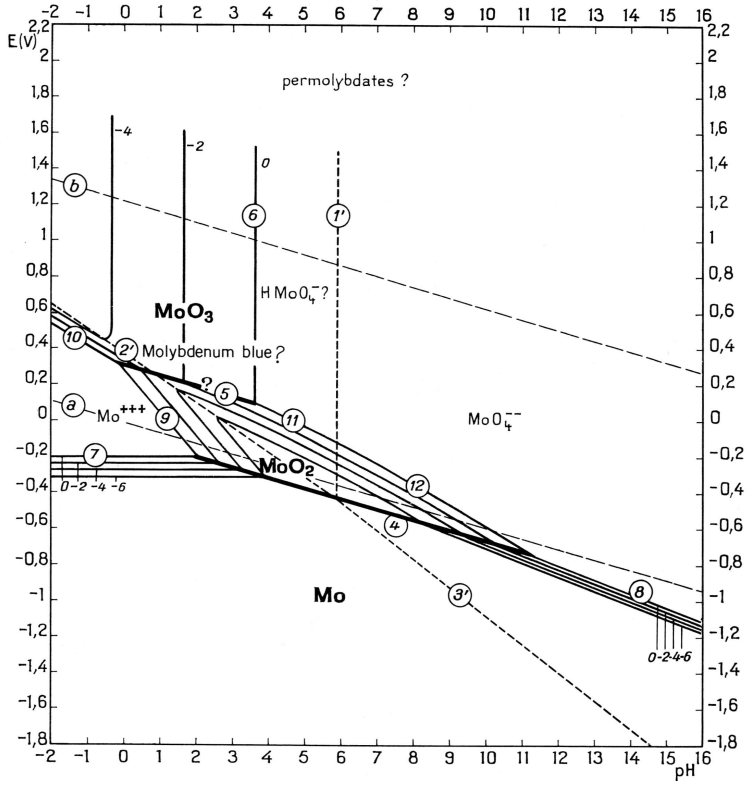

Figure 2.19: Potential-pH equilibrium diagram for the system Mo-H_2O, at 25°C [96].

Also, the repassivation of pits may be facilitated by the decreased chloride activity within the pit caused by the formation of compounds such as MoO_2Cl_2 and precipitation of Mo chlorides [103].

Mn According to Fig. 2.20, the whole domain of thermodynamic stability of Mn lies well below that of water which means it is a very base reducing metal. It is therefore very unstable in the presence of water and tends to react with it with the evolution of hydrogen. However, in practice, this reaction occurs slowly, probably due to the large hydrogen overpotential of the metal. Mn can easily be dissolved by acid and neutral oxidizing solutions with the release of Mn^{2+} ions. Applying further oxidizing action can lead to the formation of solid oxides such as MnO_2, Mn_2O_3 or Mn_3O_4. At even more oxidizing conditions manganate ions, MnO_4^{2-} (at very high pH values), or permanganate ions, MnO_4^-, can be formed. In alkaline solutions, Mn will cover itself with $Mn(OH)_2$ since the anhydrous oxide MnO is, at 25°C, thermodynamically unstable. In very alkaline solutions, the manganous hydroxide is very slightly soluble to give dimanganite ions $HMnO_2^-$. Several studies were dedicated to studying the influence of Mn on the corrosion behaviour of stainless steels. It was found that high concentrations of Mn in the alloy composition diminish the ability of passive film formation, e.g. it yields an increase of the critical current density and of the critical passivation potential

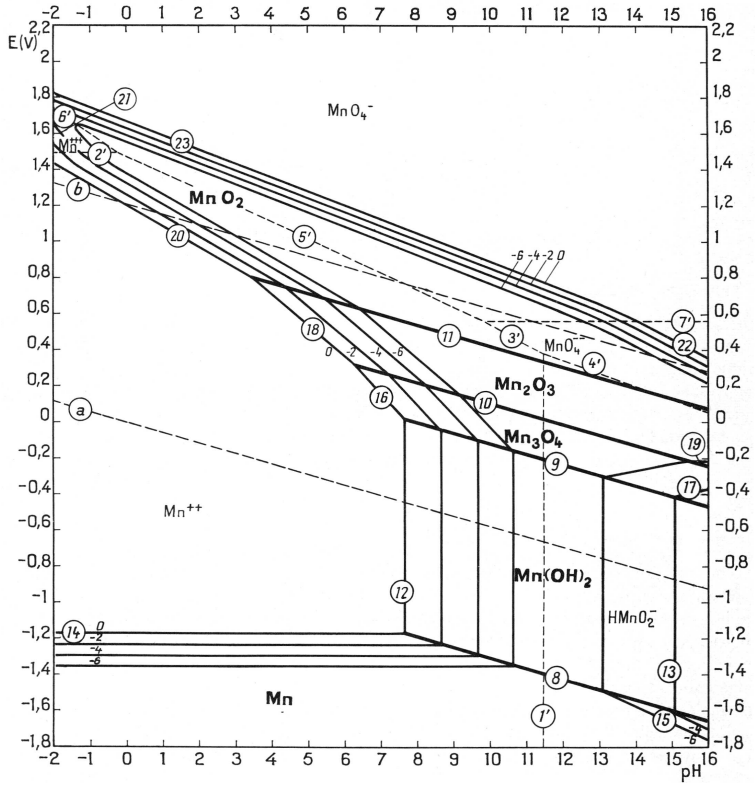

Figure 2.20: Potential-pH equilibrium diagram for the system Mn-H_2O, at 25°C (considering β -MnO_2) [96].

[104]. For some alloys it also determines a decrease of the passive film protection ability which was explained by a decrease in Cr concentration in the passive film [105].

C, B and Y Pure C can exist in the form of diamond, graphite and amorphous carbon. Based on its thermodynamic stability domain, it is theoretically easy to cause C to react, but any possible reaction is highly irreversible and cannot actually be brought about under normal conditions of temperature and pressure. According to thermodynamic calculations, B is a very powerful reducing agent. It tends to decompose water with the formation of boric acid or borates. In practice, this high reactivity is observed only for the amorphous variety of B. Crystalline B is much more resistant. For example, it is not attacked by hydrochloric acid, even when boiling. Y has a very large negative equilibrium potential. As its entire domain of stability lies well below that of water, Y is very unstable in the presence of aqueous solutions of any pH. While in acid and neutral solutions, it dissolves as yttric ions, Y^{3+}, in the presence of alkaline solutions, it covers itself with yttrium hydroxide $Y(OH)_3$ [96].

For easy referencing, Table 2.3 summarizes important reactions of the constituent elements in water solutions in dependence of the pH value.

Table 2.3: Important reactions of elemental Fe, Cr, Co, Mo and Mn in water solutions in dependence of pH value.

	acid solutions	near neutral solutions	alkaline solutions
Fe	$Fe = Fe^{2+} + 2e^-$ $2Fe^{2+} + 3H_2O = Fe_2O_3 + 6H^+ + 2e^-$	$Fe = Fe^{2+} + 2e^-$ $2Fe_3O_4 + H_2O = 3Fe_2O_3 + 2H^+ + 2e^-$	$3Fe + 4H_2O = Fe_3O_4 + 8H^+ + 8e^-$ $2Fe_3O_4 + H_2O = 3Fe_2O_3 + 2H^+ + 2e^-$
Cr	$Cr = Cr^{2+} + 2e^-$ $2Cr^{2+} + 3H_2O = Cr_2O_3 + 6H^+ + 2e^-$ $2Cr + 7H_2O = Cr_2O_7^{2-} + 14H^+ + 12e^-$ $Cr_2O_3 + 4H_2O = Cr_2O_7^{2-} + 8H^+ + 6e^-$	$2Cr + 3H_2O = Cr_2O_3 + 6H^+ + 6e^-$ $Cr_2O_3 + 5H_2O = 2CrO_4^{2-} + 10H^+ + 6e^-$	$Cr + 3H_2O = CrO_3^{3-} + 6H^+ + 3e^-$
Co	$Co = Co^{2+} + 2e^-$ $Co^{2+} + 2H_2O = CoO_2 + 4H^+ + 2e^-$	$Co + H_2O = CoO + 2H^+ + 2e^-$ $2Co^{2+} + 3H_2O = Co_2O_3 + 6H^+ + 2e^-$	$Co + 2H_2O = HCoO_2^- + 3H^+ + 2e^-$ $3HCoO_2^- = Co_3O_4 + 2H_2O + 2e^-$
Mo	$Mo = Mo^{3+} + 3e^-$ $Mo + 2H_2O = MoO_2 + 4H^+ + 4e^-$ $Mo^{3+} + 3H_2O = MoO_3 + 6H^+ + 3e^-$ $MoO_2 + H_2O = MoO_3 + 2H^+ + 2e^-$	$Mo + 2H_2O = MoO_2 + 4H^+ + 4e^-$ $MoO_2 + 2H_2O = MoO_4^{2-} + 4H^+ + 2e^-$	$Mo + 4H_2O = MoO_4^{2-} + 8H^+ + 6e^-$
Mn	$Mn = Mn^{2+} + 2e^-$ $Mn^{2+} + 2H_2O = MnO_2 + 4H^+ + 2e^-$ $MnO_2 + 2H_2O = MnO_4^- + 4H^+ + 3e^-$	$Mn = Mn^{2+} + 2e^-$ $2Mn^{2+} + 3H_2O = Mn_2O_3 + 6H^+ + 2e^-$ $MnO_2 + 2H_2O = MnO_4^- + 4H^+ + 3e^-$	$Mn + H_2O = MnO + 2H^+ + 2e^-$ $Mn + 2H_2O = HMnO_2^- + 3H^+ + 2e^-$ $3HMnO_2^- + H^+ = Mn_3O_4 + 2H_2O + 2e^-$ $MnO_2 + 2H_2O = MnO_4^- + 4H^+ + 3e^-$

3 Experimental

3.1 Materials

Besides the main material of the present study, the bulk glassy $(Fe_{44.3}Cr_5Co_5Mo_{12.8}Mn_{11.2}C_{15.8}B_{5.9})_{98.5}Y_{1.5}$ alloy, two other materials were used in this study. One was a crystalline $(Fe_{44.3}Cr_5Co_5Mo_{12.8}Mn_{11.2}C_{15.8}B_{5.9})_{98.5}Y_{1.5}$ alloy which was investigated in order to analyze the effect of structure on the corrosion behavior. The other material was the commercial steel X210Cr12 which was used as a reference to compare with the bulk glassy $(Fe_{44.3}Cr_5Co_5Mo_{12.8}Mn_{11.2}C_{15.8}B_{5.9})_{98.5}Y_{1.5}$ alloy. Ingots of nominal compositions $(Fe_{44.3}Cr_5Co_5Mo_{12.8}Mn_{11.2}C_{15.8}B_{5.9})_{98.5}Y_{1.5}$ were prepared by induction melting of high purity elements under purified Ar atmosphere and subsequent casting into a copper mold. The melting was repeated several times for homogenization. A section of a resulting rod with 10 mm diameter was investigated in this form and it was denominated 'crystalline $(Fe_{44.3}Cr_5Co_5Mo_{12.8}Mn_{11.2}C_{15.8}B_{5.9})_{98.5}Y_{1.5}$' or 'crystalline counterpart'. As it will be shown later, the denomination 'crystalline' is correct as this rod is composed entirely of crystalline phases attributable to the particular casting conditions. Another section of the rod was fragmented and the fragments were remelted. The melt was subjected to injection casting into a water-cooled copper mould in Ar atmosphere. The resulting rod was 3 mm in diameter and 50 mm in length. This diameter was chosen in order to prevent disintegration of the rod as explained in section 2.1.5. This constitutes the bulk glassy alloy $(Fe_{44.3}Cr_5Co_5Mo_{12.8}Mn_{11.2}C_{15.8}B_{5.9})_{98.5}Y_{1.5}$. The bulk glassy alloy and the crystalline counterpart samples were produced by *Dr. U. Siegel* at IFW Dresden. The X210Cr12 commercial steel (hereafter called 'conventional steel') was used in the as-received state without any subsequent treatments (1 mm thick plate). Its nominal chemical composition is given in Table 3.1. As compared to the glassy alloy, the conventional steel has higher Fe and Cr concentration while the C concentration is lower. It is also missing Co, Mo, B and Y, while Mn has a very low concentration. Additionally, the conventional steel contains a low amount of Si while the glassy alloy is Si-free.

Table 3.1: Nominal chemical composition of the commercial steel X210Cr12 (atomic concentrations derived from weight concentrations considering the mean value).

Element	Cr	C	Si	Mn	Fe
weight %	11.00–12.00	1.90–2.20	0.10–0.40	0.15–0.45	balance
atomic %	~ 11.40	~ 8.80	~ 0.46	~ 0.28	~ 79.06

3.2 Characterization techniques

In order to characterize the microstructure of the three materials selected for the corrosion study, several techniques were employed as will be described in the following.

XRD In the field of amorphous alloys research, X–ray diffraction (XRD) is a very useful tool for evaluating the amorphicity of a sample. While diffractograms of fully crystalline samples comprise distinct sharp reflections which broaden when the grain size decreases to the nanometre range, those of amorphous samples will exhibit broad and shallow peaks corresponding to the SRO and MRO structural state (see section 2.1.3). Samples that contain both crystalline and amorphous phases will provide patterns with a combination of broad and sharp peaks. In the case of crystalline phases, X-rays are diffracted by the crystalline lattice and the distance between atomic planes can be determined with Bragg's relation:

$$n \cdot \lambda = 2 \cdot d \cdot \sin\theta \qquad \text{eq. (3.1)}$$

where n is the diffraction order, λ is the radiation wavelength, d is the distance between atomic planes and θ is the diffraction angle. Analysis of diffraction peaks and comparison with values from specialized databases allows the identification of the phases in many cases if the chemistry of the investigated sample is known. In the case of multiphase samples, the analysis is more difficult as diffraction peaks may overlap. In this case, the Rietveld method is often used [106]. In this method, a least squares approach is used to refine a calculated pattern until it matches the measured pattern. As a result, a volume ratio of the constitutive phases is obtained. In this study, the PowderCell software was used for post-measurement analysis including Rietveld analysis. Details regarding the crystalline structure of various phases were extracted from the ICSD database (Inorganic Crystal Structure Database) [107].
The XRD measurements were performed with a XPertPro Phillips diffractometer using $CoK_{\alpha 1}$ radiation. The measurements were done in step mode with a step size of 0.05° and 42 s per step from 20° to 120°. The bulk glassy alloy and its crystalline counterpart were prepared as follows

for the XRD analysis: a volume of approximately 140 mm^3 of each has been fragmented and the resulting powder was glued to an amorphous silica holder with Zapon lacquer (cellulose nitrate in amyl acetate solvent). In the case of the conventional steel, a 1 mm thick plate with 10x10 mm cross-section was used.

HRSEM High resolution scanning electron microscopy (HRSEM) investigations of the bulk glassy alloy sample were performed in order to identify possible crystalline inclusions or other defects, e.g. pores. For the crystalline counterpart and the conventional steel HRSEM was used for observing and characterizing their microstructure. The principle of the SEM is rather simple: an electron beam scans the sample surface and various kinds of radiation emitted as a result are collected in suitable detectors and used for image formation [108]. The most popular techniques are the secondary electron mode which reveals surface topography (and in some situations also atomic-number and crystal-orientation contrast) and the backscattered electron mode which gives both topographic and materials contrast. In the present study, the secondary electrons mode was used. The low energy *secondary electrons* are formed as a result of the interaction between the primary electrons and loosely bound atomic electrons. In the present study, HRSEM investigations were performed with a Gemini Leo 1530 instrument. The acceleration voltage was 1–20 kV and all the images were done in the secondary electron mode. Energy dispersive x-ray analysis (EDX) was also performed. This technique is based on the fundamental principle that each element has a unique atomic structure which allows its characteristic X-rays to be used for its identification [109]. The electrons of the incident beam excite inner shell electrons of atoms in the analyzed sample, determining their ejection and resulting in the formation of electron holes within the electronic structure of those atoms. Electrons from an outer shell then fill these holes and the excess energy of those electrons is released in the form of X-ray photons. The release of these X-rays creates spectral lines that are specific to individual elements. This way the X-ray spectrum can be analyzed to identify the constituent elements of the analyzed sample and also to determine their concentration.

In order to reveal its microstructure, a cross-section of the crystalline counterpart was polished to 0.04 µm SiO_2 suspension (OP-U, Struers) and then etched for 5 s with Nital 3%. The glassy alloy and the conventional steel were only polished (same polishing procedure as for the crystalline counterpart sample).

TEM In order to further check the bulk glassy alloy sample for any crystalline inclusions at higher magnification transmission electron microscopy (TEM) was applied. In principle, similarly to SEM, TEM is also using an electron beam to probe the sample. However, the energy of the primary electrons is higher, e.g. typically 200 kV, and most of the analysis is done in transmission mode. The most common contrast used in TEM is the bright field

contrast. A bright field image is formed when only the diffracted beam is used for imaging [110]. Electron diffraction patterns and the chemical composition of selected areas in the samples can also be obtained in the TEM. TEM investigations were performed by *Ms. C. Mickel* at IFW Dresden with a Tecnai T20 instrument. An acceleration voltage of 200 kV was used and bright field images as well as diffraction patterns and EDX spectra were acquired. The samples for TEM were prepared from the original rod by cutting thin slices (approx. 1 mm) which were subsequently thinned by mechanical polishing and then by ion milling.

AES In addition to the above described techniques, Auger electron spectroscopy (AES) was used. AES was performed on bulk glassy $(Fe_{44.3}Cr_5Co_5Mo_{12.8}Mn_{11.2}C_{15.8}B_{5.9})_{98.5}Y_{1.5}$ alloy samples in the as-polished state and after selected electrochemical tests. This technique allows the determination of concentration–depth profiles in surface-near regions which serve for the characterization of surface films, e.g. native or anodically formed passive films, and the sub-film region. In AES the sample is irradiated with electrons which cause the core electrons of atoms in the sample to be ejected [111]. In order for the so ionized atom to return to its ground state, it is possible that another electron from a higher level fills the core hole. The energy released in this process is used for the ejection of another electron out from the atom which is called an *Auger electron*. The kinetic energy of the Auger electrons is measured by a detector. Each element has a characteristic spectrum. When a multielement sample is analyzed, the relative intensities of peaks are analyzed and are the basis for the calculation of atomic concentrations. In order to determine a concentration–depth profile, AES spectra are recorded in combination with intermediate sputtering. The measurements and the subsequent determination of the concentration–depth profiles were performed by *Dr. S. Baunack* at IFW Dresden. The investigations were carried out using an Auger microprobe PHI 660. The sputtering was done with Ar ions impinging under 60° with an energy $E_{ion} = 1.5$ keV. The thickness of oxide layers was estimated using the reference sputter rate of SiO_2 which is approximately 2.8 nm·min^{-1}. The interface film/alloy was considered to correspond to the point where the oxygen concentration is reduced to 50% of its maximum. Because of the multitude of constitutive elements, Auger peaks strongly overlap and were separated by data analysis techniques (linear least squares fit to standard spectra and factor analysis)

3.3 Corrosion related methods

For fundamental corrosion investigations, weight loss tests and various electrochemical polarization methods were employed. Before presenting details about these techniques, the electrolytes used are given.

Electrolytes The electrolytes used for these tests are shown in Table 3.2.

Table 3.2: The electrolytes used for the weight loss and electrochemical tests.

pH	Solution
0.1	1 M HCl
0.3	0.5 M H_2SO_4
5	0.00001 M H_2SO_4 0.1 M Na_2SO_4[a] 0.5 M Na_2SO_4[a] 0.5 M phthalate buffer
8.4	0.1 M Na_2SO_4[b] 0.3 M borate buffer
11	0.001 M NaOH
14	1 M NaOH
7	0.01 M NaCl[c] 0.1 M NaCl[c] 0.6 M NaCl[c]

[a] pH value was adjusted with H_2SO_4.
[b] pH value was adjusted with NaOH.
[c] electrolytes used for pitting tests.

The 0.5 M phthalate buffer solution was prepared by mixing 240 mL of 0.1 M NaOH with 760 mL bi-distilled water and 1 L of 0.1 M potassium hydrogen phthalate $C_8H_5O_4K$ solution. To prepare 1L of 0.3 M borate buffer solution, 9.25 g boric acid (H_3BO_3) and 14.3 g borax ($Na_2B_4O_7 \cdot 10\,H_2O$) were dissolved in bi-distilled water. Additionally, three other solutions were used for the pitting investigations: 0.01, 0.1 and 0.6 M NaCl.
For the weight loss tests, 1 mm thick disc samples of the glassy alloy (3 mm in diameter) and 9x7x1 mm samples of the conventional steel were used. For electrochemical testing, the samples were electrically connected and embedded in epoxy resin so that only their cross-section was exposed to the electrolyte. Before every test, the sample surface was ground with emery paper down to grid 4000 and then polished with 1 µm diamond suspension.

Weight loss In order to determine the free corrosion rate of the bulk glassy alloy relative to that of the conventional steel, weight loss tests were performed under four different conditions:

very acidic (0.5 M H_2SO_4), very basic (1 M NaOH), neutral aggressive chloride solution (0.6 M NaCl) and a less aggressive neutral solution (0.1 M Na_2SO_4). Immersion tests were not performed for the crystalline counterpart alloy because those samples were difficult to handle due to extreme brittleness leading to an uncontrolled loss of material. The samples were immersed in the respective solutions and periodically emerged (see next chapter for the periods), rinsed with distilled water, weighed, microscopically investigated and re-immersed. For the weight measurements a Mettler Toledo XS205 analytical balance was employed. The weight loss, Δm, was calculated with respect to the starting surface area of the samples.

Electrochemical methods The electrochemical measurements were carried out with a Solartron SI 1287 electrochemical interface connected to a cell with a three electrode arrangement using a Pt net as counter electrode and a saturated calomel electrode (SCE) ($E = 241$ mV vs. SHE) as reference electrode. The electrolytes were purged with N_2 for one hour before and during each test. After monitoring the open circuit potential (OCP) for 1 hour, potentiodynamic polarization measurements in the anodic regime were performed. The dynamic polarization was started from the cathodic regime (about -100 mV vs. OCP) and linearly swept in the anodic direction at a rate of 0.2 $mV \cdot s^{-1}$ until O_2 evolution set in or the current became excessively high. In order to achieve a high reliability of the results, all electrochemical measurements were repeated at least two times. After selected potentiodynamic polarization tests in NaCl electrolytes, SEM images were taken from the surface of the glassy alloy and of its crystalline counterpart. In order to remove the corrosion products from the surface, prior to SEM investigations, the samples were immersed for 2 h into an agitated saturated Chelaplex $C_6H_9O_6N$ solution. In the case of the conventional steel, light optical microscopy (LOM) was used. Cleaning with Chelaplex was not done in order to prevent losing the weakly bonded carbides (due to excessive dissolution of the surrounding matrix).
For the analysis of the anodic polarization curves, a number of corrosion-related parameters were evaluated. These parameters are identified in the schematic polarization curve (Fig. 3.1) for an electrode in acid solution exhibiting typical active-passive behaviour [71]. The plot demonstrates the dependence of the potential versus the logarithm of current density, whereby the current density is the measured external-circuit current divided by the area of the sample surface exposed to electrolyte. The sample potential is controlled by a potentiostat. It can be regarded as the driving force for corrosion, while the anodic current density is related to the specimen dissolution rate. Only in a few cases, the measured current density reflects other additional reactions such as the oxygen evolution reaction as shown in Fig. 3.1. The potential scan is started at potentials more negative than the corrosion potential, E_{corr}, i.e. in the cathodic regime where reduction reactions occur which cause a cathodic current, e.g. the hydrogen reduction reaction (HER) or metal deposition. It is, however, possible that metal dissolution occurs even at these potentials though not visible in the potential-current

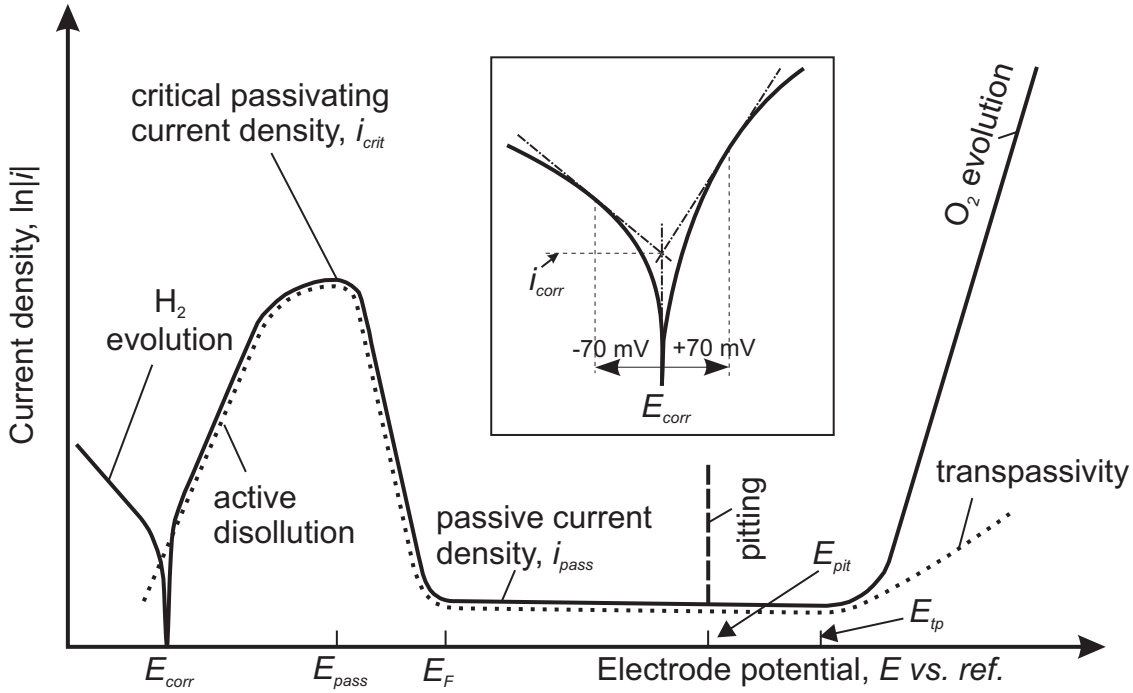

Figure 3.1: Schematic current-potential curve for a passivating electrode. Solid curve: total current-potential curve. Dotted: partial current-potential curve for metal dissolution [71]. Inset: schematic illustration of the graphical method used in this thesis for determining the corrosion current density, i_{corr}.

diagram because of the superimposed high cathodic reaction current. At E_{corr} the external measured current goes to zero meaning not that no corrosion is taking place, but that the anodic current is equal to the cathodic current. In order to determine the corrosion current density, i_{corr}, the graphical extrapolation method was used [112], shown schematically in the inset of Fig. 3.1. For this, the intersection point of the vertical line corresponding to E_{corr} with the tangents on the anodic and cathodic branches at overpotentials of about $\pm$70 mV was determined. Furthermore, with increasing anodic potential, the current density increases indicating that the metal dissolution rate increases. The alloy undergoes active dissolution up to a potential where it reaches a short plateau at high current densities corresponding to a pre-passivation state. This limiting current density is the critical passivating current density, i_{crit}, because it corresponds to the situation of accumulation of passivating species at the electrode surface in concentrations sufficient for the formation of a passive film composed of solid oxides, hydroxides or salts. This leads in turn to a transfer into the passive state of the surface clearly indicated by a rapid decrease in current density by several orders of magnitude. The potential at which this decrease begins is termed the passivation potential, E_{pass}. The potential at which the current density stops to decrease rapidly is the activation potential or the Flade potential, E_F. This potential is also observed as a temporary arrest when an electrode passivated previously is left to activate spontaneously [71]. From this potential, the

alloy is in the passive state as it is covered by a protective film which acts as a barrier for metal ion release and thus, allows only a very small dissolution rate. The permeability of the film is measurable in terms of the passive current density, i_{pass}, a value corresponding to the current density plateau. At potentials higher than the equilibrium potential of the water decomposition reaction, $E^0(H_2O/O_2)$, oxygen evolution will set in and this will cause an increase in current density. The level of the current density for this reaction is determined by the porosity of the passive layer when H_2O oxidation takes place on the metal surface, and by the electron conductivity of the passive film when H_2O oxidation takes place on the film surface. However, parallel to this reaction, transpassivation may occur meaning that the passive film breaks down and further metal reactions are possible. The potential at which this happens is termed the transpassive or breakdown potential, E_{tp}. As seen in Fig. 3.1, this potential is not always detectable as it can be superposed by the water oxidation reaction. If the investigated alloy undergoes pitting corrosion as for example in environments containing halide ions (F^-, Cl^-, Br^-), a somewhat different scenario occurs. Halide ions are known to locally destabilize the passive film. In this case, the passive film may break down at a potential lower than the transpassive potential. This breakdown is often clearly marked by a sudden increase in current density as shown by the dashed line in Fig. 3.1. The slope of this increase relates to the pit growth rate. The potential at which stable pits are nucleated is the pitting potential, E_{pit}. However, prior to E_{pit}, metastable pitting may occur and this is reflected in a more or less pronounced noise-like shape of the $i - E$ curve (not shown in Fig. 3.1).

3.4 Ex situ and in situ AFM

In order to better understand the global corrosion reaction mechanism, local corrosion analysis at high magnification by techniques such as atomic force microscopy (AFM) are necessary. AFM is a scanning probe microscopy (SPM) technique, which utilizes a sharp tip mounted onto a cantilever spring to scan the sample surface and to monitor its topography [108]. Principally, when the AFM tip approaches the sample surface, it will experience forces which can be schematically represented as in Fig. 3.2. When the tip is very close to the sample surface, i.e. below ∼0.5 nm, it will be repulsed due to electrostatic repulsion of the electron clouds of the atoms of tip and sample. This is where the tip is operated in contact mode. At larger tip-sample distances, the tip will be attracted towards the sample due to long-range van der Waals forces. This is where the non-contact mode is operated. As the tip scans the surface, it will be deflected depending on the surface topography. A simplified diagram of an AFM device is shown in Fig. 3.2. A laser source is used to emit a laser beam which is directed on the backside of the cantilever where it is reflected and subsequently detected by a

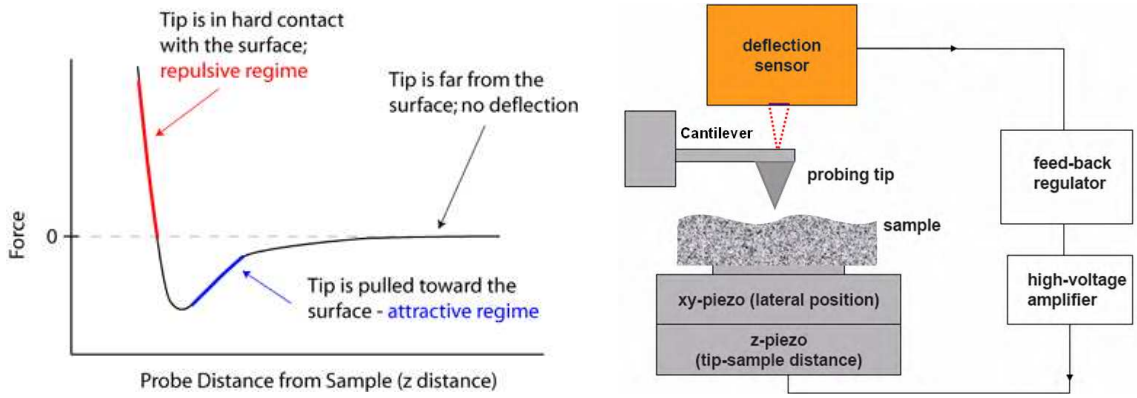

Figure 3.2: Left: force versus distance curve for sample-probe interaction in AFM [113]. Right: block diagram of AFM [114].

4-quadrant photodetector. The signal of this detector is fed into a feed-back regulator which will dictate the Z-piezo movement.

AFM has several modes of operation such as contact mode, non-contact mode and tapping mode. In this work, contact mode was used for the in situ measurements. In contact mode, as the tip scans the surface, it is deflected by the surface corrugation. The tip is constantly adjusted to maintain a constant deflection and, therefore, a constant height above the surface. It is this adjustment that is displayed as data. For the ex-situ measurements, non-contact mode was used. In non-contact mode, a stiff cantilever is oscillated in the attractive regime, consequently the tip is quite close to the sample surface, but does not touch it (hence, 'non-contact'). The detection scheme is based on measuring changes in the resonant frequency or amplitude of the cantilever.

One of the advantages of AFM is that it can be operated in air at atmospheric pressure and also in liquids. This is a major benefit for corrosion science as it allows in situ imaging of surface morphology changes during corrosion processes as they occur in the environment of interest and, thus, eliminating any artefacts related to the removal of the sample from the environment. A Park XE-100 instrument (Fig. 3.3) was used for both ex situ and in situ measurements on the bulk glassy $(Fe_{44.3}Cr_5Co_5Mo_{12.8}Mn_{11.2}C_{15.8}B_{5.9})_{98.5}Y_{1.5}$ alloy. The ex situ measurements were performed in air at room temperature after 200 days of exposure to 0.5 M H_2SO_4. The in situ tests were performed in order to study the initial stages of dissolution in the same solution, 0.5 M H_2SO_4. The cell used for these tests is shown in Fig. 3.3. The typical three electrode setup was used in conjunction with an external potentiostat in order to realize similar conditions as in the 'bulk' electrochemical cell used for the polarization studies. A Teflon capillary was the link between the cell and the SCE used as reference electrode. As counter electrode a Pt wire was used. During the measurements, the cantilever was fully immersed in the electrolyte. In order to be able to observe the very small initial topography changes, a very flat original surface is required. For this, the sample was ground with emery

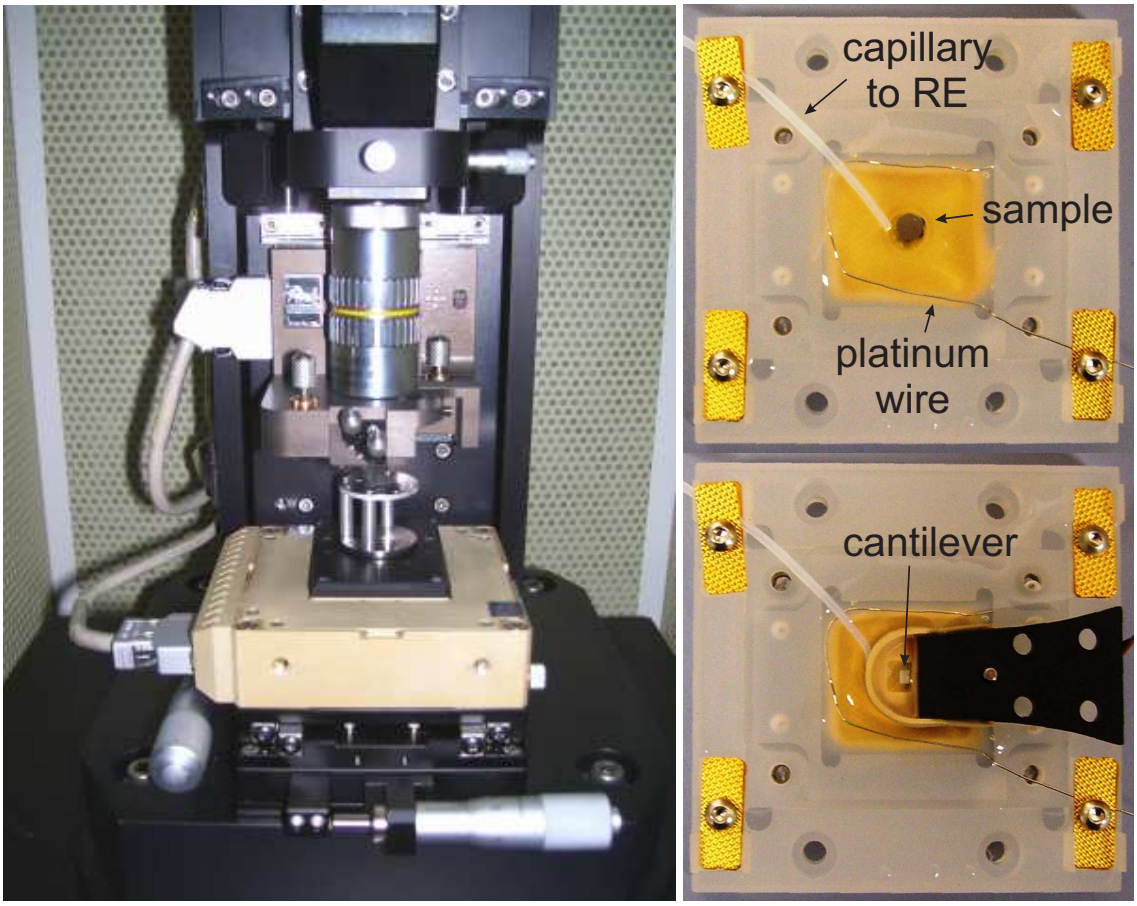

Figure 3.3: Left: photograph of the AFM Park XE-100 instrument employed in this study. Right: photographs of modified electrochemical cell used for the in situ AFM investigations. Top: sample is visible. Bottom: position of cantilever as during actual measuring is visible.

SiC paper from grit 400 down to grit 4000 and then polished using 1 µm diamond, 0.2 µm and 0.04 µm SiO_2 suspensions. Finally, the sample was cleaned similarly as for the electrochemical tests.

4 Results and discussion

Generally, the microstructure of an alloy sample has a strong influence on the corrosion behaviour. Therefore, this chapter begins with a section on the microstructure characterization of the three subject materials. The following sections focus on the analysis of the free corrosion, the anodic polarization behaviour and the passivation ability of the bulk glassy $(Fe_{44.3}Cr_5Co_5Mo_{12.8}Mn_{11.2}C_{15.8}B_{5.9})_{98.5}Y_{1.5}$ alloy in dependence of the pH value of the electrolyte. A separate section is devoted to the evaluation and description of its pitting behaviour. For some particular aspects, a comparison is made with the crystalline counterpart alloy and with the commercial steel X210Cr12. As described in the introduction the morphology of a corroding surface strongly depends on the structure of the corroding material. While this aspect was thoroughly studied for crystalline alloys, only few studies with respect to this were done for amorphous alloys. In the final section of this chapter results of detailed investigations regarding active dissolution in acid solutions with a special focus on the morphology evolution are presented.

4.1 Microstructure characterization

4.1.1 The bulk glassy $(Fe_{44.3}Cr_5Co_5Mo_{12.8}Mn_{11.2}C_{15.8}B_{5.9})_{98.5}Y_{1.5}$ alloy

The microstructure of the cast sample with 3 mm diameter was investigated by XRD, SEM and TEM which were presented in section 3.2. Figure 4.1(a) represents the XRD pattern of the bulk glassy $(Fe_{44.3}Cr_5Co_5Mo_{12.8}Mn_{11.2}C_{15.8}B_{5.9})_{98.5}Y_{1.5}$ sample. In this pattern only broad diffuse maxima can be observed indicating that the sample has a mainly amorphous structure. However, local observations of the structure at the nanoscale performed by TEM investigations revealed the presence of crystalline polyhedral particles which are embedded in the glassy matrix. Two TEM micrographs of such particles are shown in Fig. 4.2. Typically, these particles are smaller than 200 nm in size. Their crystalline nature was clearly evidenced by electron diffraction. Two electron diffractograms are shown in the inset of Fig. 4.2(a). They provide clear evidence of the amorphous and crystalline state of the matrix and of the particle, respectively. In order to measure the chemical composition of these particles, EDX

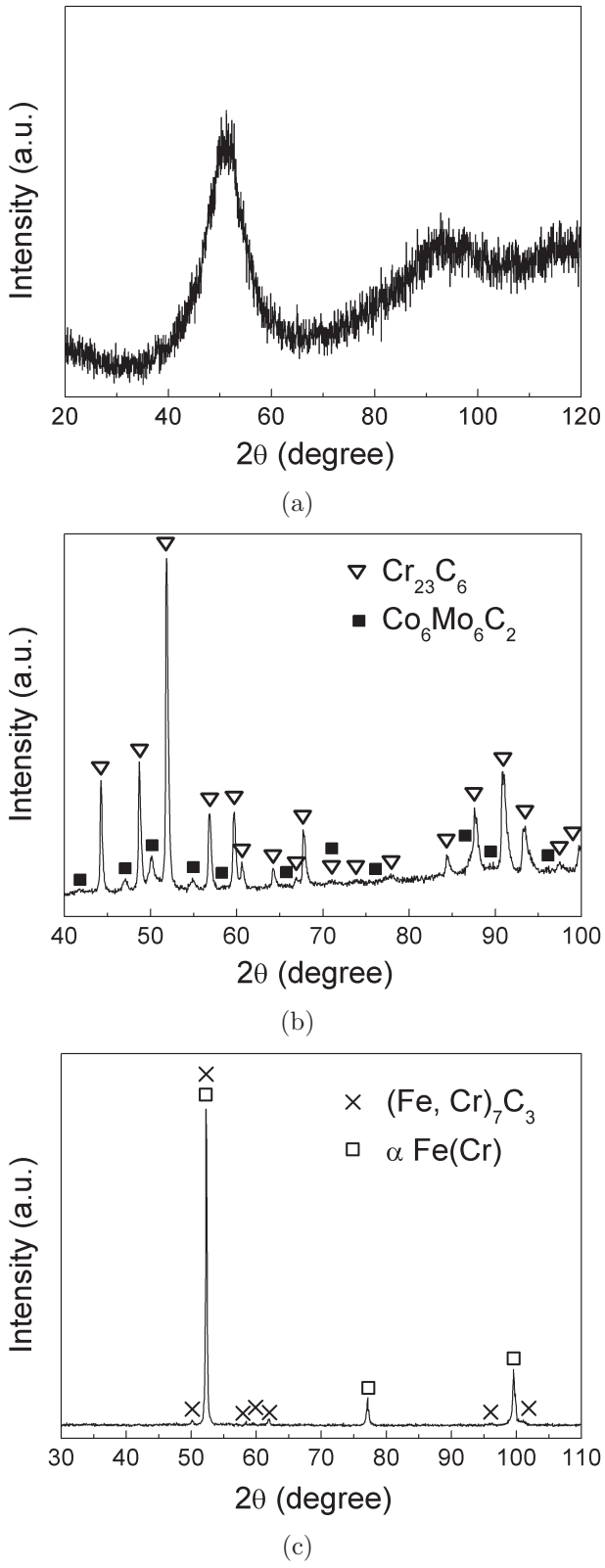

Figure 4.1: XRD patterns of: a) the bulk glassy $(Fe_{44.3}Cr_5Co_5Mo_{12.8}Mn_{11.2}C_{15.8}B_{5.9})_{98.5}Y_{1.5}$ alloy sample with 3 mm diameter, b) the crystalline $(Fe_{44.3}Cr_5Co_5Mo_{12.8}Mn_{11.2}C_{15.8}B_{5.9})_{98.5}Y_{1.5}$ sample, and c) the commercial steel X210Cr12 sample.

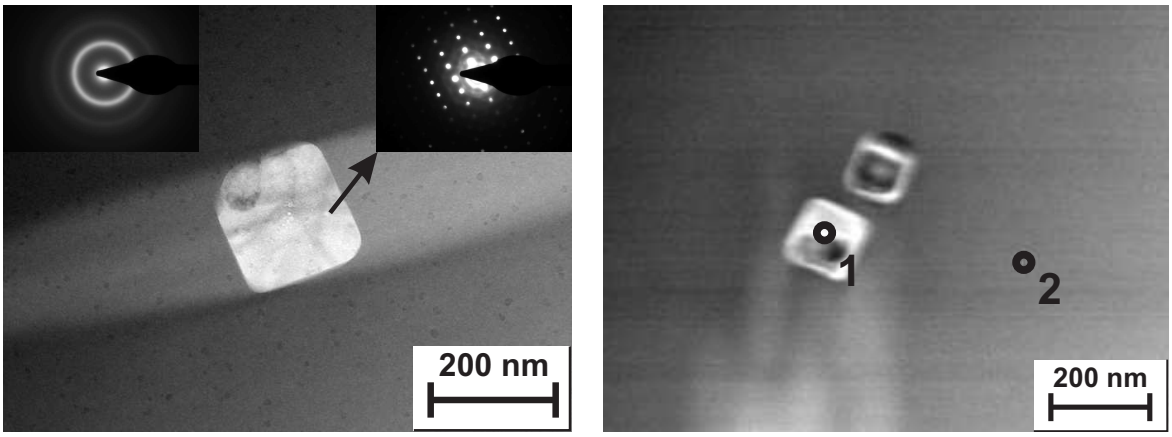

(a) (b)

Figure 4.2: TEM micrographs of sections of the bulk glassy $(Fe_{44.3}Cr_5Co_5Mo_{12.8}Mn_{11.2}C_{15.8}B_{5.9})_{98.5}Y_{1.5}$ alloy. a) crystalline polyhedral particle of Y_2O_3 embedded in the matrix. Inset: electron diffraction patterns of the amorphous matrix (left) and of the crystalline particle (right); b) indication of two locations where EDX analysis was performed; see Table 4.1.

investigations have been performed. Details of a representative measurement are summarized in Fig. 4.2(b) and in Table 4.1.

Table 4.1: TEM-EDX analysis of crystalline polyhedral particles in a bulk glassy $(Fe_{44.3}Cr_5Co_5Mo_{12.8}Mn_{11.2}C_{15.8}B_{5.9})_{98.5}Y_{1.5}$ alloy sample (concentrations given in at.%).

Location index	Fe	Cr	Co	Mo	Mn	Y	O
1 (particle)	1.60	0.00	0.00	1.49	0.10	43.18	53.61
2 (matrix)	57.03	5.90	3.74	20.03	12.14	1.13	0.00

As it can be seen, the particle consists mainly of Y and O. As the stoichiometry is close to Y:O = 2:3, it was concluded that the particle is composed of yttrium oxide, Y_2O_3. A series of particles was also analyzed and similar results were obtained. Only in the case of a few particles some other elements, e.g. Mo, Fe, were also enriched in the Y_2O_3 particles.
As revealed by SEM which enables the analysis of a wider cross-sectional area of the sample, the 3 mm diameter rod contains only a low fraction of Y_2O_3 polyhedral particles. Due to the low fraction of these particles, they could not be detected by XRD. These particles usually reside in groups and the distance between such groups is on average in the order of tens of microns. Figure 4.3(a) shows a SEM image of such a group. These particles could have been formed during the preparation process due to the high affinity of Y to O ($\Delta_f G^o(Y_2O_3)$

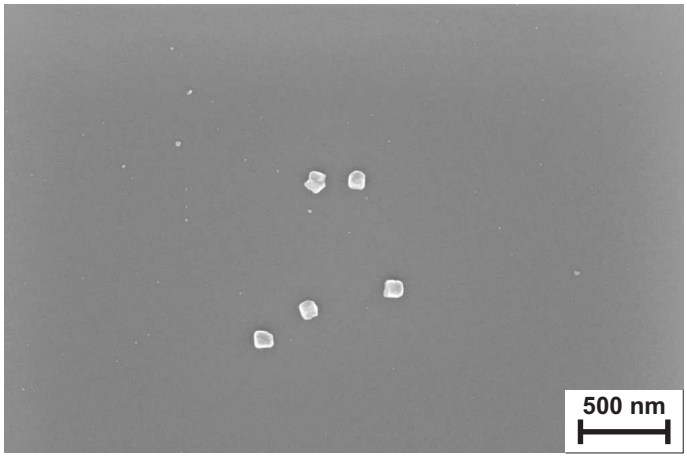

(a)

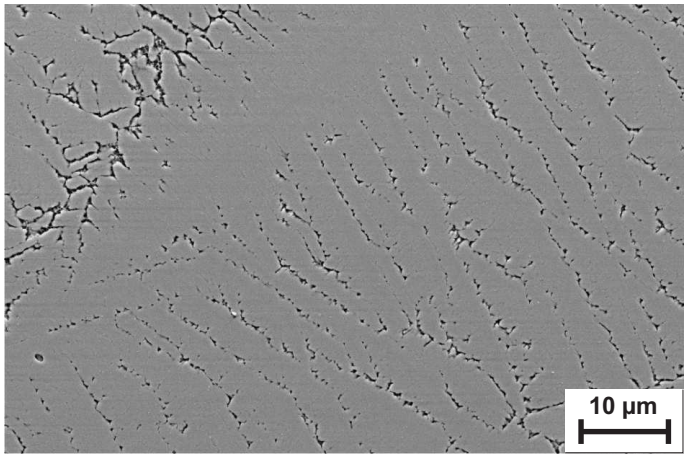

(b)

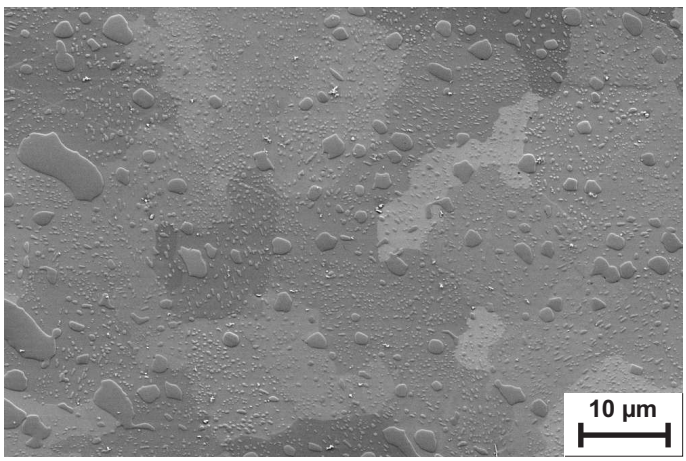

(c)

Figure 4.3: SEM images of the cross-sectional area of: a) the cast bulk glassy $(Fe_{44.3}Cr_5Co_5Mo_{12.8}Mn_{11.2}C_{15.8}B_{5.9})_{98.5}Y_{1.5}$ alloy rod sample with 3 mm diameter, b) the cast crystalline $(Fe_{44.3}Cr_5Co_5Mo_{12.8}Mn_{11.2}C_{15.8}B_{5.9})_{98.5}Y_{1.5}$ rod sample with 10 mm diameter, and c) the commercial steel X210Cr12 sample.

$= -1932\,\mathrm{kJ{\cdot}mol^{-1}}$ [115]) and the unavoidable presence of minimal O contents in the melt during casting. SEM investigations on a 3 mm diameter sample of the same alloy performed by Siegel [40] also revealed the presence of Y_2O_3 particles. Their volume fraction was under 1 % which explained, as in the case of the present study, the lack of sharp peaks in the x-ray diffraction pattern. However, the sample studied by Siegel contained, besides the sub-micrometre particles as in the case of the samples in the present study, also larger particles, i.e. micrometer sized, and, additionally, more particles were found in agglomerations. Y oxide particles with size in the micrometre and sub-micrometre range were also found in a bulk glassy $Fe_{61}Y_2Zr_8Co_6Al_1Mo_7B_{15}$ alloy sample with l5 mm diameter by Lu et al. [7].

4.1.2 The crystalline $(Fe_{44.3}Cr_5Co_5Mo_{12.8}Mn_{11.2}C_{15.8}B_{5.9})_{98.5}Y_{1.5}$ alloy

An XRD pattern of the crystalline counterpart is shown in Fig. 4.1(b). Due to the numerous peaks corresponding to the multitude of stable and metastable intermetallic compounds that could be formed in this system, it is difficult to clearly identify the phase composition of this sample. However, taking into account the B and C affinity of the constitutive elements, some phases appear to be more favourable than others. The main phase, identified as of the $Cr_{23}C_6$ type, can be designated by the general formula $(Fe,Cr,Mn,Co,Mo)_{23}(B,C)_6$. There is another set of peaks which can not be related to the same compounds. They were found to match the η-carbide structure-type [116]. This secondary phase can be for example Co_3Mo_3C or Mn_3Mo_3C. According to the Rietveld analysis the volume fraction of this phase is 16 %. However, if we consider that only these two phases constitute the microstructure, the ratio of metal to metalloid atoms (M:Me=4.08:1) would be higher than the actual value (M:Me=3.68:1). To account for this, a third phase, rich in metalloids, should be present. Considering also the strong lanthanide-metalloid interactions [3] and the very probable low solubility of Y in $M_{23}(B,C)_6$ and in the η-carbide phases, it might be expected that this phase is a Y-metalloid compound such as FeY_2C_4. However, peaks of this phase do not appear in the diffraction pattern of this alloy, but its concentration can be below the detection limit of the XRD method, i.e. $\sim$ 5 vol.%.

Previous work related to similar alloys suggested different phase compositions, but they all agree on $M_{23}(B,C)_6$ (M = Fe,Cr,Mo,Mn) as the main phase [3, 8, 117, 118]. However, besides the M_6C (η-carbide), Miller et. al. [117] observed a third phase enriched with Y which they assigned as $Fe_{14}Y_2B$ (for the alloy in their study M:Me=3.93:1). As stated in section 2.1.5, annealing a bulk glassy $(Fe_{44.3}Cr_5Co_5Mo_{12.8}Mn_{11.2}C_{15.8}B_{5.9})_{98.5}Y_{1.5}$ alloy sample at 1273 K leads to complete devitrification. As XRD investigations show, the microstructure after this treatment comprises three phases: $M_{23}(B,C)_6$, $Mo_3(Co,Fe)_3C$ and $Mo_{12}(Co,Fe)_{22}C_{10}$ [40]. The $Mo_{12}(Co,Fe)_{22}C_{10}$ phase was not found in the present study to be part of the microstructure of the crystalline counterpart while the FeY_2C_4 phase which is possibly in the microstructure

of the crystalline counterpart was not stated to be found in the annealed sample (see Ref. [40]). This difference is believed to be due to the thermal history of the samples, e.g. during the annealing treatment of the glassy sample, firstly the $M_{23}(B,C)_6$ and the $Mo_3(Co,Fe)_3C$ phases are formed and only subsequently the $Mo_{12}(Co,Fe)_{22}C_{10}$ is formed from the probably not-yet-crystallized remaining phase with modified chemical composition (different from $(Fe_{44.3}Cr_5Co_5Mo_{12.8}Mn_{11.2}C_{15.8}B_{5.9})_{98.5}Y_{1.5}$), however, in the case of the crystalline counterpart sample, this phase, i.e. $Mo_{12}(Co,Fe)_{22}C_{10}$, probably can not form directly from the melt, because there is not yet a domain with the required chemical composition for its formation as in the case of the annealed sample.
In Fig. 4.3(b) a SEM image of the crystalline counterpart is shown. The microstructure is mainly composed of lamellar grains. There is also another phase located at the intergranular region which is preferentially dissolved during etching. It is reasonable to expect the intergranular phase to be η-carbide as detected by XRD and the grains to be the $M_{23}(B,C)_6$ phase. In order to clarify the composition of each phase, EDX point analysis was performed. Unfortunately, the differences in the measured concentration values were very low and consequently, considered to be insignificant. This should be due to the rather low dimension of the interdendritic phase(s) (< 200 nm), lower than the spatial resolution limit of the EDX setup used.

4.1.3 The commercial steel X210Cr12

In Fig. 4.1(c), an XRD pattern of the X210Cr12 steel sample is shown. This pattern can be indexed by assuming two phases: an αFe-based solid solution with Cr as solute and the carbide $(Fe,Cr)_7C_3$. This phase composition corresponds to the equilibrium situation [119]. A SEM image of the conventional steel sample is shown in Fig. 4.3(c). The microstructure of this alloy is composed of equiaxed grains with an average size of 10 µm and particles with a wide size distribution from tens of nanometres to tens of micrometres. An EDX analysis (carbon was not included in the analysis) shows that the particles, which are obviously the carbide, contain 51 at. % Fe and 49 at. % Cr and the grains 94 at. % Fe and 6 at. % Cr. Nevertheless, the concentration of Fe and Cr in the grains (the αFe(Cr) solid solution) as measured by EDX might not represent the real values because fine particles of carbides are very closely present and the measurement might be influenced by these. In consequence, the concentration of Cr in the matrix should be considered to be less than 6 at. %. For the refinement of the XRD pattern, the Fe based solid solution is considered to contain 5 at. % Cr.

Summary For the cast *bulk glassy* $(Fe_{44.3}Cr_5Co_5Mo_{12.8}Mn_{11.2}C_{15.8}B_{5.9})_{98.5}Y_{1.5}$ alloy samples with 3 mm diameter a mainly single phase glassy state was confirmed, but also the

presence of a few dispersed nanometre-sized yttrium oxide Y_2O_3 particles. On the contrary, its crystalline counterpart obtained by casting with slower cooling rate (10 mm diameter rod sample) and the conventional steel X210Cr12 have multi-phase crystalline microstructures. Mainly $M_{23}(B,C)_6$ dendrites, an interdendritic η-carbide as a secondary phase and probably FeY_2C_4 as a third phase, compose the crystalline counterpart. In the conventional steel, $(Fe,Cr)_7C_3$ particles are surrounded by an αFe(6 at.%Cr) solid solution matrix phase. While both the crystalline counterpart and the conventional steel are crystalline alloys, what differentiates them from each other with regard to microstructure is the volume fraction of carbides: the crystalline counterpart sample is comprised entirely of (boro-)carbides while the conventional steel contains a limited amount of carbides. i.e. $\sim 29\%$. This particular steel was chosen as a reference material for this study because it has a high content of C which is closer to that of the bulk glassy alloy than that of most other steels.

4.2 Free corrosion behaviour

For determining the free corrosion rate of the bulk glassy alloy $(Fe_{44.3}Cr_5Co_5Mo_{12.8}Mn_{11.2}C_{15.8}B_{5.9})_{98.5}Y_{1.5}$ weight loss tests were performed in four different solutions: very acidic (0.5 M H_2SO_4), very basic (1 M NaOH), neutral aggressive chloride solution (0.6 M NaCl) and a less aggressive neutral solution (0.1 M Na_2SO_4). Additionally, the same tests were performed for the conventional steel as a reference. Weight loss tests were not performed for the crystalline counterpart alloy because this sample was difficult to handle due to its extreme brittleness leading to an uncontrolled loss of material. Figure 4.4 shows the weight loss curves of the bulk glassy alloy and the conventional steel in the above given solutions. In general, the bulk glassy alloy showed much lower corrosion rates than the reference steel in all electrolytes. Remarkably, the behaviour of the two alloys in 0.5 M H_2SO_4 is very different: while the glassy alloy lost $6\,mg{\cdot}cm^{-2}$ after 100 days, the conventional steel sample lost $200\,mg{\cdot}cm^{-2}$ after only 0.83 days. In 0.6 M NaCl, 0.1 M Na_2SO_4 and 1 M NaOH solutions, the glassy alloy had an insignificant weight loss even after 100 days proving a very high resistance in these solutions. Comparatively, the conventional steel exhibited appreciable weight losses in 0.6 M NaCl and 0.1 M Na_2SO_4, but an insignificant weight loss in 1 M NaOH. As shown in Fig. 4.4, the bulk glassy alloy exhibits slightly negative weight changes, i.e. weight gains, in 0.1 M Na_2SO_4 and in 1 M NaOH. This is attributed to the formation of corrosion products attached to the surface. In the case of the sample immersed in 0.1 M Na_2SO_4, the presence of corrosion products is also evidenced by a change in colour of the surface.

In order to better understand the remarkable difference in the corrosion rate between the glassy alloy and the conventional steel in 0.5 M H_2SO_4, SEM investigations were performed

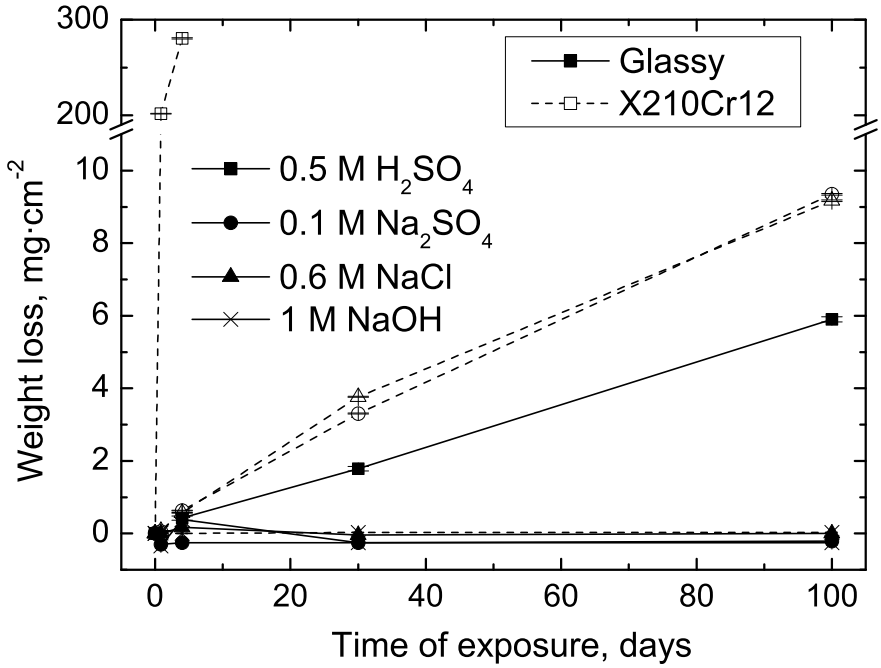

Figure 4.4: Weight loss measurement results of the bulk glassy alloy $(Fe_{44.3}Cr_5Co_5Mo_{12.8}Mn_{11.2}C_{15.8}B_{5.9})_{98.5}Y_{1.5}$ and of commercial steel X210Cr12 samples in 0.5 M H_2SO_4, 0.1 M Na_2SO_4, 0.6 M NaCl and 1 M NaOH.

on the surface of the samples after the aforementioned periods of immersion. The attack of the glassy alloy is initiated by near-hemispherical regions (see Fig. 4.5(a)). Their uniform distribution and round shape prove the purely electrochemical nature of the dissolution process without any influence from possible microstructural irregularities. Figure 4.5(c) shows a SEM image of the conventional steel sample after immersion for 0.83 days. The α-Fe(Cr) matrix was preferentially dissolved. This implies that the matrix and the carbide particles have significantly different nobility which causes a strong galvanic coupling between the two phases. Considering the similar multiphase nature of the crystalline counterpart, galvanic coupling is expected also in the case of this alloy. In contrast, the monolithic single-phase glassy alloy sample does obviously not exhibit this effect. In conclusion, the single-phase nature of the glassy alloy, as contrary to the multiphase nature of the crystalline counterpart and the conventional steel, is responsible for the much higher corrosion resistance in 0.5 M H_2SO_4. SEM investigations of the bulk glassy alloy surface after immersion in the other three solutions, i.e. 0.1 M Na_2SO_4, 0.6 M NaCl and 1 M NaOH, did not reveal morphologies similar to the one after treatment in 0.5 M H_2SO_4. As expected when considering the insignificant weight loss, the surface morphology after immersion in these three solutions remained mostly unchanged with the exception of a limited roughening due to the presence of a thin layer of corrosion products. As an example Fig. 4.5(b) shows a SEM image of the bulk glassy alloy surface after 100 days in 1 M NaOH.

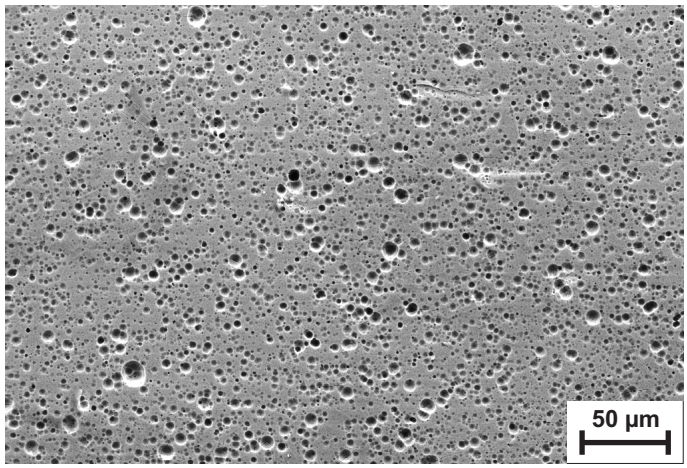

(a)

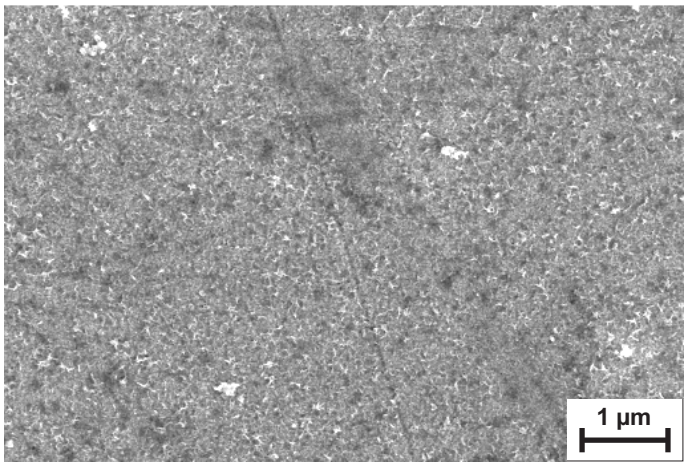

(b)

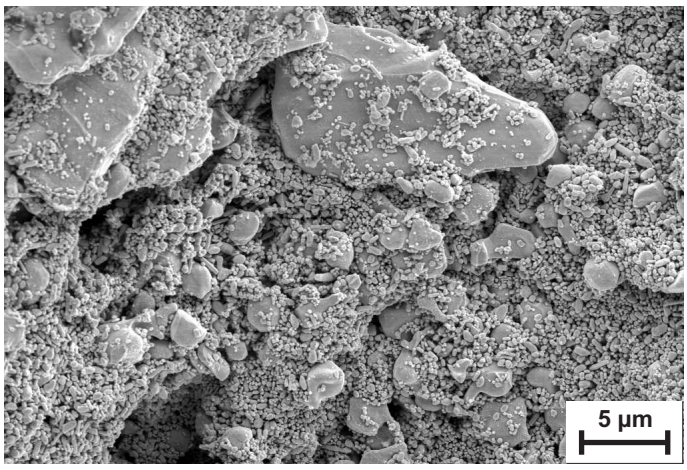

(c)

Figure 4.5: SEM images of the bulk glassy $(Fe_{44.3}Cr_5Co_5Mo_{12.8}Mn_{11.2}C_{15.8}B_{5.9})_{98.5}Y_{1.5}$ alloy surface after 100 days in (a) 0.5 M H_2SO_4 and (b) 1 M NaOH. (c) Surface of commercial steel X210Cr12 after 20 h in 0.5 M H_2SO_4.

Preferential dissolution of the α-Fe(Cr) matrix in the conventional steel, similar to that occurring in 0.5 M H_2SO_4 (though not as strong), was observed after corrosion in the 0.6 M NaCl and 0.1 M Na_2SO_4 solutions. However, in 1 M NaOH, no selective dissolution was indicated by the SEM studies as may be expected when considering the insignificant weight loss. It can be concluded that, with increasing pH value, galvanic coupling becomes decreasingly significant in the corrosion behaviour of the conventional steel.

Summary Weight loss measurements coupled with SEM investigations have been performed for the bulk glassy $(Fe_{44.3}Cr_5Co_5Mo_{12.8}Mn_{11.2}C_{15.8}B_{5.9})_{98.5}Y_{1.5}$ alloy and commercial steel X210Cr12 in 0.5 M H_2SO_4, 0.1 M Na_2SO_4, 0.6 M NaCl and 1 M NaOH solutions. After 100 days, the bulk glassy alloy exhibits a significant weight loss indicating a high corrosion rate only in the acid solution. On the contrary, the conventional steel sample used as reference demonstrated a much higher weight loss in all test solutions, except in 1 M NaOH. This large difference in corrosion stability is explained by the microstructure. While the bulk glassy alloy is single-phase, the conventional steel is multi-phase enabling by this galvanic coupling between the constituent phases resulting in increased corrosion rates. Attack of the bulk glassy alloy in 0.5 M H_2SO_4 causes the formation of micron-sized round pits uniformly distributed on the surface. This aspect will be presented in more detail in section 4.5.

4.3 Effect of pH value on anodic polarization behaviour

4.3.1 Anodic polarization measurements

In order to characterize the free corrosion and the anodic passivation behaviour of the bulk glassy $(Fe_{44.3}Cr_5Co_5Mo_{12.8}Mn_{11.2}C_{15.8}B_{5.9})_{98.5}Y_{1.5}$ alloy in halide free aqueous solutions with pH values in the interval 0.3-14, potentiodynamic anodic polarization measurements were conducted. Typical curves recorded in electrolytes with selected pH values are shown in Fig. 4.6. From these results, corrosion potentials, E_{corr}, and current densities, i_{corr}, were determined and plotted against the pH value of the electrolyte (Fig. 4.7). The corrosion current densities were determined by graphical extrapolation in the potential range close to the current density minimum as explained in section 3.3. The two dashed lines in Fig. 4.7 correspond to the equilibrium conditions of the oxygen and hydrogen reduction reactions for partial pressures of $5 \cdot 10^{-6}$ and 1 atm, respectively. As it can be seen, the corrosion potential, E_{corr}, of this alloy is in all electrolytes nobler than the equilibrium potential of the hydrogen reduction reaction and, in general, it decreases with increasing pH value. Consequently, at free corrosion conditions, depolarization is not achieved by reduction of hydrogen ions. The only possible

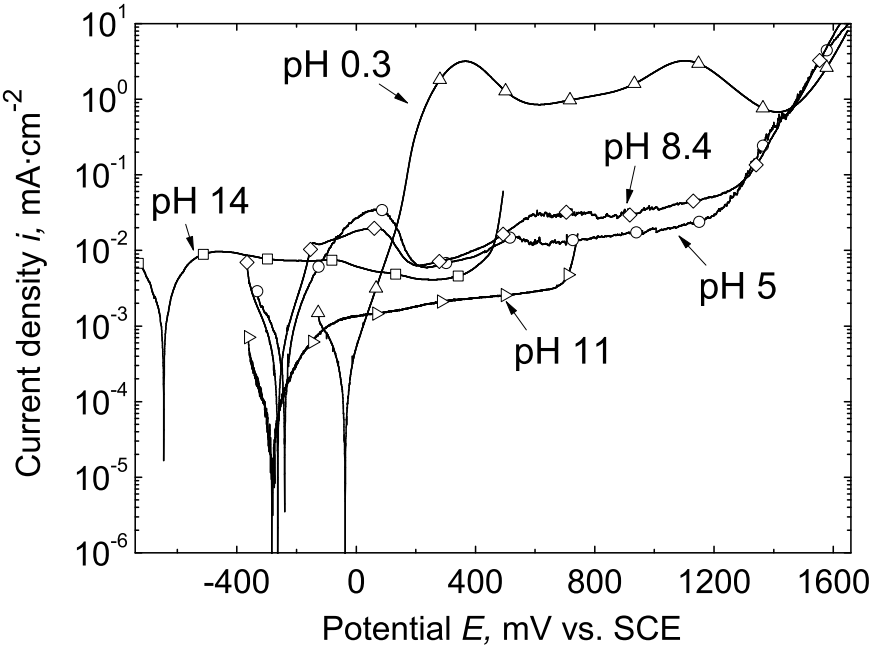

Figure 4.6: Anodic polarization curves of the bulk glassy $(Fe_{44.3}Cr_5Co_5Mo_{12.8}Mn_{11.2}C_{15.8}B_{5.9})_{98.5}Y_{1.5}$ alloy recorded in 0.5 M H_2SO_4 (pH 0.3), 0.1 M Na_2SO_4 (pH 5 and 8.4), 0.001 M NaOH (pH 11), and 1 M NaOH (pH 14).

depolarization reaction in the electrolytes used for testing is the reduction of dissolved oxygen. The corrosion current densities are low, i.e. below $3\,\mu A \cdot cm^{-2}$ at any pH value in the interval 0.3–14. A comparison between this alloy and the conventional steel X210Cr12 regarding corrosion current density values is given later in this section. Between pH 5 and 11, the corrosion potential does not follow the expected trend of decreasing with increasing pH value. Similarly, the corrosion current density does not follow the expected trend of increasing with increasing pH value. Instead, in this pH value interval the corrosion potential is nearly constant and the corrosion current density is decreasing, e.g. at pH 11 it is lower by one order of magnitude than at pH 0.3, 5 or 8.4. This is attributed to the formation of passive films already under open circuit conditions, i.e. during exposure prior to the polarization tests.

Anodic polarization tests were performed in five different solutions with pH values of 0.3, 5, 8.4, 11 and 14. The potentiodynamic curves of the bulk glassy alloy $(Fe_{44.3}Cr_5Co_5Mo_{12.8}Mn_{11.2}C_{15.8}B_{5.9})_{98.5}Y_{1.5}$ recorded at each pH value are shown in Fig. 4.6. Upon anodic polarization at pH 0.3 the alloy generally exhibits high active dissolution rates of 1–3 $mA \cdot cm^{-2}$ which indicate that this alloy is characterized by a very poor passivation ability in very acidic solutions. With increasing pH value of the electrolyte the overall anodic current density level decreases by two orders of magnitude at near neutral pH values (pH 5 and 8.4), i.e. to $\sim 20\,\mu A \cdot cm^{-2}$, and by another one at pH 11, i.e. to $\sim 2\,\mu A \cdot cm^{-2}$, indicating that the passivation ability is remarkably improved with increasing pH value. At pH 11, the alloy passivates spontaneously. The corrosion potential, E_{corr}, establishes during pre-exposure un-

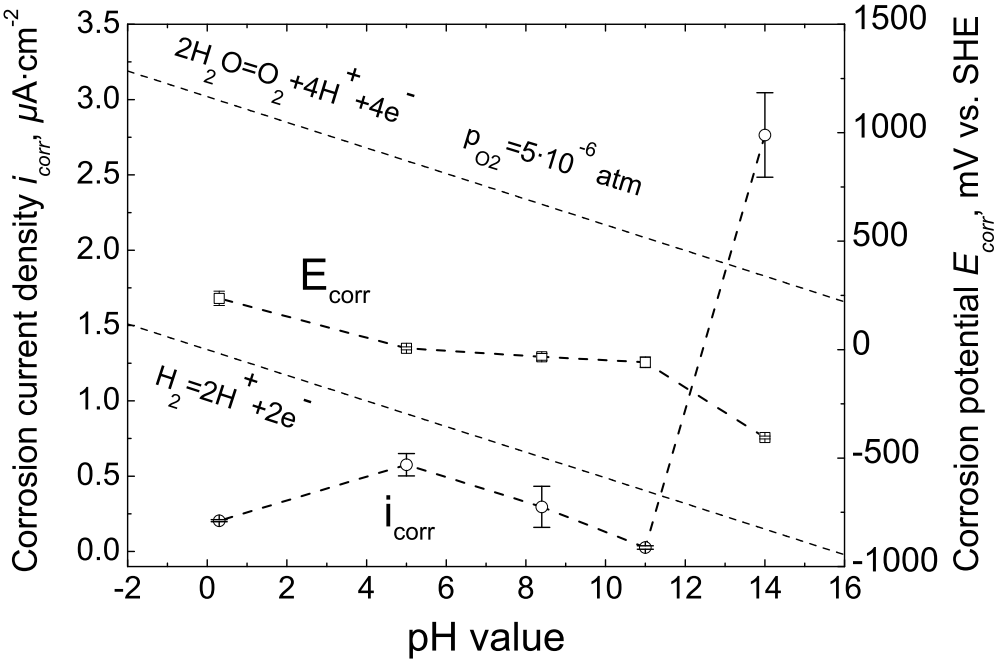

Figure 4.7: Corrosion current density, i_{corr}, and corrosion potential, E_{corr}, of the bulk glassy $(Fe_{44.3}Cr_5Co_5Mo_{12.8}Mn_{11.2}C_{15.8}B_{5.9})_{98.5}Y_{1.5}$ alloy in dependence of the pH value. Dashed lines: equilibrium potentials of oxygen and hydrogen reduction reactions at the experimental conditions.

der OCP conditions at potentials nobler than the passivation potential, E_{pass}. Consequently, the polarization curve does not show an active-passive transition. It is passive already at the beginning of the polarization test and it remains passive for at least 920 mV. The current density is not constant in the passive domain. Its logarithm increases linearly with potential (with a slope of $5.4{\cdot}10^{-4}$ A·V^{-1}). In very basic electrolytes, i.e. at pH 14, although the alloy exhibits a passive behaviour similar as at pH 11, the mean passive current density is higher, i.e. $\sim 7\,\mu A \cdot cm^{-2}$ (at $E = -150$ mV), which reveals that the passive film is less protective. Two domains can be distinguished in the anodic polarization curve: one at lower polarization, from E_{corr} up to –70 mV vs. SCE, where the passive current decreases slowly with potential and another one at more anodic potentials than –70 mV, where the current density decreases faster with increasing potential.

For the pH value interval 0.3-8.4, at low anodic polarization there is an active dissolution domain followed by an active-passive transition (peaks at 360 mV for pH 0.3 and at 60 mV for pH 5 and 8.4, respectively) which is marked by a decrease in current density of almost one order of magnitude. At higher anodic potentials, at pH 0.3 there is a second oxidation peak at 1110 mV. At pH 5 and 8.4, instead of this second oxidation peak there is a plateau with small fluctuations which begins at 560 mV after a domain in which the current density increases slowly. However, the mean 'passive' current density measured in 0.5 M H_2SO_4 (pH 0.3) is quite high. This is mainly explained by the much higher thermodynamic stability of

the ionic state as compared to the oxide state for some of the alloy constituent elements, e.g. Fe, Cr, Co, Mn, Y [96] (see section 2.4). Because these elements tend to be more stable as ionic species, they do most probably not form oxides on the alloy sample surface to protect it from active dissolution. The decay in current density after the first peak indicates the formation of a 'passive' film which is not very protective as the recorded current density is still quite high, i.e. $0.8\,\mathrm{mA \cdot cm^{-2}}$. The decay in current density after the second oxidation peak can be attributed to the formation of MnO_2 (see the reaction in Table 2.3). According to the Pourbaix diagram for pure Mn, the equilibrium potential for the 10^{-6} M Mn^{2+}/MnO_2 transition is 1320 mV vs. SHE which is very close to the potential corresponding to the peak maximum (1350 mV vs. SHE). With increasing pH value (up to ~ 11), the stability domains of the oxide species of the alloy constituents become wider (see Pourbaix diagrams of constituent elements in section 2.4 and Ref. [96]) gaining more stability with respect to the ionic state. Therefore, the dissolution rates are lower with increasing pH value of the electrolyte up to pH ~ 11. However, with a further increasing pH value towards very basic conditions, the potential domains in which the oxide species are stable shrink and as expected, a higher passive current level is registered in the solution with pH 14 compared to the one with pH 11.

4.3.2 Influence of sulphate concentration

During the pitting studies which will be presented later (section 4.4) it was observed that sulphate ions can act very deteriorating on passivity — in some cases even more than chloride ions. Therefore, it was decided to dedicate special attention to systematically investigate the influence of sulphate ions on the anodic passivation ability. In order to do this for the bulk glassy $(Fe_{44.3}Cr_5Co_5Mo_{12.8}Mn_{11.2}C_{15.8}B_{5.9})_{98.5}Y_{1.5}$ alloy, a series of potentiodynamic polarization measurements was performed in solutions with various concentrations of Na_2SO_4, and additionally in 0.5 M phthalate buffer, all with the same pH value of 5. As it can be seen in Fig. 4.8, the nature and the concentration of the anions in the electrolyte have a significant influence on the anodic polarization behaviour of this alloy.

In 0.5 M phthalate buffer, the alloy has the least noble corrosion potential and the anodic potential corresponding to the critical passivation current is also less noble than the corresponding ones recorded in the sulphate containing solutions. The kind of anions of the electrolyte does not drastically influence the active dissolution regime and the critical passivation current density (compare anodic polarization curves in 0.5 M phthalate buffer and in 0.5 M Na_2SO_4, respectively). But the concentration of the sulphate ions in the electrolyte has a dramatic influence on the active dissolution process, e.g. at $E{=}{-}50\,\mathrm{mV}$ the current density in 10^{-5} M H_2SO_4 is $4.2\,\mu\mathrm{A \cdot cm^{-2}}$ while in 0.1 M Na_2SO_4 it is increased by one order

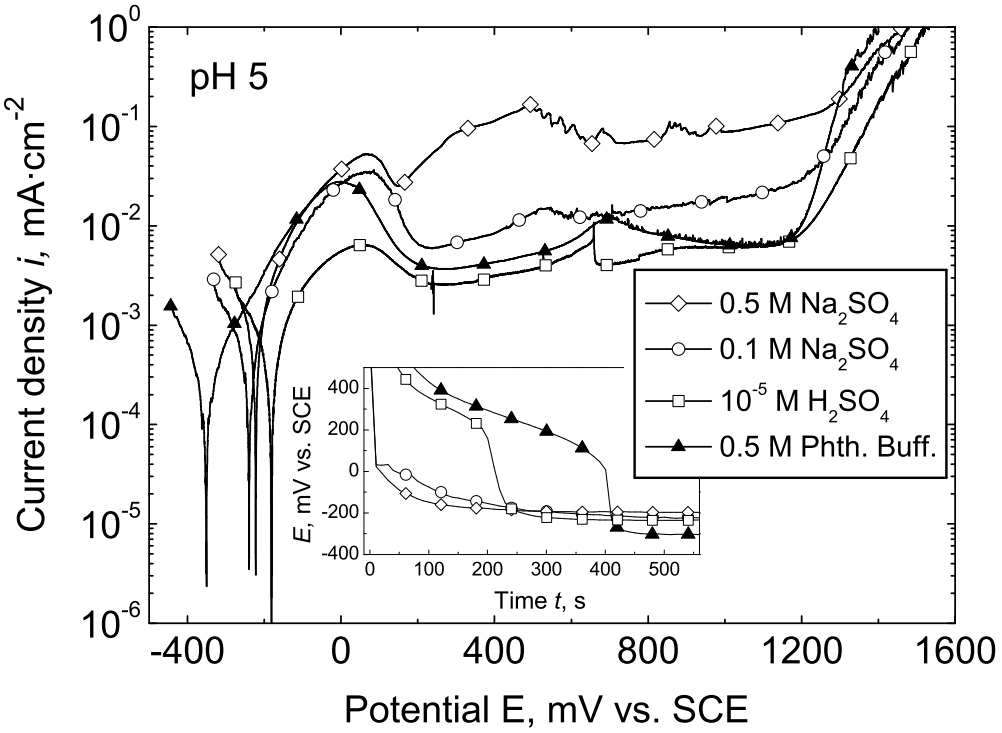

Figure 4.8: Anodic polarization curves of the bulk glassy $(Fe_{44.3}Cr_5Co_5Mo_{12.8}Mn_{11.2}C_{15.8}B_{5.9})_{98.5}Y_{1.5}$ alloy recorded in various solutions with pH 5. Inset: free electrode potential versus time curves after the polarization tests.

of magnitude to $20\,\mu A \cdot cm^{-2}$. The active-passive transition does not occur suddenly at a certain potential as shown in Fig. 3.1, but gradually in a potential interval. There is a strong influence of the sulphate ion concentration on the passive current density of this alloy. On average, a one order of magnitude higher passive current density is observed for an increase of the sulphate ion concentration from 0.1 to 0.5 M. In order to investigate the influence of the sulphate ion concentration on the stability of the anodically formed passive films, the self-regulating electrode potential was measured after the potentiodynamic tests. In the inset of Fig. 4.8 selected parts of the free electrode potential vs. time curves determined immediately after the linear polarization tests are shown. In the electrolytes with high sulphate ion concentration, after the polarization is stopped, the self-regulating electrode potential under open circuit conditions drops rapidly to a potential close to the open circuit potential (the one measured before the linear polarization test), while for the sulphate free and low concentrated electrolytes the free electrode potential firstly tends to reach a constant value of 200 mV corresponding to an anodic potential close to the equilibrium potential of the passive film/electrolyte system and then, as this film is dissolved, rapidly decays to the initial OCP value. It results from the above described observations that the sulphate anions deteriorate

the protective effect and the stability of the passive films on this alloy in solutions with a pH value of 5.

4.3.3 Auger electron spectroscopy investigations

The analysis of the composition of the thin passive films formed on the bulk glassy alloy surface was performed by Auger electron spectroscopy (AES). This is very challenging due to the expected superposition of the Auger peaks of the numerous constituent elements. Sputter depth profiles were recorded after exposure of the cross-sectional areas of the rod samples to air, to 0.1 M Na_2SO_4 (pH 5) under free corrosion conditions and after anodic potentiostatic polarization in 0.1 M Na_2SO_4 (pH 5) at 280 mV and to 0.001 M NaOH (pH 11) under polarization at 400 mV. Typical profiles are shown in Fig. 4.9. In order to prevent a subsequent modification of the passive films formed by potentiostatic polarization, the samples were removed from the electrolyte and cleaned with ethanol immediately after the polarization was stopped.

In the Auger electron spectra of all surfaces (not shown here), oxide species of only Cr and Fe were detected. However, by sputtering oxidized species can be reduced. Therefore the possibility that other elements are present in the oxidized state in the passive film should not be excluded. For C, in the Auger electron spectra two peaks corresponding to different bonding states were identified: one which is similar to that measured in carbides, and another one similar to that measured in graphite (the usual peak shape of the surface contamination C species). The concentration of C with graphite-like bonding is very small, i.e. 0.5 at.%, at the substrate. Therefore, the carbide-like peak shape is assumed to be characteristic for C in the alloy. B could not be clearly identified in the AES spectra due to partial superposition of its Auger transition (K-VV) with those of other elements like Mo (M_{45}-NN) and S (L-VV). Y could not be detected at all neither in the bulk of the alloy nor in the covering passive films.

For all samples, a slight enrichment in C is observed in the bulk alloy close to the surface layer/alloy interface. It is also observed that the passive layers are strongly depleted in C as obvious from Fig. 4.9. This suggests that either C is not easily dissolved at the potentials at which the polarization tests were performed or that the transport of C through the passive layer, from the inner alloy/film to the outer film/electrolyte interface, is slower than the transport of other constituents.

On the surface of a sample that is exposed to air for one week, a thin layer of Fe and Cr oxides with an estimated thickness of 2-3 nm is formed (see Fig. 4.9(a)). This layer has a non-uniform composition, i.e. it consists mainly of Fe oxide in the outer region and of a mixture of Fe and Cr oxides in almost equal proportions in the inner region close to the alloy. All the other elements are drastically depleted in the surface layer. Polished samples exposed

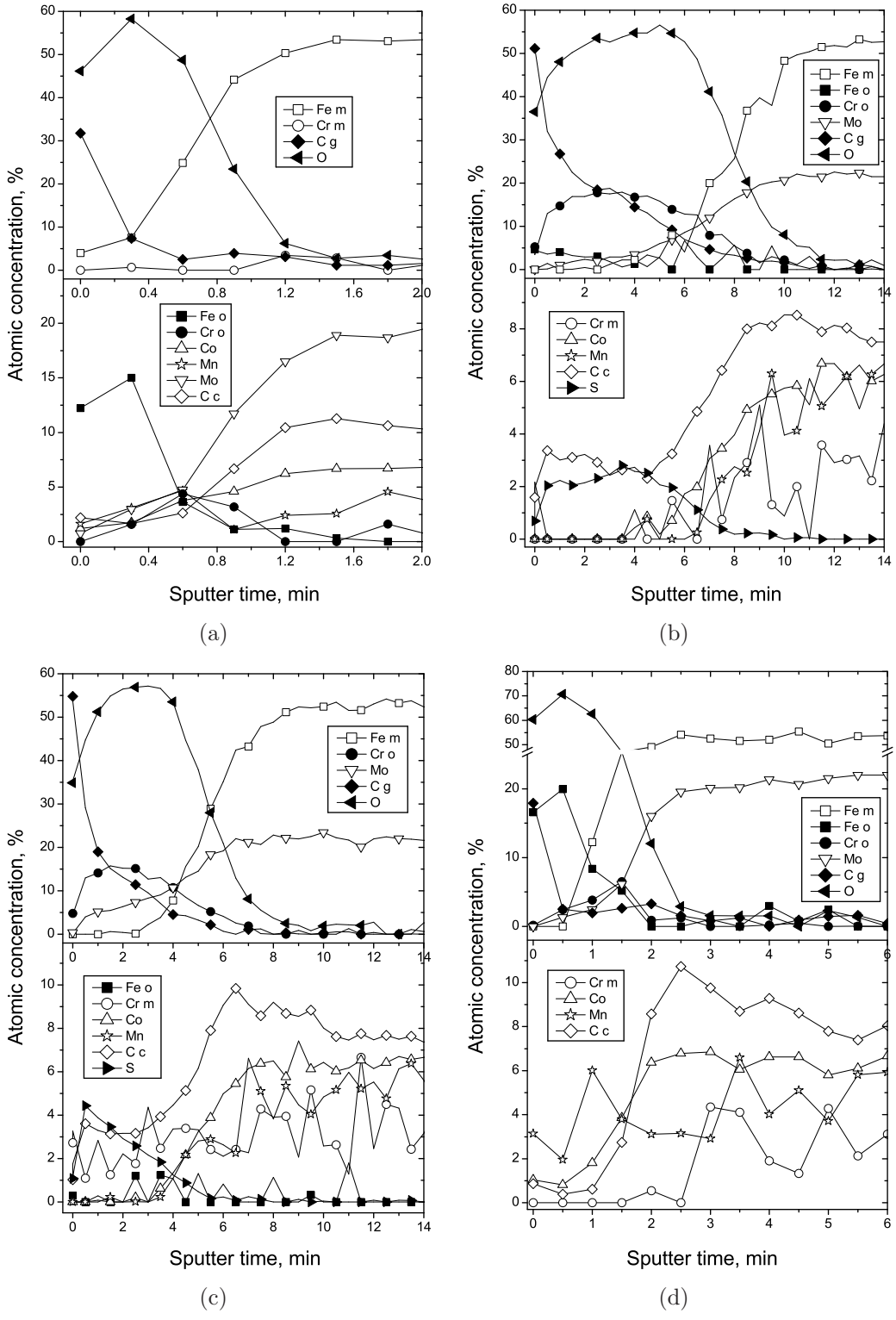

Figure 4.9: Concentration depth profiles from AES investigations of the surface of bulk glassy $(Fe_{44.3}Cr_5Co_5Mo_{12.8}Mn_{11.2}C_{15.8}B_{5.9})_{98.5}Y_{1.5}$ samples after various treatments: a) one week in laboratory air, b) 19 h immersion in 0.1 M Na_2SO_4 with pH 5, c) 19 h potentiostatic polarization at 280 mV in 0.1 M Na_2SO_4 with pH 5, and d) 19 h potentiostatic polarization at 400 mV in 0.001 M NaOH. Main species are represented in the upper plots and minor species are represented in the lower plots.

to laboratory atmosphere for 18 months are still shiny. This shows that the passive film formed in air is protective enough to insure an excellent resistance to atmospheric corrosion (at 40% humidity level).
A much thicker oxide layer (estimated thickness $\sim$ 22 nm) is formed on the bulk glassy $(Fe_{44.3}Cr_5Co_5Mo_{12.8}Mn_{11.2}C_{15.8}B_{5.9})_{98.5}Y_{1.5}$ alloy after exposure to a solution of 0.1 M Na_2SO_4 with pH 5 (see Fig. 4.9(b)) for 19 h. This layer is mainly composed of Cr oxide and contains small amounts of oxidized Fe, metallic Mo, and C. Neither Co nor Mn is detected in the oxide layer. S is also present in the passive layer in a small concentration, which is relatively constant over the thickness of the surface layer.
The surface layer formed by potentiostatic polarization at 280 mV for 19 h in the same solution (0.1 M Na_2SO_4 with pH 5) is thinner (estimated thickness $\sim$ 15 nm). It is also mainly composed of Cr oxide (see Fig. 4.9(c)). This film comprises small amounts of C and metallic Mo. The Mo concentration is not uniform over the thickness of the oxide layer, but increases with distance from the outer surface. S is again present in the oxide layer in small concentrations.
The AES investigations reveal that the layers formed in sulphate electrolytes contain S, most probably as metal sulphates since the sulphate SO_4^{2-} anions which are already in the electrolyte are very stable. Another indication that the surface layers formed in sulphate electrolytes contain metal sulphates is that the passive current density increases with sulphate concentration (see Fig. 4.8). Most probably the layer consists mainly of Cr oxide/oxyhydroxide and a variable fraction of various sulphate compounds depending on the sulphate anion activity in the electrolyte. The ratio of the oxide-to-sulphate concentrations in the layer may decrease with increasing activity of sulphate anions, rendering the surface film less resistant to the transport of species to and from the electrolyte/film interface.
Potentiostatic anodic polarization in 0.001 M NaOH (pH 11) at 400 mV for 19 h results in the formation of a film with similar composition as the one formed in air (see Fig. 4.9(d)), though it is two times thicker (estimated thickness $\sim$ 5 nm). The outer layer additionally (to the one formed in air) contains a small amount of metallic Cr and Mn. Mn was not depleted nor enriched in the oxide film, it has the same concentration as in the bulk of the alloy. Of all the metal components of this alloy, only Mo dissolves actively at this pH value [96]. All the other metals form stable oxides or hydroxides which can contribute to passivity. As obvious from the AES results, Mo is indeed strongly depleted in the surface layer, but unexpectedly also Co. It is known that pure Co forms in basic solutions upon increasing anodic polarization compounds like $Co(OH)_2$, Co_3O_4 and CoOOH [100].

The poor passivation ability of the bulk glassy alloy in acidic solutions is explained by the insufficient concentration of passivating constituents. Mainly, the concentration of Cr is considered to be insufficient for the formation of a complete Cr oxide rich layer. The

Cr concentration of this alloy (4.93 at.%) is much lower than the minimum value which is regarded to be necessary to form a complete Cr-oxyhydroxide film on conventional Fe-Cr alloys, i.e. (13 at.%). It is also lower than the Cr content of earlier Fe-based amorphous alloys notable for their excellent corrosion resistance, e.g. Fe-10Cr-13P-7C (concentrations in at.%) [14] (see section 2.3). Compared to the above mentioned alloys with optimized composition, the alloy under investigation contains also a relatively high concentration of elements that are electrochemically very active in acidic solutions, namely Mn and Co. Their oxides are only stable at high anodic potentials (see section 2.4). For example, at pH 0.3 the equilibrium potential of the 10^{-6} M Mn^{2+}/MnO_2 couple is 1320 mV (vs. SHE) and that of 10^{-6} M Co^{2+}/CoO_2 is 1750 mV (vs. SHE) (for reactions see Table 2.3). Therefore, at lower potentials (which are of interest for usual corrosion conditions), they can not participate effectively in the passivation process based on oxide formation. It is concluded, with respect to these thermodynamic considerations, that in acidic solutions Mn and Co can have a detrimental effect on the passivation of the glassy alloy at pH 0.3. Mn was already proven to show this effect in the case of stainless steels [104, 105]. Mo is known to have a beneficial effect on the pitting resistance of stainless steels and also to ease their passivation by altering the active-passive transition [78]. However, when its concentration, or more precisely, the ratio of its concentration to that of Cr is high, it yields a poor protective effect of the growing passive films. It was clearly shown for the glassy FeCrMoCB system that excessive Mo to Cr concentration ratios cause a dramatic increase of the anodic passive current density [82]. In consequence, also for this alloy, the Mo content is regarded to be detrimental for passivation. Furthermore, as suggested by Hashimoto [17], C is expected to dissolve rapidly as carbonates. According to thermodynamic considerations, in acidic solutions, Y is also expected to easily dissolve (as Y^{3+} ions) [96].

At higher pH values, as shown by the potentiodynamic polarization measurements (Fig. 4.6), the passivation ability of the glassy alloy is higher. The main constituents of the passive films are Fe and Cr oxides. Cr is strongly enriched in the passive film. For example, it reaches more than 50 at.% of the cationic species at pH 5, although its fraction in the composition of the bulk alloy is only 4.93 at.%. Another interesting observation is that C is enriched underneath the passive film. To the author's knowledge, this enrichment of C was not noted in previous studies on other Fe-based amorphous alloys. But there are studies that report an enrichment of another metalloid, P, underneath the passive layer [91, 92]. This sub-surface enrichment was not observed for B or Si. As explained in section 2.3, the metalloids have a marked effect on the corrosion resistance and passivation ability of Fe-based glasses. The corrosion resistance was found to increase with the order: B and Si $<$ C $<$ P [92]. It was argued that the beneficial effect of P might be attributed to the enrichment of P underneath the film reducing the ionic conductivity of the interface. Since a similar enrichment in C is observed for the bulk glassy $(Fe_{44.3}Cr_5Co_5Mo_{12.8}Mn_{11.2}C_{15.8}B_{5.9})_{98.5}Y_{1.5}$ alloy, it may be

concluded that C has a similar effect as P.
Y is known to have some beneficial effects, for instance, to improve the stability of passive films for the $Fe_{50-x}Cr_{15}Mo_{14}C_{15}B_6Y_x$ bulk glass [85]. However, as the AES results indicate, Y species are not present in the passive films of the bulk glassy $(Fe_{44.3}Cr_5Co_5Mo_{12.8}Mn_{11.2}C_{15.8}B_{5.9})_{98.5}Y_{1.5}$ alloy. Still, this observation might be an artefact, as any Y present could be removed during the sputtering process. Below the passive film, in the bulk of the sample, the AES results reveal that there is no Y, but they should show the nominal composition of 1.5 at.%. This sustains the idea that Y might be originally present in the passive film. To clarify whether this is a sputtering effect, AES should be performed on the bare surface of the alloy (sample broken inside the vacuum chamber of the spectrometer). The same discussion is applicable to B. In conclusion, a discussion regarding the influence of the minor constituents B and Y on corrosion-related modifications of the surface-near regions would be irrelevant here due to the low reliability of the analysis data for these two species.

4.3.4 Comparison with the crystalline counterpart and the conventional steel

In order to compare the anodic polarization behaviour of the bulk glassy alloy with that of its crystalline counterpart and that of the conventional steel, a series of anodic polarization curves have been recorded for all three alloys in electrolytes with pH values in the range 0.3–14. Exemplary potentiodynamic curves measured in 0.5 M H_2SO_4 (pH 0.3) are shown in Fig. 4.10. In agreement with the results of the weight loss tests it is obvious that in this acid electrolyte the glassy alloy exhibits a much lower corrosion current rate than the conventional steel sample. As in the case of the immersion tests, also in the case of the linear polarization tests galvanic coupling between the $(Fe,Cr)_7C_3$ particles and the αFe(Cr) matrix is responsible for the high corrosion activity of the steel. As mentioned in section 4.2, due to its multiphase nature also the crystalline counterpart, similar to the conventional steel, suffers from galvanic coupling between the main phase ($M_{23}(B,C)_6$) and the interdendritic phase(s). This is expected to be the reason for the higher corrosion current density of both crystalline alloys compared to that of the single-phase glassy alloy.
The anodic behaviour of the three alloys in this acidic solution is quite different. Opposite to the low corrosion current, upon anodic polarization, the glassy alloy exhibits high dissolution rates proving a very low ability to passivate in this electrolyte (the origin of this behaviour was discussed in the sections 4.3.1 and 4.3.3). Similarly, the crystalline counterpart exhibits low passivation ability. Only the conventional steel sample shows an appreciable tendency to passivate, i.e. a clear active-passive transition is visible at $E_{pass} = 280\,\mathrm{mV}$ vs. SCE.
Potentiodynamic measurements for the three alloys were also conducted in other electrolytes

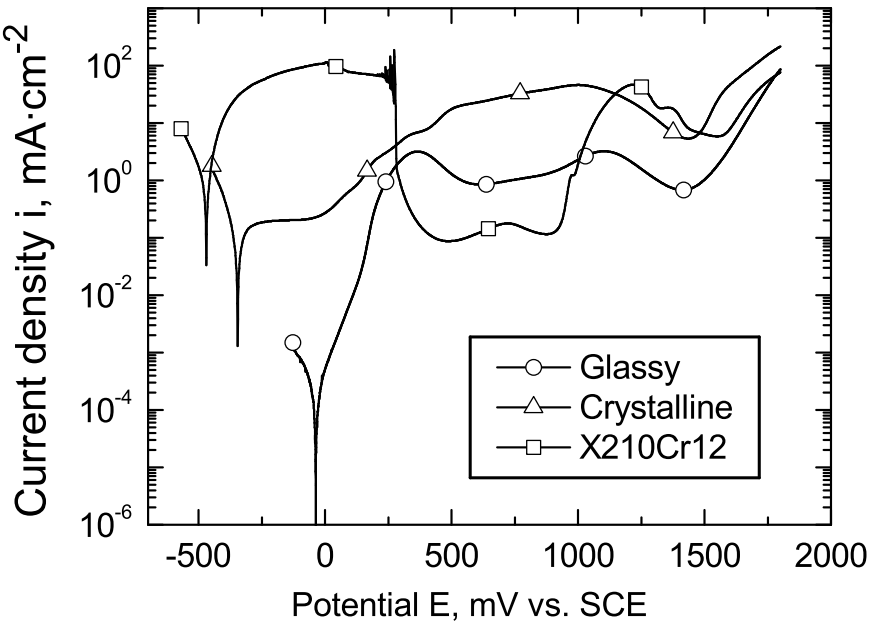

Figure 4.10: Potentiodynamic anodic polarization curves of the bulk glassy alloy $(Fe_{44.3}Cr_5Co_5Mo_{12.8}Mn_{11.2}C_{15.8}B_{5.9})_{98.5}Y_{1.5}$, of its crystalline counterpart and of commercial steel X210Cr12 recorded in 0.5 M H_2SO_4 (pH 0.3).

with various pH values: 5, 8.4, 11 and 14. Characteristic quantitative corrosion parameters determined from these curves are plotted versus the pH value in Fig. 4.11. Their determination is explained in section 3.3. As obvious from Fig. 4.11(b), both the glassy alloy and its crystalline counterpart, have significantly nobler corrosion potentials than the steel in acidic solutions and behave slightly more noble in near neutral acidic solutions. This could be explained by the formation of Mo-oxide(s)-rich films on the multicomponent alloy surfaces proceeding already during the 1 h period of exposure in the electrolyte prior to the beginning of the potentiodynamic measurements. It was previously noted that, in acidic conditions, Mo determines the ennoblement of Fe [120] and also of glassy Fe-Cr based alloys [81] by the formation of a Mo oxide film. In neutral and slightly basic solutions, all constitutive metallic elements except Mo form stable oxides or hydroxides [96] (see section 2.4). Only at pH 11 the conventional steel exhibits a more noble corrosion potential, E_{corr}, than that of the crystalline counterpart, and at pH 14 the potential value is higher than that of both multicomponent alloys. This is explained by the chemical composition difference: additionally to Fe, Cr and C (the main elements of the conventional steel) the multicomponent alloys contain elements like Mo, Mn and Co in significant concentrations. In very basic solutions, those components can be dissolved as complex ions and only at higher potentials Mn and Co form oxide or hydroxide films [96] (see section 2.4).

As seen in Figs. 4.10 and 4.11(a), at pH 0.3 the corrosion current density values of the three alloys are very different. As already discussed, this is a direct effect of their phase composi-

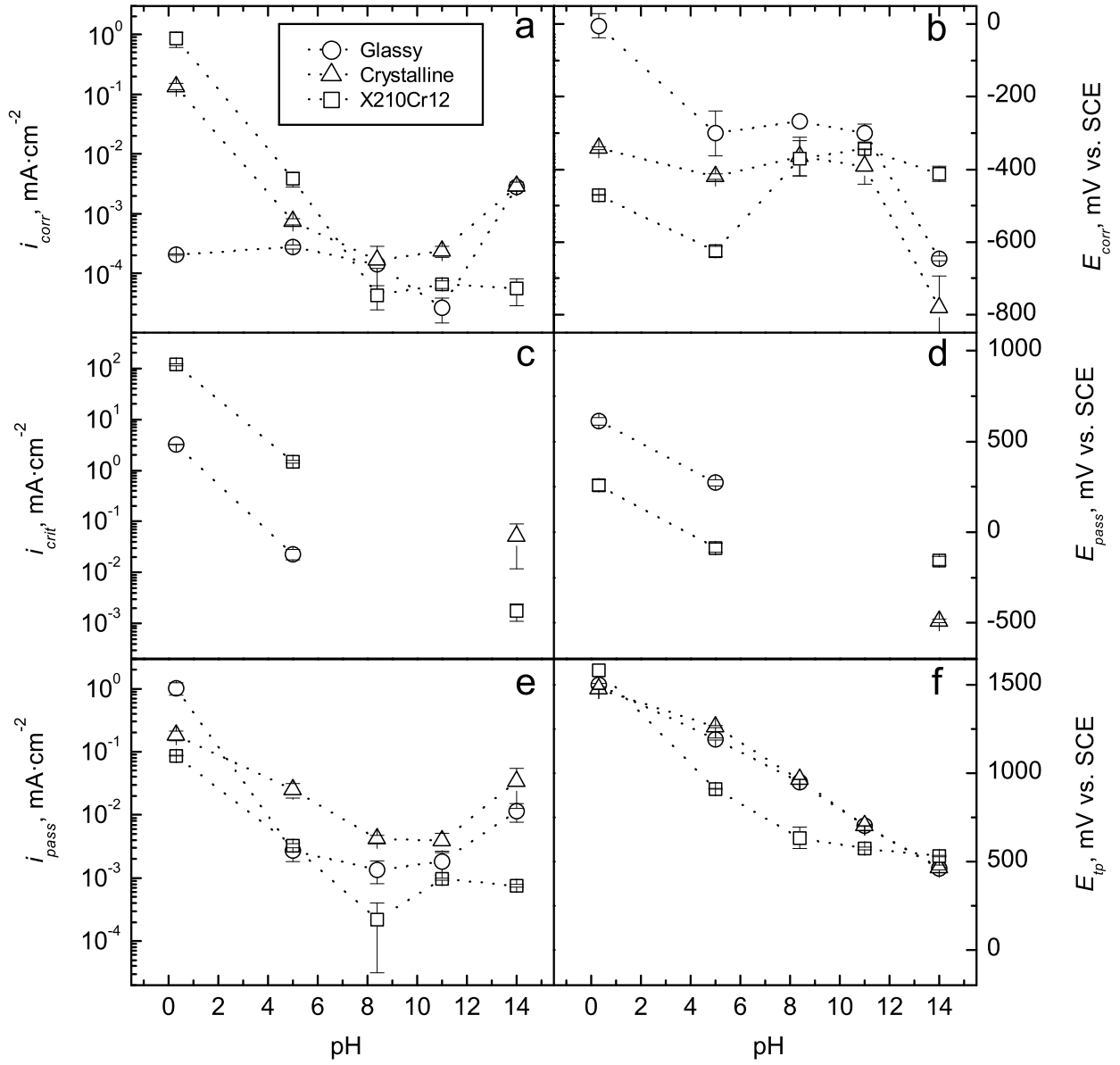

Figure 4.11: Characteristic corrosion parameters of the bulk glassy alloy $(Fe_{44.3}Cr_5Co_5Mo_{12.8}Mn_{11.2}C_{15.8}B_{5.9})_{98.5}Y_{1.5}$, of its crystalline counterpart and of commercial steel X210Cr12 in dependence of pH value: (a) corrosion current density i_{corr}, (b) corrosion potential E_{corr}, (c) critical current density i_{crit}, (d) passivation potential E_{pass}, (e) passive current density i_{pass}, and (f) transpassivation potential E_{tp}. Values determined from potentiodynamic measurements.

tion. However, at higher pH values, in near neutral solutions, these differences are smaller. As described in section 4.2, with increasing pH value the galvanic coupling between the αFe(Cr) matrix and the $(Fe,Cr)_7C_3$ particles plays a less and less important role and, as it will be seen later in this section, the overall passivation (of both phases) dominates its behaviour. A similar behaviour is to be expected from the crystalline counterpart. In very basic solutions, at pH 14, the difference in corrosion current densities are again as high as in the acidic solu-

tions. But in these basic solutions the conventional steel is very corrosion resistant, while the multicomponent alloys have higher corrosion current densities. The corrosion current densities of the multicomponent alloys are very similar, indicating that the phase composition has an insignificant influence on this parameter in this electrolyte. Altogether, it results that in very basic solutions the phase composition plays an insignificant role, while the elemental composition dominates the overall behaviour. As explained for the E_{corr} dependency on pH value, Mo, Mn and Co are also assumed to be responsible for the higher corrosion current densities of the multicomponent alloys as compared to those of the conventional steel.
Figures 4.11(c) and (d) show the pH value dependencies of the critical current density and of the passivation potential, respectively, corresponding to the three studied alloys. The missing points in these curves correspond to those cases of spontaneous passivation which did not allow the aforementioned parameters to be determined. Compared to the conventional steel, the multicomponent alloys exhibit, in acid solutions, lower critical current densities and nobler passivation potentials, while in base electrolytes they have higher critical current densities and less noble passivation potentials. As in the case of corrosion current densities and potentials, a Mo oxide film would explain the reduced critical current in acid solutions. The free dissolution of Mo, Mn and Co at low potentials (see section 2.4) would explain the higher values of critical current density and of passivation potential for the multicomponent alloys compared to the conventional steel.
Furthermore, the passive current density values of the three alloys were evaluated comparatively. It is obvious from Fig. 4.11(e) that the passive films formed on the X210Cr12 steel are the most protective (except at pH 5, where its passive current density is very close to that of the glassy alloy). This is explained by the alloy composition. It was shown that the carbide particles $(Fe,Cr)_7C_3$ in the conventional steel consist of approximately 35 at.% Cr. Additionally, the C in these particles further contributes to a lowering of the passive current [121]. In contrast, the αFe(Cr) matrix contains only 6 at.% Cr or less and an insignificant concentration of C (its solubility in this phase is very limited [119]). In consequence, it is expected that the matrix forms less protective passive films than the carbide phase and so the overall passive current density (the measured one) is determined by the passive film on the matrix. The single-phase glassy alloy has a relatively similar content of Cr, i.e. 5 at.% compared to the matrix phase of the conventional steel, i.e. 6 at.%. However, as mentioned earlier, the higher content of C in this glassy alloy, compared to that in the matrix phase of the conventional steel, is expected to result in lower i_{pass} values. Nevertheless, the effect of the other reactive alloying elements of the glass dwarfs the effect of Cr and C. As AES investigations on the glassy alloy revealed [55], some of the alloying elements can have a detrimental effect on the passivity of this alloy (see section 4.3.3). For example, Mo does not participate in the composition of the anodic passive films. As well, Co is not present in the passive films formed on this glassy alloy. Furthermore, Mn was seen to participate only in

those passive films which are formed in basic electrolytes [81].
As derived from Fig. 4.11(e), the passive films on the glassy alloy are more protective than those on the crystalline counterpart. However, it cannot be clearly concluded that this is a particular intrinsic effect of the amorphous nature of the single-phase glassy alloy. In contrast, the crystalline counterpart alloy, like the conventional steel, is of multiphase nature. Therefore, the crystalline counterpart is covered with a passive film that is laterally non-uniform. Thus, it is believed that the segregation of various elements in the constitutive phases leads to a passive film that is locally less protective than that on the glassy alloy. Unfortunately, as mentioned earlier, due to the low dimension of the interdendritic phase(s), the measurement of its elemental composition provided insignificant differences compared to the overall composition of the alloy.
As it can be seen in Fig. 4.11(f), the difference in phase composition between the glassy alloy and its crystalline counterpart has almost no influence on the transpassivation potential. On the contrary, the X210Cr12 steel has lower transpassivation potentials, except at extreme pH values (0.3 and 14) which indicates that the additional elements of the multicomponent alloys (with respect to the conventional steel) extend the stability domain of the passive film to higher potentials. This could be explained by the fact that in addition to Fe or Cr oxides that can form on the conventional steel, on the multicomponent alloys, Mn and Co oxides (which are stable up to higher potentials) can also form.
In conclusion, as a consequence of its single-phase nature, in acid solutions the glassy alloy exhibits a high free corrosion stability compared to its crystalline counterpart and the conventional steel. However, by anodic polarization, the single-phase glassy alloy (with passivating Cr and Fe contents lower than those of the conventional steel) exhibits lower passivation tendency, but higher compared to its multiphase crystalline counterpart. With increasing pH value, the passivation ability of all three alloys is improved and the galvanic coupling effect becomes weaker. In very basic solutions, the influence of the galvanic coupling is minimal and, instead, the elemental alloy composition dominates the free corrosion and the anodic behaviour.

4.3.5 Summary

The influence of the pH value of an electrolyte on the anodic polarization behaviour and the passivation ability of bulk glassy $(Fe_{44.3}Cr_5Co_5Mo_{12.8}Mn_{11.2}C_{15.8}B_{5.9})_{98.5}Y_{1.5}$ has been investigated. For this, anodic polarization tests and AES investigations of grown surface films have been performed. In a large pH value interval (0.3–14), the bulk glassy alloy shows corrosion potential values nobler than the equilibrium potential of the hydrogen evolution reaction and it yields corrosion current densities below $3\,\mu A \cdot cm^{-2}$. Its passivation ability is poor in acidic solutions. However, with increasing pH value of the electrolyte, the passivation ability

is dramatically improved due to the formation of protective surface layers mainly composed of Fe and Cr compounds, for example, oxides/salts. Sulfate ions present in the solution negatively influence the protective effect of the passive layer most probably by incorporation of sulfate anions in the film which reduces the fraction of the more effective oxides. The poor passivation ability of the glassy alloy in acidic solutions is explained by the alloy composition: mainly the Cr concentration is considered to be insufficient for the formation of a complete Cr-oxide-rich layer and at the same time, the concentration of Mn, which is electrochemically active in very acidic solutions (see section 2.4), is too high. The passivation ability may be improved by further development of the alloy composition in the limits allowed for obtaining a sufficient GFA. Particularly suggested are (i) an increase of the concentration of Cr to a level that enables the formation of complete, very protective surface films, (ii) a decrease of Mo concentration to a value enabling an optimal Mo/Cr ratio (this has to be found out by trial) and (iii) a decrease of the concentration of Mn, which deteriorates the protective effect of a passive film (see section 2.4), to a necessary minimum.
In acid electrolytes the crystalline counterpart and the conventional steel exhibit much higher corrosion rates than the glassy alloy. This is a consequence of galvanic coupling between the $M_{23}(B,C)_6$ dendrites and the η-carbide interdendritic phase, causing the preferential dissolution of the η-carbide in the case of the crystalline alloy, and between the $(Fe,Cr)_7C_3$ particles and the αFe(Cr) matrix causing preferential dissolution of the αFe(Cr) matrix in the case of the conventional steel. However, by anodic polarization, the single-phase bulk amorphous steel exhibits a passivation tendency lower than that of the conventional steel due to its lower content of passivating elements Cr and Fe. But compared to the crystalline counterpart, the glassy alloy has higher tendency to passivate. With increasing pH value, the passivation ability of all three alloys is improved and the galvanic coupling effect aforementioned becomes weaker. In very basic solutions, the influence of the galvanic coupling is minimal, and, instead, the elemental composition dominates the free corrosion and the anodic behaviour.

4.4 Pitting corrosion

In order to study the pitting corrosion behaviour of the bulk glassy alloy $(Fe_{44.3}Cr_5Co_5Mo_{12.8}Mn_{11.2}C_{15.8}B_{5.9})_{98.5}Y_{1.5}$ and to compare it with that of its crystalline counterpart and of the conventional steel, anodic potentiodynamic polarization measurements were performed in neutral aqueous solutions with various NaCl concentrations. Some representative curves are shown in Fig. 4.12. The corrosion current density values of the glassy alloy are similar in all three electrolytes and similar to the one in a chloride-free neutral electrolyte (0.1 M Na_2SO_4 — corresponding polarization curve not shown here), i.e. $0.6\,\mu A \cdot cm^{-2}$. The corrosion potentials of the glassy alloy are not as similar to each other as the corrosion current

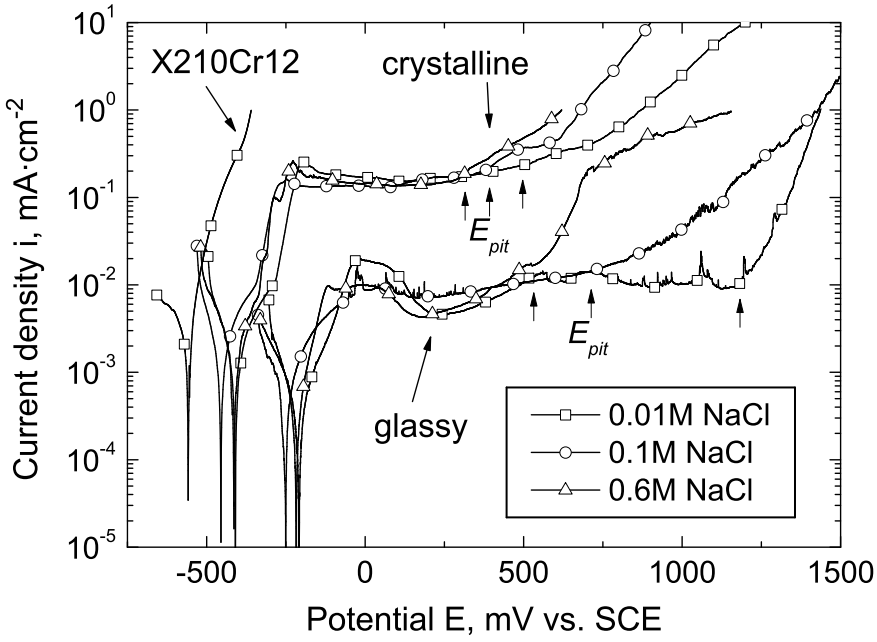

Figure 4.12: Potentiodynamic anodic polarization curves of the bulk glassy $(Fe_{44.3}Cr_5Co_5Mo_{12.8}Mn_{11.2}C_{15.8}B_{5.9})_{98.5}Y_{1.5}$ alloy, of its crystalline counterpart and of the commercial steel X210Cr12 in neutral 0.001, 0.1 and 0.6 M NaCl electrolytes.

density values, but the corrosion potential value in 0.1 M NaCl, i.e. -250 mV vs. SCE, is very close to the value in 0.1 M Na_2SO_4, i.e. -256 mV vs. SCE. It can be concluded therefore, that Cl ions, Cl^-, do not have a significant influence on the dissolution reaction of the glassy alloy at low polarization conditions. The low anodic current densities, e.g. at 300 mV vs. SCE, $\sim 10\,\mu A \cdot cm^{-2}$, indicate that a stable passive layer is initially formed on the bulk glassy alloy surface at all three chloride concentrations. Nevertheless, the potential E_{pit} at which the passive film becomes unstable, which is marked by an increasing deviation of the current density from the passive plateau, is less noble for higher chloride concentrations. Compared to the glassy alloy, the crystalline counterpart alloy exhibits (in similar electrolytes) less noble corrosion potentials, i.e. $E_{corr} \sim -425\,mV$, and higher corrosion current densities, i.e. $i_{corr} \sim 2\,\mu A \cdot cm^{-2}$, revealing a poorer free corrosion behaviour. At low anodic polarization (in the range ±250 mV vs. SCE), the crystalline counterpart also forms stable passive films in all the electrolytes as evident from the current plateau region (considering the high value of this plateau, i.e. $\sim 200\,\mu A \cdot cm^{-2}$, a more proper denomination would be pseudo-passive films). However, these are much less protective than those grown on the glassy alloy, since the passive current densities are more than one order of magnitude higher. Similarly to the glassy alloy, the films on the crystalline counterpart become unstable at lower potentials E_{pit} with increasing chloride concentration. However, the conventional reference steel X210Cr12 does not form a passive film in these Cl^--containing environments, not even in the lowest

concentrated electrolyte. Only a small anodic polarization is needed to dramatically increase its dissolution rate. At free corrosion conditions, the diffusion-controlled oxygen reduction reaction limits its corrosion rate to a relatively low value. These significant differences in the anodic polarization behaviour clearly reveal a much better corrosion resistance of the bulk glass-forming Fe-based alloy than that of the conventional alloy.

As obvious from Fig. 4.12, there is no marked sudden increase of the anodic current density for the bulk glass-forming alloy samples, which was found to be specific for pitting initiation and rapid propagation on surfaces of Zr-based [122] or Mg based bulk glassy alloys [123]. In order to clarify the corrosion mode related to the gradual current density increase, microscopic investigations were performed on the alloy surfaces after potentiodynamic polarization tests. These were conducted similar to those shown in Fig. 4.12, but the scans were stopped when the anodic current density reached a value of $1\,\mathrm{mA}\cdot\mathrm{cm}^{-2}$. Light optical microscopy (LOM) and SEM images of polarized samples are shown in Fig. 4.13. On the surface of the glassy alloy sample even when exposed to 0.6 M NaCl, no signs of pitting corrosion were found. Instead, without cleaning with Chelaplex, a porous film was present on the surface. It is believed that the increase in current density at 500 mV vs. SCE corresponds to a transformation of the real thin and compact protective passive film to the observed porous film, which is not as protective. After cleaning the surface with Chelaplex, as shown in Fig. 4.13(a), pores were observed which have the same distribution, size and shape as the Y_2O_3 particles (see Fig. 4.3(a)). Moreover, only a few Y_2O_3 particles were found on the surface after this test. It is now evident that these pores were formed at the sites of the former particles. However, these pores do not grow further than the initial size of the pre-existing particles. In conclusion, although the Y_2O_3 particles provide a prerequisite for local breakdown of the passive film, and indeed, local dissolution occurs, pitting propagation does not take place. This proves a high pitting resistance of this alloy, or more specifically, a high repassivation ability. Referring to the small sharp current density peaks within the anodic region prior to the large current density increase beginning at the pitting potential, E_{pit}, which were recorded in the 0.01 and 0.1 M NaCl electrolytes (Fig. 4.12), it becomes clear that these correspond to the aforementioned local events. The small increase in current density at the beginning of a small peak corresponds to a local dissolution event close to a Y_2O_3 particle exposing the bare alloy surface when the particle is removed. The decrease in current density at the end of the small peak corresponds to repassivation of the respective spot at the surface. These peaks appear in the 0.01 M NaCl solution at more noble potentials than in 0.1 M NaCl and are not present at all in the 0.6 M NaCl electrolyte. Most probably, due to the higher concentration of aggressive chloride ions, they appear at less noble potentials. It follows then that the majority of these local events takes place in 0.6 M NaCl during the 1 h period before the polarization test and this is the reason for which no small peaks are seen on the corresponding polarization curve. This high repassivation ability could be caused by the relatively high content of Mo in

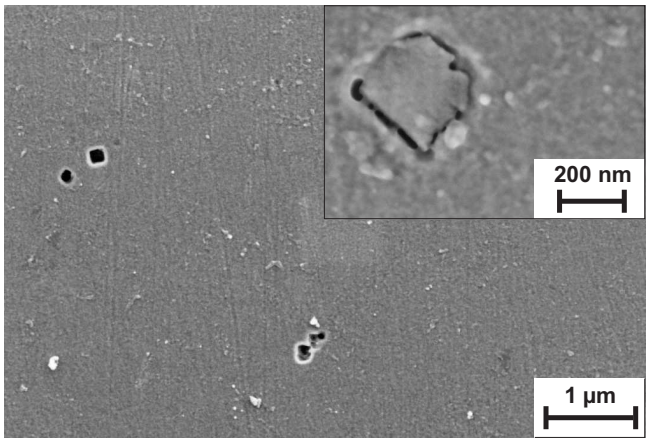

(a)

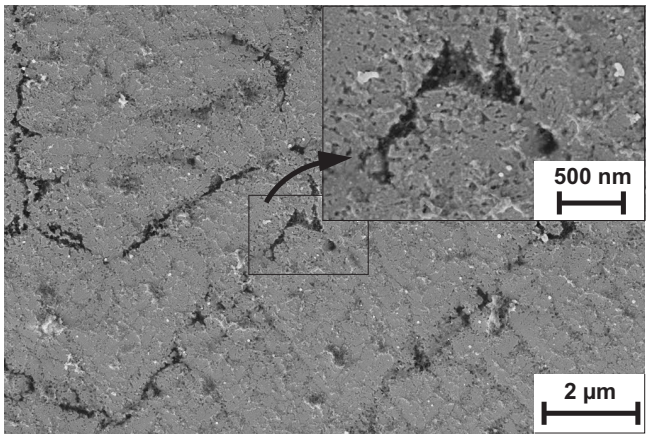

(b)

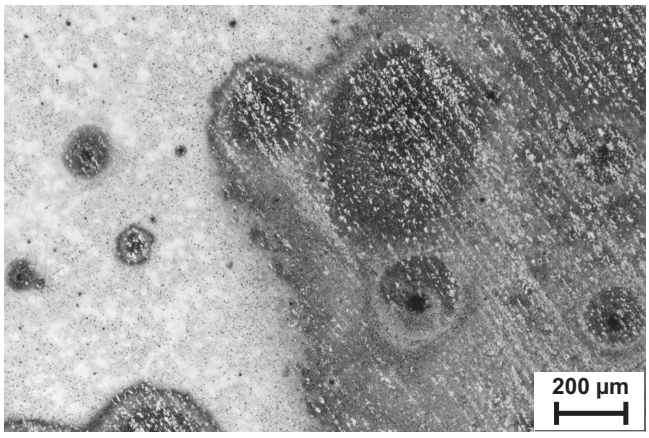

(c)

Figure 4.13: Surface images after potentiodynamic anodic polarization up to $1\,\mathrm{mA}\cdot\mathrm{cm}^{-2}$ of: (a) (SEM) bulk glassy $(Fe_{44.3}Cr_5Co_5Mo_{12.8}Mn_{11.2}C_{15.8}B_{5.9})_{98.5}Y_{1.5}$ alloy sample in 0.6 M NaCl (inset: higher magnification of a dissolving yttrium oxide particle), (b) (SEM) crystalline $(Fe_{44.3}Cr_5Co_5Mo_{12.8}Mn_{11.2}C_{15.8}B_{5.9})_{98.5}Y_{1.5}$ alloy sample in 0.6 M NaCl (inset: higher magnification of the marked area), and (c) (LOM) image of commercial steel X210Cr12 sample after potentiodynamic anodic polarization in 0.01 M NaCl.

the $(Fe_{44.3}Cr_5Co_5Mo_{12.8}Mn_{11.2}C_{15.8}B_{5.9})_{98.5}Y_{1.5}$ alloy. Alloyed Mo is known to significantly improve the repassivation ability of stainless steels [124] (see also section 2.4). With respect to the formation of those pores at the sites of the former Y_2O_3 particles in the Fe-based BMG, it is not clear yet whether they were formed by dissolution of the particles or by dissolution of the surrounding matrix leading to an excavation and subsequent detachment of the particles. The inset of Fig. 4.13(a) shows a higher magnification SEM image of a particle at an intermediate stage of dissolution. It can be seen that the local dissolution initiates at the interface. However, it is not evident whether it is the matrix, the particle, or both that dissolve(s).

A SEM image of the surface of the crystalline counterpart sample taken after the same polarization treatment in 0.6 M NaCl is shown in Fig. 4.13(b). Also in this case, no pits were observed. Instead, preferential dissolution of the secondary phase(s) takes place. SEM investigations performed on the surface of this alloy after 1 h of OCP immersion in the same electrolyte, 0.6 M NaCl, revealed no preferential dissolution. Therefore, it was concluded that the dissolution process is initiated under anodic conditions, i.e. at $-300\,\mathrm{mV}$ vs. SCE where the significant increase in current density is observed (Fig. 4.12). Following this idea, the pseudo-passive plateau observed at more noble potentials than this significant increase in current density, would then correspond to the dissolution of the interdendritic phase(s) (see the microstructure description in section 4.1.2). This is limited by the diffusion of ions in the electrolyte residing in the channels created in the place of the former phase(s). The subsequent increase in current density might correspond to the initiation of the attack on the main phase, $M_{23}(B,C)_6$.

As the LOM image in Fig. 4.13(c) shows, on the surface of the conventional steel polarized in 0.01 M NaCl, two corrosion zones were identified: one which maintains the shiny metallic appearance and contains pits (left hand side in Fig. 4.13(c)), and one which is severely corroded, similarly as in the case of the immersion test in 0.5 M H_2SO_4 (see Fig. 4.5(c)). In-between the two aforementioned zones, multiple neighbouring pits reside. These observations lead to the following interpretation: as seen in Fig. 4.11(e), in borate buffer (pH 8.4) this alloy exhibits a very low passive current density which indicates that a passive film is formed at this pH value. The formation of a passive film is expected also in the neutral 0.01 M NaCl electrolyte which has a pH value, i.e. 7, close to the one of the borate buffer. However, due to the chloride ions, this passive film is broken at weak sites, e.g. at the interface between the $(Fe,Cr)_7C_3$ phase and the αFe(Cr) matrix. Pits are formed at the respective breakdown site. Subsequently, due to their lateral growth along the matrix phase, they coalesce and form large corroded areas as observed on the right hand side of the SEM image in Fig. 4.13(c).

A comparison of the polarization behaviour in Cl^--containing electrolytes of the bulk glassy alloy $(Fe_{44.3}Cr_5Co_5Mo_{12.8}Mn_{11.2}C_{15.8}B_{5.9})_{98.5}Y_{1.5}$ to most of the other Fe-based bulk glasses can not be done in a rigorous manner because of the dissimilar test elec-

trolytes used by various authors, e.g. very acidic 1 N HCl [82], 1 and 6 N HCl [125]. However, in two of the reported works [91, 126], anodic polarization tests of an Fe-based bulk glass, $Fe_{65.5}Cr_4Mo_4Ga_4P_{12}C_5B_{5.5}$, were done in electrolytes similar to the ones used in this study, i.e. Cl^--containing 0.1 M acetate buffer electrolytes (pH $\sim$ 5) [91] and 1 N NaCl (pH 7) [126]. In the buffer electrolyte with 0.1 M NaCl, the bulk glassy $Fe_{65.5}Cr_4Mo_4Ga_4P_{12}C_5B_{5.5}$ alloy has the same passive current density as the bulk glassy $(Fe_{44.3}Cr_5Co_5Mo_{12.8}Mn_{11.2}C_{15.8}B_{5.9})_{98.5}Y_{1.5}$ alloy has in the 0.1 M NaCl electrolyte, i.e. i_{pass} $=\sim 10\,\mu A \cdot cm^{-2}$. However, the pitting potential E_{pit} of $Fe_{65.5}Cr_4Mo_4Ga_4P_{12}C_5B_{5.5}$ is 1200 mV vs. SCE which is higher than that of the $(Fe_{44.3}Cr_5Co_5Mo_{12.8}Mn_{11.2}C_{15.8}B_{5.9})_{98.5}Y_{1.5}$ alloy, i.e. 730 mV vs. SCE in the same electrolytes. Also the pitting potential E_{pit} of the $Fe_{65.5}Cr_4Mo_4Ga_4P_{12}C_5B_{5.5}$ alloy, in 1 N NaCl, i.e. 700 mV vs. SCE, is higher than that of the $(Fe_{44.3}Cr_5Co_5Mo_{12.8}Mn_{11.2}C_{15.8}B_{5.9})_{98.5}Y_{1.5}$ alloy in the less aggressive electrolyte 0.6 M NaCl, i.e. 520 mV vs. SCE. These last two observations indicate that the $(Fe_{44.3}Cr_5Co_5Mo_{12.8}Mn_{11.2}C_{15.8}B_{5.9})_{98.5}Y_{1.5}$ alloy investigated in this study has a lower pitting resistance than the $Fe_{65.5}Cr_4Mo_4Ga_4P_{12}C_5B_{5.5}$ alloy. However, the pitting susceptibility of the latter alloy exhibits a very high sensitivity to material defects manifested in much lower pitting potentials, E_{pit}, when defects are present at the exposed surface as compared to when there are no defects. On the contrary, defects at the surface of the bulk glassy $(Fe_{44.3}Cr_5Co_5Mo_{12.8}Mn_{11.2}C_{15.8}B_{5.9})_{98.5}Y_{1.5}$ alloy, i.e. Y_2O_3 inclusions, have no effect on the pitting behaviour, i.e. they do not originate pits. Leaving aside this sensitivity, the difference in pitting resistance of the two alloys is explained by their composition differences. The $Fe_{65.5}Cr_4Mo_4Ga_4P_{12}C_5B_{5.5}$ alloy would be expected to have a lower pitting resistance due to its lower Mo concentration. However, the P in its composition is stabilizing the passive film as stated by Chattoraj et al. [91] and consequently it is improving its resistance against breakdown. At the same time, the Mn in the composition of the $(Fe_{44.3}Cr_5Co_5Mo_{12.8}Mn_{11.2}C_{15.8}B_{5.9})_{98.5}Y_{1.5}$ alloy can destabilize the passive film and adversely affect the pitting resistance [104].

Summary and conclusion The bulk glassy $(Fe_{44.3}Cr_5Co_5Mo_{12.8}Mn_{11.2}C_{15.8}B_{5.9})_{98.5}Y_{1.5}$ alloy has a higher stability in Cl^--containing solutions under OCP and anodic conditions than the crystalline counterpart and the commercial steel X210Cr12. The Fe-based BMG does not suffer from pitting corrosion under the test conditions. However, Cl^- ions determine the deterioration of the passive film resulting in poorly protective porous films. At the same time, local dissolution events occur at the Y_2O_3 inclusions which, however, are stopped after the inclusions are removed due to repassivation. Pitting corrosion in the test conditions does not occur also in the case of the crystalline counterpart. Instead, anodic polarization of this crystalline alloy in Cl^--containing electrolytes results in preferential dissolution of the interdendritic phases, e.g. Co_3Mo_3C, FeY_2C_4. In the case of the conventional steel X210Cr12,

pitting easily takes place and may lead to severe dissolution on extended areas of the surface with minimal Cl^- concentration and anodic polarization. The lower pitting susceptibility of the glass and of its crystalline counterpart as compared to the conventional steel is explained mainly by the presence of Mo. Mo is also thought to be responsible for the 'self healing' effect at the Y_2O_3 inclusions.

4.5 Active dissolution in acid solutions

As mentioned in section 4.2, when exposed to 0.5 M H_2SO_4 the bulk glassy $(Fe_{44.3}Cr_5Co_5Mo_{12.8}Mn_{11.2}C_{15.8}B_{5.9})_{98.5}Y_{1.5}$ alloy corrodes under formation of characteristic morphological features on the micrometre scale. Therefore detailed microscopic surface investigations have been carried out in order to thoroughly analyze the surface morphology evolution mechanism during reaction with acid solutions both in the initial and the late stages.

4.5.1 Corrosion under open circuit conditions

Firstly, a disc sample of the bulk glassy $(Fe_{44.3}Cr_5Co_5Mo_{12.8}Mn_{11.2}C_{15.8}B_{5.9})_{98.5}Y_{1.5}$ alloy was used for long term weight loss tests in the 0.5 M H_2SO_4 solution. The sample has been periodically emerged for weight measurements and for surface analyses by SEM and AFM. The weight loss values were calculated with respect to the initial surface area of the samples. As Fig. 4.14 shows, the weight loss increases linearly with time indicating that the corrosion rate is constant.

A series of representative SEM images is shown in Fig. 4.15. The as-polished surface is very smooth except for some scratches that were generated during the polishing process (Fig. 4.15(a)). After one day of exposure in 0.5 M H_2SO_4 (Fig. 4.15(b)) numerous nano-sized pores are observed. Their mean size is 12 nm. After 100 days, as shown in Fig. 4.15(c), round-shaped micrometer-sized pits are visible on the surface of the glassy alloy. Their maximum size is around 10 µm while their minimum size could not be determined precisely because of the presence of corrosion products. These pits are clearly distinguishable from the nano-sized pores visible in Fig. 4.15(b). After this exposure time, a change in the colour of the surface from shiny metallic to brown was observed. This indicates the presence of a corrosion product layer. However, at this stage, the layer is electron-transparent which allows the visualization of the underlying morphology with SEM. After 200 days of exposure, the alloy surface changed to black colour corresponding to an increase of the layer thickness which made it completely opaque. At this stage the corrosion product layer is not only light-opaque,

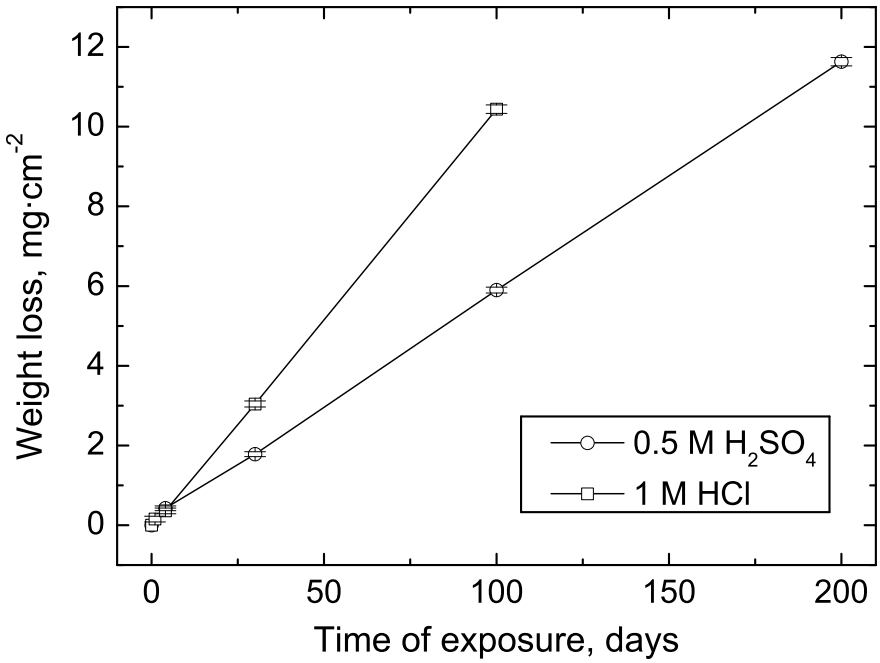

Figure 4.14: Weight loss measurement of bulk glassy $(Fe_{44.3}Cr_5Co_5Mo_{12.8}Mn_{11.2}C_{15.8}B_{5.9})_{98.5}Y_{1.5}$ alloy in 0.5 M H_2SO_4 and 1 M HCl.

but also electron-opaque. Figure 4.15(d) shows a SEM image of the surface at this stage. The corrosion product layer is not continuous, but contains many cracks. The cracks might form as a consequence of the drying process of the originally hydrated layer after removal from the electrolyte. Measurements with SEM revealed a mean thickness of the corrosion product layer after 200 days of approximately 2 µm.

More detailed SEM investigations of the exposed sample have been performed after removal of the corrosion product layer in order to better characterize the morphology of the corroded glassy alloy surface. As Fig. 4.16(a) shows, after 200 days in 0.5 M H_2SO_4 the surface of the sample is completely covered with round-shaped pits of size ranging from 0.2 to 12 µm. This large interval of values suggests that while early formed larger pits grow, new smaller pits form implying a progressive nucleation process. New pits appear at random locations; there are apparently no preferred sites for the nucleation of new pits. At higher magnification it is obvious that, as visible in Fig. 4.16(b), the surface exhibits a nano-porous structure. This substructure occurs similarly on the walls of all the larger micron-sized pits. The mean pore size of the substructure is 15 nm which is similar to the mean pore size determined after one day of exposure, i.e. 12 nm (Fig. 4.15(b)). It is therefore concluded that the same process which initially generated this nano-porous structure continues to take place in the later stages when the micron-sized pits start to form and grow. These observations suggest that although the two processes, i.e. the one causing the nano-porous structure and the one causing the micron-sized pits, take place simultaneously, they are independent from each other.

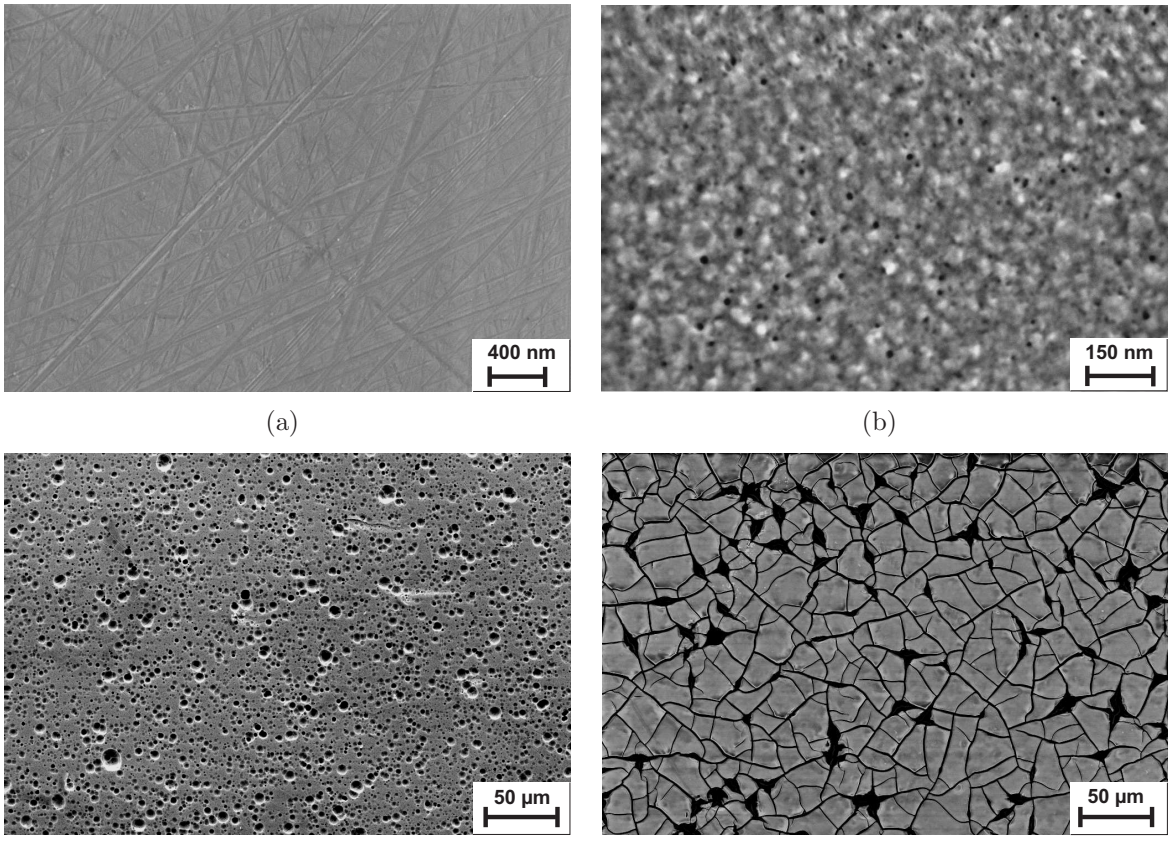

(a) (b)

(c) (d)

Figure 4.15: SEM images of the bulk glassy $(Fe_{44.3}Cr_5Co_5Mo_{12.8}Mn_{11.2}C_{15.8}B_{5.9})_{98.5}Y_{1.5}$ alloy sample: (a) before immersion; after immersion in 0.5 M H_2SO_4 (b) for 1 day, (c) for 100 days and (d) for 200 days.

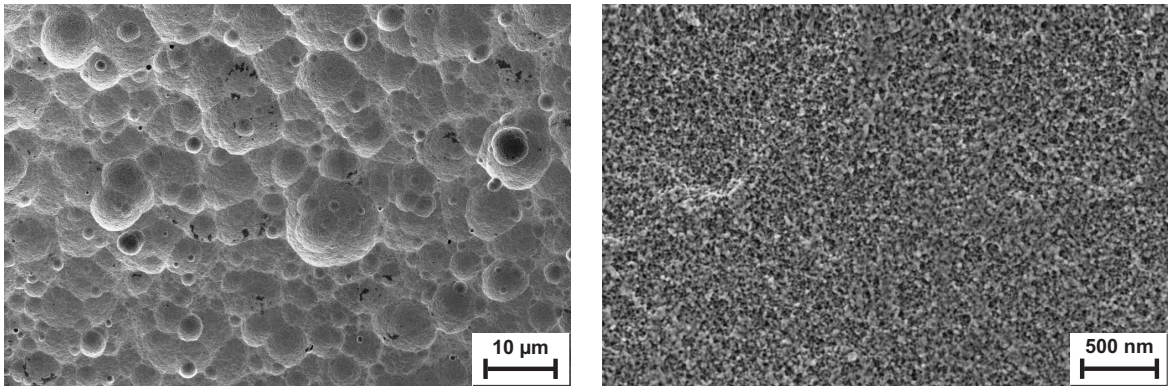

(a) (b)

Figure 4.16: SEM images of the bulk glassy $(Fe_{44.3}Cr_5Co_5Mo_{12.8}Mn_{11.2}C_{15.8}B_{5.9})_{98.5}Y_{1.5}$ alloy sample surface after 200 days in 0.5 M H_2SO_4. The corrosion layer was removed by ultrasonic treatment in Chelaplex. (a) low magnification, and (b) higher magnification.

Additional investigations of the corroded surface morphologies were conducted by atomic force microscopy (AFM). Figure 4.17(a) shows an AFM image of a glassy alloy surface which was exposed for 200 days in 0.5 M H_2SO_4 and subsequently cleaned from corrosion products. As also observed by SEM (Fig. 4.16(a)), round-shaped pits with various sizes exist. The di-

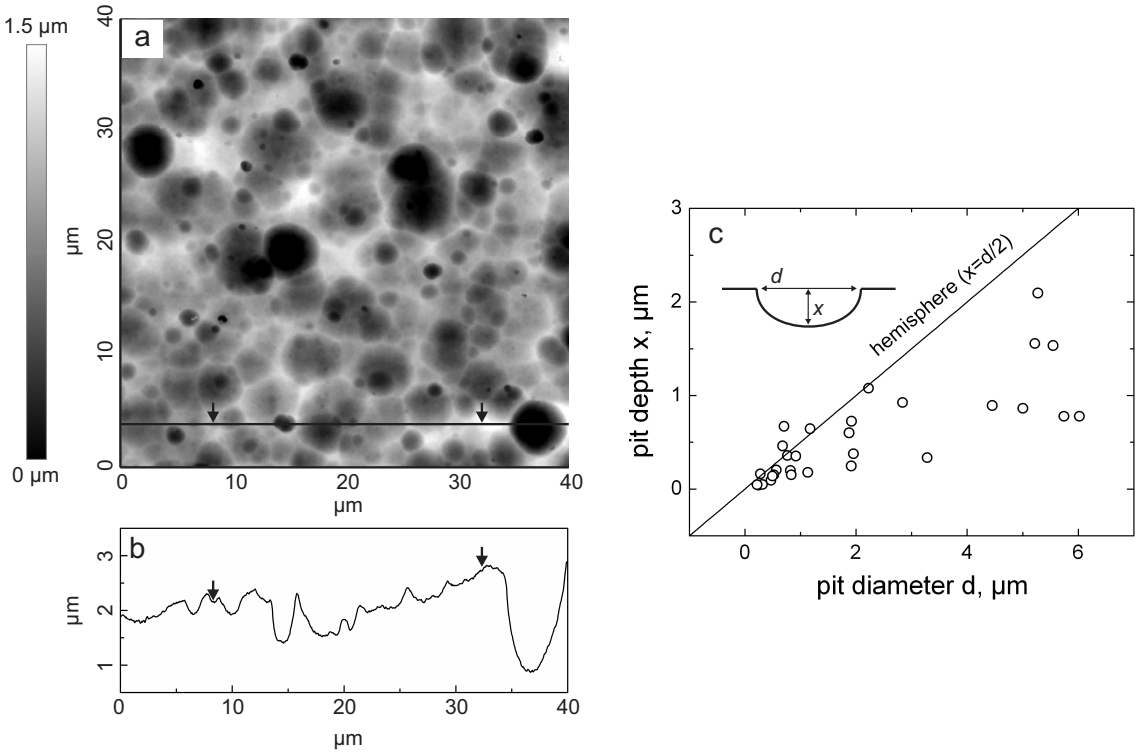

Figure 4.17: (a) Non-contact AFM image of the bulk glassy alloy $(Fe_{44.3}Cr_5Co_5Mo_{12.8}Mn_{11.2}C_{15.8}B_{5.9})_{98.5}Y_{1.5}$ sample after 200 days in 0.5 M H_2SO_4, (b) line scan corresponding to the line indicated on the image, and (c) depth versus width of 30 pits of which some can be seen in (a).

ameter of the pits as measured by AFM is between 200 nm and 6 µm. As compared to SEM, AFM provides much more detailed information on the surface topography. Pit dimensions are determined more accurately, especially in the vertical direction [127]. Indeed, as it can be seen in the line profile in Fig. 4.17(b), the shape of the pits in the vertical direction is very well defined. In order to characterize the general shape of the pits, the diameter and depth of 30 pits representing the whole size interval, i.e. 0.2–6 µm, were determined from such line profiles as the one shown in Fig. 4.17(b). Figure 4.17(c) shows a plot in which the diameter and the depth of those pits are represented. In order to compare their shape to that of a perfect hemisphere a line corresponding to this is also represented. It is evident that the shape of the majority of pits is semi-ellipsoidal, the short axis being perpendicular to the surface plane, i.e. the depth. This indicates that the corrosion front propagates on the glassy alloy surface more laterally than in depth resulting in shallow pits. Unfortunately, the nano-porous substructure visible in the SEM image in Fig. 4.16(b) could not be satisfactorily imaged with

AFM due to tip-sample convolution.
In order to determine the elemental composition of the corrosion product layer (Fig. 4.15(d)) and of the region adjacent to this, i.e the substrate, EDX investigations were carried out. For comparison, EDX analysis was also performed on the bulk glassy alloy in the as-polished state. The EDX results for the sample immersed for 200 days in 0.5 M H_2SO_4 are shown comparatively in Fig. 4.18. The corrosion product layer contains nearly all the constituent

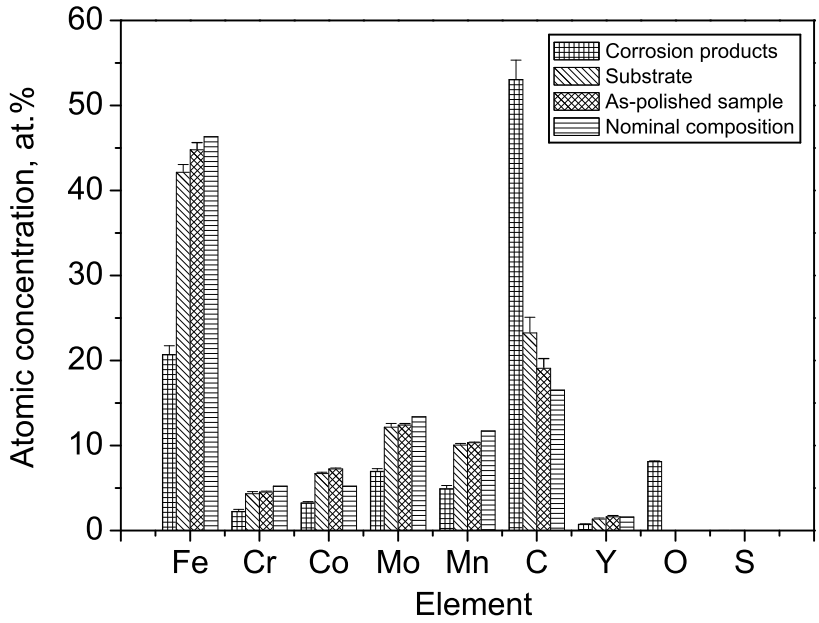

Figure 4.18: Elemental concentrations as measured by EDX of the corrosion products layer and of the underlying alloy after 200 days in 0.5 M H_2SO_4, and of the as-polished bulk glassy $(Fe_{44.3}Cr_5Co_5Mo_{12.8}Mn_{11.2}C_{15.8}B_{5.9})_{98.5}Y_{1.5}$ alloy.

elements of the bulk glassy alloy and additionally O indicating that nearly all constituents participate in layer formation. Unfortunately, B cannot be measured by EDX because of its low atomic mass. However, B is not expected to be present in the corrosion product layer since it is known to dissolve rapidly from various Fe-based glassy alloys and therefore not to be present in their passive films [26, 30, 55, 128]. Very clearly, the corrosion product layer is much richer in C while poorer in every metallic element with respect to both the substrate and the as-polished sample. Although it may be argued that the measured concentrations are not exact because the corrosion product layer is only 2 µm in thickness, and therefore, the EDX measurement can be affected by the substrate, without doubt the layer is richer in C than the underlying bulk glassy alloy. Also the substrate is enriched in C with respect to the as-polished sample, i.e. 4 at.% higher. This slight enrichment in C in the substrate zone can be an artefact due to the presence of remnant corrosion products on the surface after cleaning with Chelaplex. If this is not the case, and indeed SEM images as those in Fig. 4.16

do not show any remaining corrosion products, it can be concluded that also the substrate is, though only slightly, enriched in C. Interestingly, a similar C enrichment was observed under passive films formed at higher pH values as shown in section 4.3.3.
Another obvious aspect is that the corrosion product contains O in a significant amount, i.e. almost 10 at.%, in addition to C. Unfortunately, it can not be stated what the bonding states of O and C are. For example, they could form compounds with the metallic elements, e.g. oxides, hydroxides, carbides, carbonates. Furthermore, sulphur, S, which is present in the electrolyte, is not present in the corrosion products layer which was expected since metal sulphates are very soluble in acid aqueous solutions. In order to (perspectively) clarify which compounds constitute the corrosion products layer, experimental techniques which have the capability to detect the valence states of atoms, e.g. XPS, or the bond-types, e.g. FTIR, should be employed. The reason why the composition of the corrosion products layer and of the substrate was compared to the composition of the (as-polished) glassy alloy measured by EDX and not to its nominal composition is because EDX can give relatively high error. In order to minimize the influence of such an error on the analysis of concentration differences between the layer, the substrate and the as-polished glassy alloy, all EDX measurements were done with the same instrument and in a single measurement session. However, in order to assess the reliability of the measurements, the composition of the as-polished sample measured by EDX was compared to the nominal composition (re-normalized without B concentration)(Fig. 4.18). Except for the Co concentration which shows a deviation of 38 % from the nominal one, all the other concentrations have deviations in the range ±16 %.

4.5.2 Corrosion under anodic polarization conditions

In order to analyze anodic corrosion processes in direct relation to the surface morphology evolution of the bulk glassy $(Fe_{44.3}Cr_5Co_5Mo_{12.8}Mn_{11.2}C_{15.8}B_{5.9})_{98.5}Y_{1.5}$ alloy, potentiodynamic and potentiostatic polarization measurements in conjunction with microscopic observations have been performed. Potentiodynamic polarization tests were conducted in 0.5 M H_2SO_4 (pH 0.3) and 1 M HCl (pH 0.1) and typical curves are shown in Fig. 4.19. In 1 M HCl, the corrosion potential is more negative than in 0.5 M H_2SO_4, i.e. E_{corr}^{HCl}=−198 mV compared to $E_{corr}^{H_2SO_4}$=−37 mV. Also, the corrosion current density is higher, i.e. i_{corr}^{HCl}=10 µA · cm^{-2} compared to $E_{corr}^{H_2SO_4}$=0.23 µA · cm^{-2}. This indicates that the bulk glassy alloy exhibits higher reactivity in 1 M HCl than in 0.5 M H_2SO_4. However, during anodic polarization at potentials more positive than 200 mV, the alloy exhibits a quite similar response in both electrolytes. The overall anodic current density level is high, i.e. it reaches values of 2 and 8 mA · cm^{-2} at 1000 mV in 0.5 M H_2SO_4 and 1 M HCl, respectively. This indicates that the alloy dissolves actively in both electrolytes. Additionally, for the bulk glassy alloy a potentiostatic test was performed at 600 mV for 1 hour in 0.5 M H_2SO_4. The resulting potentiostatic curve is shown

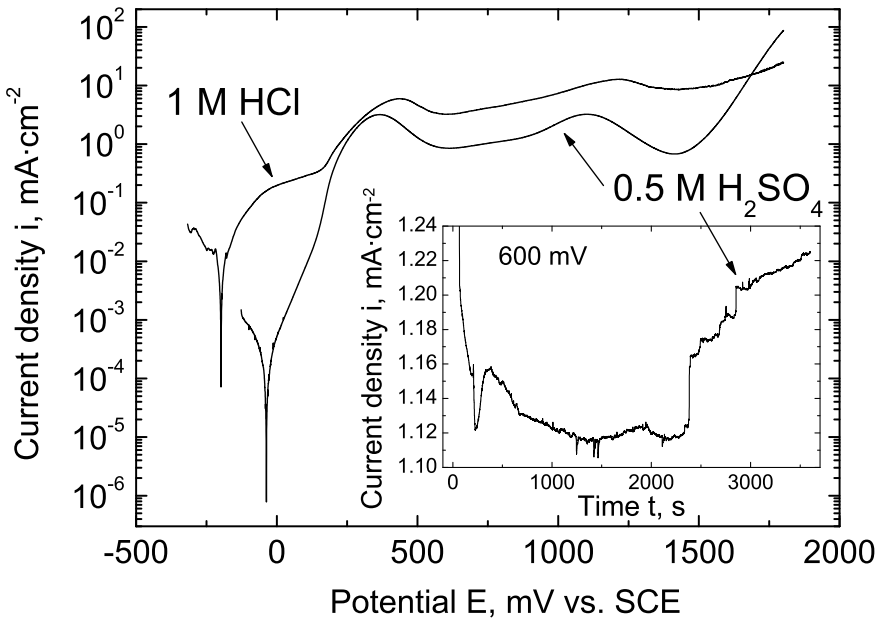

Figure 4.19: Potentiodynamic polarization curves of the bulk glassy alloy $(Fe_{44.3}Cr_5Co_5Mo_{12.8}Mn_{11.2}C_{15.8}B_{5.9})_{98.5}Y_{1.5}$ in 0.5 M H_2SO_4 and in 1 M HCl. Inset: potentiostatic polarization curve of the same alloy at 600 mV vs. SCE in 0.5 M H_2SO_4.

in the inset of Fig. 4.19. The average value of current density during this potentiostatic test, i.e. $1.17\,\mathrm{mA \cdot cm^{-2}}$, corresponds very well to the value registered during the potentiodynamic test at the same potential (600 mV), i.e. $0.85\,\mathrm{mA \cdot cm^{-2}}$. The current density value varies in a small range during the 1 hour test period, i.e. 1.10–$1.23\,\mathrm{mA \cdot cm^{-2}}$. This variation can be regarded as insignificant, but an overall trend of increase with time can be claimed after 2400 sec. This increase in current density is explained by the increase of the reactive surface area. As it will be seen later, this increase is the result of roughening of the exposed surface.

Light optical microscopy (LOM) investigations of the alloy surface performed after the complete polarization in the 0.5 M H_2SO_4 electrolyte (Fig. 4.20(a)) revealed a similar type of surface morphology as observed in the case of corrosion under open circuit conditions (Fig. 4.15(c)), i.e. after 100 days of exposure to 0.5 M H_2SO_4, where uniformly distributed round-shaped pits were found to be characteristic. This is similarly the case after complete polarization in 1 M HCl (see Fig. 4.20(b)) and after 1 hour potentiostatic polarization at 600 mV in 0.5 M H_2SO_4 (see Fig. 4.20(c)). There are fewer pits formed after potentiostatic polarization in 0.5 M H_2SO_4 than after complete potentiodynamic polarization in either of the two electrolytes. This is because less charge is consumed in this potentiostatic test. However, the principal pit morphology is similar as in all the other cases. These observations lead to the conclusion that the morphology of the actively corroded surface is not determined by the electrolyte or by the potential regime. The same $(Fe_{44.3}Cr_5Co_5Mo_{12.8}Mn_{11.2}C_{15.8}B_{5.9})_{98.5}Y_{1.5}$

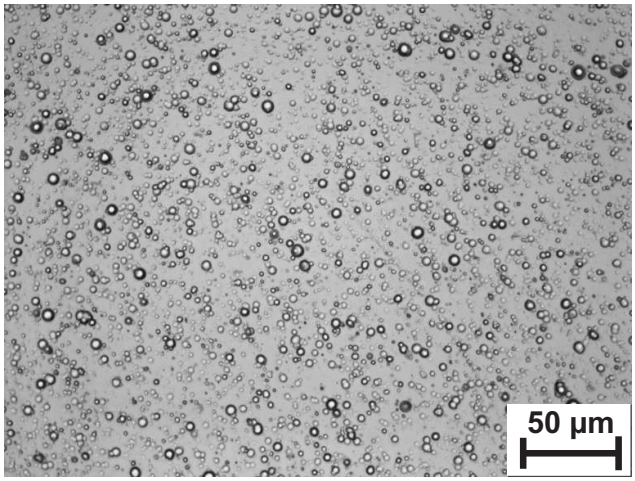

(a)

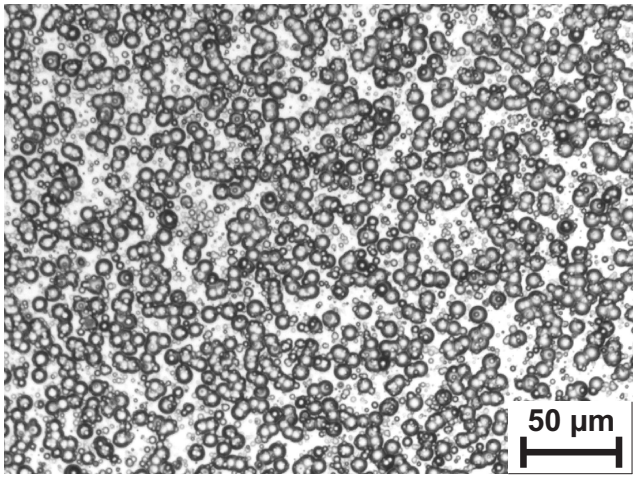

(b)

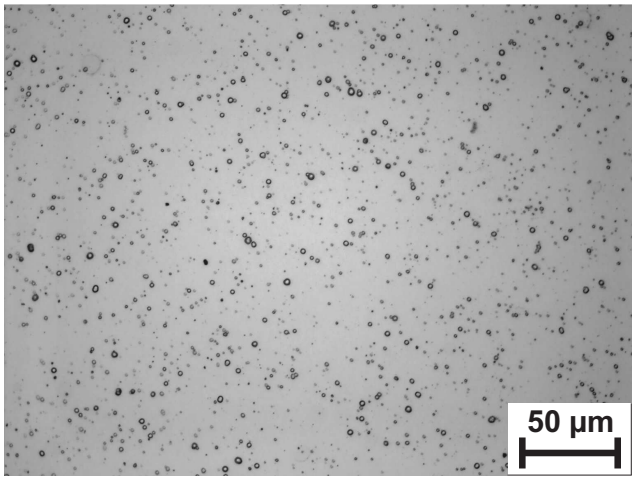

(c)

Figure 4.20: LOM images of the bulk glassy $(Fe_{44.3}Cr_5Co_5Mo_{12.8}Mn_{11.2}C_{15.8}B_{5.9})_{98.5}Y_{1.5}$ alloy sample after: (a) complete polarization cycle in 0.5 M H_2SO_4 (b) complete polarization cycle in 1 M HCl, and (c) 1 h potentiostatic polarization at 600 mV vs. SCE.

alloy, but in the shape of a melt-spun ribbon was also potentiodynamically polarized and a very similar corrosion morphology was developed in this case as well. Compared to the bulk glassy alloy sample which was polished before each experiment, the ribbon sample surface was initially used in the as-quenched state. The similarity of the surface morphology of these two samples after the corrosion tests indicates that the initial surface state is also not a decisive factor for the corrosion mode.
In conclusion, the surface morphology evolution of the bulk glassy alloy $(Fe_{44.3}Cr_5Co_5Mo_{12.8}Mn_{11.2}C_{15.8}B_{5.9})_{98.5}Y_{1.5}$ during corrosion is not determined by the kind of the acid electrolyte nor by the initial surface state or the applied potential regime. It is therefore concluded that the corrosion morphology is most likely determined by material-specific characteristics such as alloy structure and/or composition.

4.5.3 Initial corrosion stages

In order to analyze the initial stages of pit formation during metallic glass corrosion in acid solutions, in-situ AFM investigations were performed in 0.5 M H_2SO_4. For this the glassy $(Fe_{44.3}Cr_5Co_5Mo_{12.8}Mn_{11.2}C_{15.8}B_{5.9})_{98.5}Y_{1.5}$ sample was firstly exposed for 1 hour under open circuit conditions in the in-situ AFM cell and then an anodic potential of 600 mV vs. SCE was applied. AFM images were taken before applying the anodic potential and then periodically after every 10 min during polarization up to a total polarization time of 60 min. During the AFM imaging, the anodic polarization was interrupted. Selected AFM images are shown in Fig. 4.21. It can be seen that already before applying the anodic potential, i.e. after 1 hour under open circuit conditions, single small pits with a diameter of about 200 nm and a mean depth of only about 5 nm are visible (Fig. 4.21(a)). After 10 min of polarization at 600 mV vs. SCE, the same pit (it appears at a different site in the image because the sample drifts with time) has grown both in diameter and in depth. It can be seen in Fig. 4.21(b) that at this time the pit is 280 nm wide and 14 nm deep. An additional small pit appeared at the rim of this one. After 60 min (Fig. 4.21(c)) the same pit grew further reaching 800 nm in diameter and 143 nm in depth. Furthermore, new pits appear progressively at other surface sites. It is noticed that the initially very flat pits, e.g. depth:diameter=5:200 nm (Fig. 4.21(a)) grow faster in depth than in diameter resulting in nearly hemispherical shapes, e.g. 143:800 nm (Fig. 4.21(c)). As revealed by ex-situ AFM (Fig. 4.17), after 200 days under OCP conditions, the whole surface of the glassy $(Fe_{44.3}Cr_5Co_5Mo_{12.8}Mn_{11.2}C_{15.8}B_{5.9})_{98.5}Y_{1.5}$ alloy is attacked by pits and these have a round shape as the ones observed by in-situ AFM. Another similar aspect is that both modes, in-situ and ex-situ, show that the bigger pits, i.e. $> 1\,\mu m$, have a shape tending to hemispherical. However, in the case of the smaller pits, while ex-situ AFM reveals a similar shape, in-situ AFM reveals much flatter shapes. This could be caused by the partial filling of the newly created pit with corrosion products. In-situ AFM

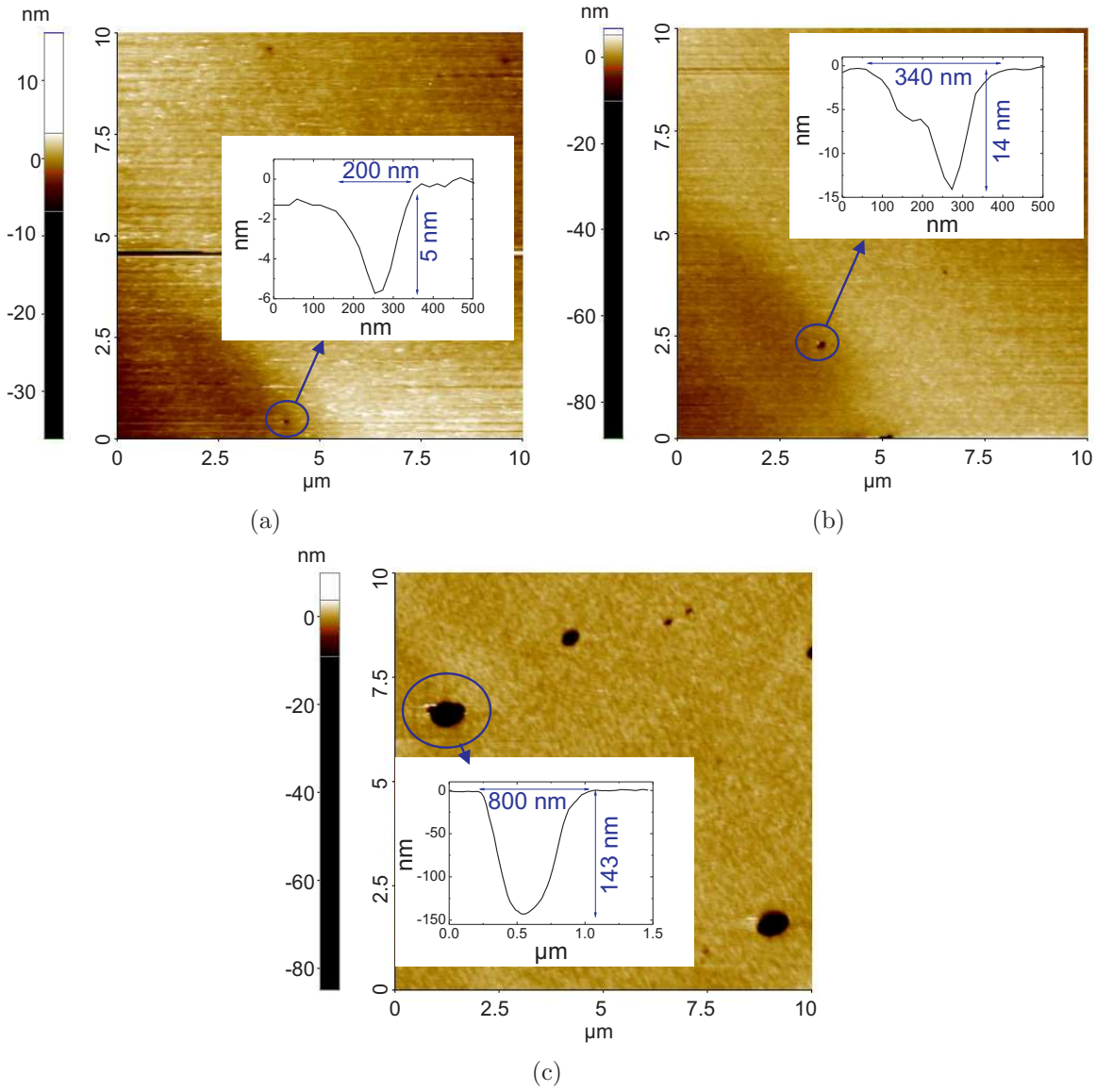

Figure 4.21: In-situ AFM images of a bulk glassy $(Fe_{44.3}Cr_5Co_5Mo_{12.8}Mn_{11.2}C_{15.8}B_{5.9})_{98.5}Y_{1.5}$ alloy sample surface in 0.5 M H_2SO_4(a) at the beginning of the polarization test (after 60 min at OCP), (b) after 10 min at 600 mV vs. SCE, and (c) after 60 min at 600 mV vs. SCE.

enabled the capability of observing in detail the evolution of the corroding surface of the glassy $(Fe_{44.3}Cr_5Co_5Mo_{12.8}Mn_{11.2}C_{15.8}B_{5.9})_{98.5}Y_{1.5}$ alloy sample at a fixed location without emerging the sample from the test electrolyte. Ex-situ investigations with AFM or SEM would require much more effort and would have the additional problem of emerging the sample from the test solution for every investigation.

In order to further analyze the very initial stages of active corrosion processes of the bulk glassy $(Fe_{44.3}Cr_5Co_5Mo_{12.8}Mn_{11.2}C_{15.8}B_{5.9})_{98.5}Y_{1.5}$ alloy at the nano-scale TEM investigations were conducted. Figure 4.22(a) shows a bright field TEM image of the as-prepared state

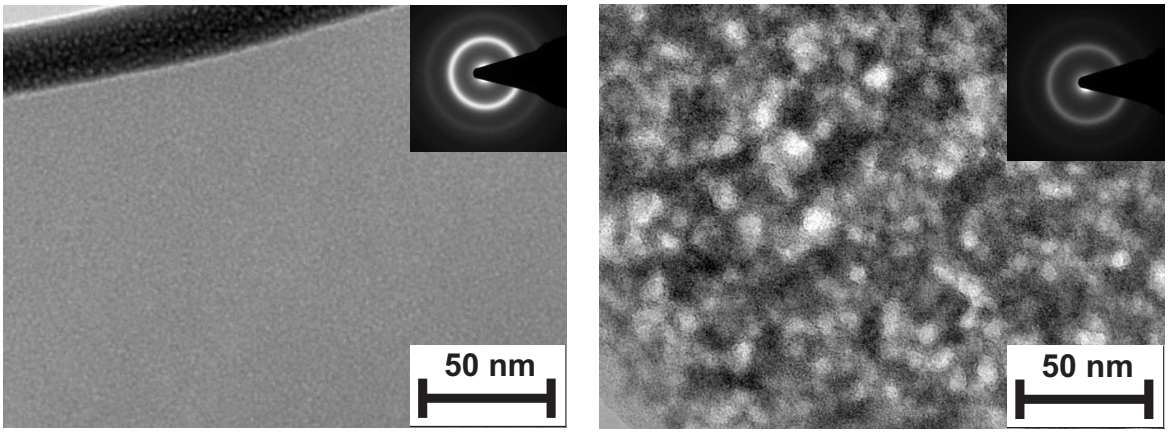

(a) (b)

Figure 4.22: TEM images of a bulk glassy $(Fe_{44.3}Cr_5Co_5Mo_{12.8}Mn_{11.2}C_{15.8}B_{5.9})_{98.5}Y_{1.5}$ alloy surface (a) before immersion and (b) after immersion in 0.5 M H_2SO_4 for 24 h. Insets: electron diffraction patterns of corresponding sample states.

of the glassy alloy. No indications of crystallinity were found with either bright or dark field imaging (dark field images not shown here). This, as well as electron diffraction patterns made at various locations (see inset of Fig. 4.22(a) for a representative electron diffraction pattern), proved the glassy nature of this sample. The same TEM foil was then immersed in 0.5 M H_2SO_4 for 24 hours and investigated again by TEM. Figure 4.22(b) shows a representative bright field image after this treatment. As it can be seen, the initially featureless sample has undergone changes that lead to the generation of characteristic features on nanoscale dimension. These have various sizes in the interval from 5 to 30 nm. Interestingly, high resolution SEM investigations reveal similar features as the ones identified by TEM (see Fig. 4.15(b) showing a SEM image of the bulk glassy alloy surface after 24 hours in 0.5 M H_2SO_4). Therefore, it is thought that the contrast in TEM images is due to the same features seen in Fig. 4.15(b). Further electron diffraction analysis of the sample immersed for 24 hours in 0.5 M H_2SO_4 indicates that these features are amorphous as is the alloy itself (see inset of Fig. 4.22(b)). Probably these features are initial corrosion products which later evolve in the much thicker film as observed by SEM (see for example Fig. 4.15(d)). EDX analysis indicated no significant difference in composition between the observed features and the surroundings.

4.5.4 Further discussion

Based on the experimental observations, a description of the evolution of the surface morphology of the bulk glassy $(Fe_{44.3}Cr_5Co_5Mo_{12.8}Mn_{11.2}C_{15.8}B_{5.9})_{98.5}Y_{1.5}$ alloy during active corrosion in acid solution can be given. This process is regarded to occur in both cases, i.e. under open circuit conditions and during anodic dissolution, and to be independent of the

nature of the electrolyte, i.e. H_2SO_4 or HCl. A schematic representation of the surface morphology evolution is given in Fig. 4.23. Upon immersion in the electrolyte, firstly two processes take place as shown in the second cartoon for t = 1 day. On the one hand, as oxidation of constituent elements takes place, a part of them is dissolved in the electrolyte, while another part is not dissolved and participates in the formation of corrosion products which precipitate at the surface. On the other hand, the surface of the alloy (beneath the corrosion products layer) undergoes transformation from the smooth as-polished state to a rough nano-porous morphology. The presence of the corrosion products layer and the nano-porous surface morphology were revealed by SEM and TEM investigations (see Fig. 4.15(b) and Fig. 4.22(b)). Later on, larger pits with diameters in the micrometer range form, as shown in the third cartoon in Fig. 4.23 for t = 100 days. These are initially some hundred of nanometres in diameter, but very shallow as revealed by in-situ AFM studies (Fig. 4.21). They subsequently grow in size mainly in depth and tend to a hemispherical shape, but in general they have a semi-ellipsoidal shape. With time the number of pits increases indicating progressive pit nucleation. Eventually the entire surface is covered by pits as shown in the fourth cartoon in Fig. 4.23 for t = 200 days. The nano-porous morphology persists in this late stage when the micrometre-sized pits develop and it is present on the whole surface including inside the pits on their walls. The corrosion products layer continues to grow in thickness in the late stages as well.

A very similar surface morphology evolution was observed by Shan et al. in the case of the bulk glassy SAM 1651 alloy ($Fe_{48}Cr_{15}Mo_{14}C_{15}B_6Y_2$) in a crevice corrosion test in 4 M NaCl at 100°C at a potential of 150 mV vs. SCE [26]. In that case, the growth of larger pores was explained to be initiated at the location of the Y_2O_3 particles. Y_2O_3 particles are also present in the alloy studied in the present work (see section 4.1.1 and [55, 112]), but their number is much lower than the number of observed pits. This leads to the conclusion that the described surface morphology evolution during acid corrosion is not directly related to the presence of those secondary phase particles, as stated in the study by Shan et al.. Moreover, it was observed that most of these particles located at the surface were removed during the surface polishing process [112].
As it was demonstrated, the surface morphology evolution during corrosion of the bulk glassy $(Fe_{44.3}Cr_5Co_5Mo_{12.8}Mn_{11.2}C_{15.8}B_{5.9})_{98.5}Y_{1.5}$ alloy is very likely due to material characteristics. Especially, the multi-component composition of this alloy is thought to be responsible for the generation of those characteristic features. The bulk glassy alloy $(Fe_{44.3}Cr_5Co_5Mo_{12.8}Mn_{11.2}C_{15.8}B_{5.9})_{98.5}Y_{1.5}$ comprises eight elements with different electrochemical behaviour. For example, while Mn is easily dissolved in acid electrolytes in a potential regime ranging from its equilibrium potential up to relatively high overpotentials, Cr is passive and, therefore, it exhibits very low dissolution currents. As well, while B is readily dissolved, C is virtually inert. It is therefore believed that, at the glassy alloy surface, selec-

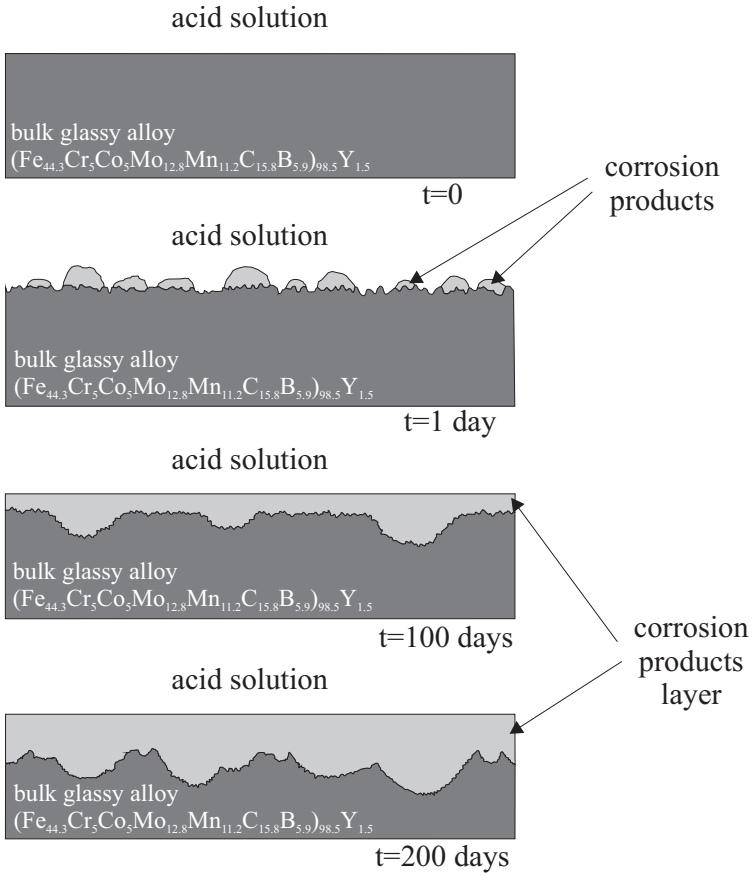

Figure 4.23: Schematic representation of the surface morphology evolution of the bulk glassy $(Fe_{44.3}Cr_5Co_5Mo_{12.8}Mn_{11.2}C_{15.8}B_{5.9})_{98.5}Y_{1.5}$ alloy during dissolution in acid solutions.

tive dissolution of the more active elements takes place while the more noble elements are enriched. For example, it was detected by EDX analysis that there is a slight enrichment in C at the surface after 200 days of immersion in 0.5 M H_2SO_4 (see section 4.5.1). The formation of the nano-porous surface is then explained similarly as in the case of the well known selective dissolution of 'higher-melting' crystalline alloys (implying a low diffusivity at room temperature) [129]. In the case of crystalline alloys the dissolution of atoms produces vacancies at the surface which subsequently agglomerate forming the so-called 'dissolution nuclei' [71]. In the case of amorphous alloys a similar process can be expected to take place noting that the 'vacancy' created by the removal of one atom from the surface can not be called 'vacancy' since this is a term defined for crystalline materials. Therefore, the initial pores which are created as a consequence of selective dissolution are expected to be very small, i.e. to be at the atomic level in the case of dissolution of a single atom or at the nanometre level in the case of agglomeration of several 'vacancies'. However, as shown in Fig. 4.16(b), the pores identified by SEM have a much larger size, i.e. a mean size of 15 nm. Unfortunately, the resolution of SEM is not sufficient to visualize those expected pores with a size in the nano-

and sub-nanometre range. The formation of larger pores observed by SEM with a mean size of 15 nm can be explained in terms of Wagner's theory [130]. A description of the mechanism in Wagner's theory which was developed for crystalline alloys is given in Ref. [71]. Figure 4.24 shows a schematic representation of the mechanism of surface roughening of an alloy in accordance with this theory. Initially, selective dissolution of alloy constituents depletes the

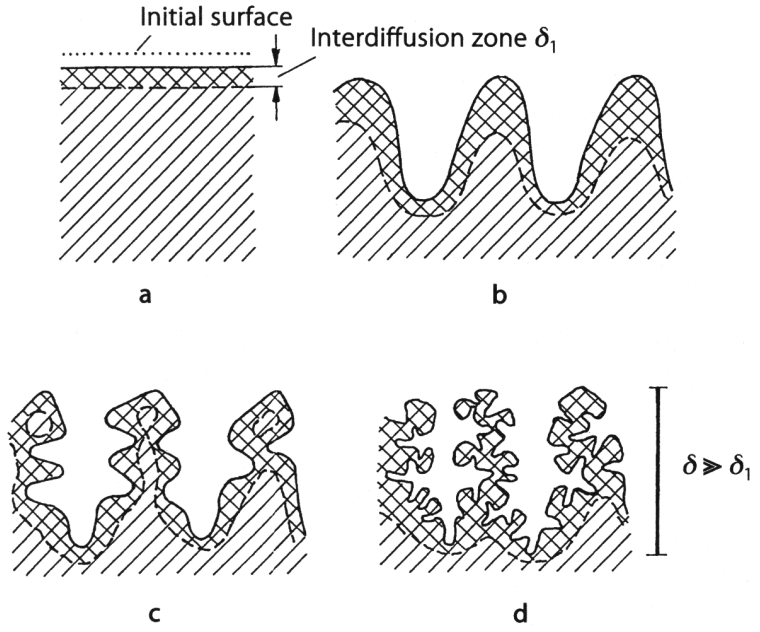

Figure 4.24: Surface roughening of an alloy by selective dissolution of less noble constituents with rate-determining volume diffusion [71].

surface concentration of the more active elements. Therefore, an inter-diffusion zone with thickness δ_1 develops. When a pore is formed as explained above, the inter-diffusion zone will be thinner at the bottom of the pore since it is fresher. However, the concentration difference across the inter-diffusion layer at the bottom of the pore will be the same as elsewhere. It follows that the concentration gradient across this layer will be higher at the bottom of the pore and, therefore, the diffusion rate of less noble constituents will be higher. This means that, if volume diffusion (and not the dissolution) is rate determining, the pore will tend to deepen, i.e. reach depths $\delta \gg \delta_1$. This is the reason, according to Wagner, for which pores will tend to grow in depth. On the contrary, owing to the Gibbs-Thomson effect pores will tend to flatten [131]. This is due to the dependence of the chemical potential of an element on the curvature of the surface favoring flat surfaces. The formation of the larger pits, i.e. $>$ 200 nm, can also be explained by the same competition of the two tendencies, i.e. roughening due to selective dissolution and flattening due to the Gibbs-Thomson effect. However, it is not yet clear why there are no pores with diameters in the interval 15 to 200 nm.

Summary It was demonstrated that active dissolution reactions of the bulk glassy $(Fe_{44.3}Cr_5Co_5Mo_{12.8}Mn_{11.2}C_{15.8}B_{5.9})_{98.5}Y_{1.5}$ alloy in acidic solutions yield characteristic morphological features of the glassy alloy surface on the micro- and nanometre scale. These morphological features are independent of the kind of electrolyte and, therefore, are thought of depending on the material characteristics. A corrosion product layer rich in C is formed on the surface which thickens with time of corrosion. For the first time, it was shown that in-situ AFM is a powerful method to study corrosion phenomena for metallic glasses. The observed morphology evolution, nano- and micro-porous structures, was explained by extrapolating selective dissolution concepts already known for crystalline alloys to this particular bulk glassy alloy. In principle, the corrosion morphology evolution is governed by the interplay between selective dissolution tending to roughen the surface and the Gibbs-Thomson effect tending to flatten the surface.

5 Summary and outlook

Recently (2004), breakthroughs in the development of Fe-based bulk glasses led to the development of new alloy compositions with remarkable glass forming ability (GFA) [1]. Considering also their relatively inexpensive cost, ease of fabrication and outstanding mechanical properties, e.g. high strength and hardness, their applicability was greatly increased. Their high brittleness is now the only drawback for their use as structural materials, but much effort is nowadays dedicated to improving their plasticity [54]. However, environmental stability is yet another decisive factor for their applicability (as for the applicability of any material), but this aspect was scarcely studied. The corrosion behaviour of their predecessors was intensely investigated (see section 2.3 for a review). But, since their composition is very different, the knowledge already acquired from the previous *non-bulk* glasses can not be extended to these newly developed *bulk* glasses. Therefore, new studies are required for the fundamental understanding of the corrosion behaviour of the recently developed Fe-based *bulk* glasses. One of the most prominent alloys of this class at the time of beginning of this work (2007), $(Fe_{44.3}Cr_5Co_5Mo_{12.8}Mn_{11.2}C_{15.8}B_{5.9})_{98.5}Y_{1.5}$, also entitled as 'structural amorphous steel' was chosen to fundamentally study the corrosion behaviour. This glassy alloy with a maximum sample thickness of 12 mm has a high thermal stability ($T_g = 804\,\mathrm{K}$), a high strength ($\sim$ 3 GPa) and hardness (1224 HV), and it is non-ferromagnetic at ambient temperatures ($T_c = \sim 55\,\mathrm{K}$) [1].

The aim of this work was to fundamentally investigate the corrosion behaviour of the bulk glassy $(Fe_{44.3}Cr_5Co_5Mo_{12.8}Mn_{11.2}C_{15.8}B_{5.9})_{98.5}Y_{1.5}$ alloy. Particularly, the free corrosion and the anodic polarization behaviour, the passivation ability and the pitting susceptibility have been assessed in electrolytes with varying pH values and anion species concentrations. For some particular aspects, a comparison was made with the crystalline $(Fe_{44.3}Cr_5Co_5Mo_{12.8}Mn_{11.2}C_{15.8}B_{5.9})_{98.5}Y_{1.5}$ counterpart alloy and with the commercial steel X210Cr12. Additionally, detailed microscopic investigations for the clarification of active dissolution mechanisms in acid solutions were conducted for the bulk glassy $(Fe_{44.3}Cr_5Co_5Mo_{12.8}Mn_{11.2}C_{15.8}B_{5.9})_{98.5}Y_{1.5}$ alloy.

Firstly, the microstructure of the three metallic materials used in this study was investigated because the particular microstructure determines decisively the corrosion behaviour. The Cu-mould cast $(Fe_{44.3}Cr_5Co_5Mo_{12.8}Mn_{11.2}C_{15.8}B_{5.9})_{98.5}Y_{1.5}$ alloy sample with 3 mm diameter is composed of a single glassy phase with a few dispersed nanometre-sized Y_2O_3 particles.

On the contrary, its crystalline counterpart obtained by Cu-mould casting (10 mm diameter) and the conventional steel X210Cr12 have multi-phase microstructures. Mainly $M_{23}(B,C)_6$ dendrites, an interdendritic η-carbide as a secondary phase and probably FeY_2C_4 as a third phase compose the crystalline counterpart. In the conventional steel, micrometre-sized $(Fe,Cr)_7C_3$ particles are surrounded by an αFe(6 at.%Cr) solid solution matrix phase.
Weight loss measurements have been performed for the bulk glassy $(Fe_{44.3}Cr_5Co_5Mo_{12.8}Mn_{11.2}C_{15.8}B_{5.9})_{98.5}Y_{1.5}$ alloy and the commercial steel X210Cr12 in 0.5 M H_2SO_4, 0.1 M Na_2SO_4, 0.6 M NaCl and 1 M NaOH. After 100 days, the bulk glassy alloy had a significant weight loss only in the acid solution while it was very stable in all the other solutions. On the contrary, the conventional steel sample used as reference exhibited much higher weight loss values in all solutions except in 1 M NaOH. This strongly deviating behaviour of the two alloys is explained by their very different microstructure, i.e. phase composition. While the bulk glassy alloy is single-phase, the conventional steel is multi-phase enabling galvanic coupling between adjacent constituent phases which strongly increases the total corrosion rate.
A major part of the study was dedicated to the analysis of the influence of the electrolyte pH value on the anodic polarization behaviour and the passivation ability of the bulk glassy $(Fe_{44.3}Cr_5Co_5Mo_{12.8}Mn_{11.2}C_{15.8}B_{5.9})_{98.5}Y_{1.5}$ alloy. For this, anodic polarization tests in combination with surface analytical studies, i.e. AES depth profiling, of surface films have been performed. In a wide pH value interval (0.3–14) the corrosion potential of the bulk glassy alloy has values nobler than the equilibrium potential of the hydrogen evolution reaction. This indicates that at free corrosion conditions depolarization is not achieved by reduction of hydrogen ions but by other reactions, e.g. reduction of dissolved oxygen. The corrosion current densities are in the pH value interval 0.3–14 relatively low, i.e. below $3\,\mu A \cdot cm^{-2}$. Its passivation ability is rather poor in acidic solutions. However, with increasing pH value of the electrolyte, the passivation ability improves dramatically due to the formation of protective surface layers mainly composed of Fe and Cr compounds, e.g. oxides/salts. Sulfate ions present in the solution negatively influence the protective effect of the passive layer most probably by incorporation of sulfate anions in the film which reduces the fraction of the more protective oxides. The poor passivation ability of the glassy alloy in acidic solutions is explained by the particular alloy composition: mainly the Cr concentration of 4.93 at.% is considered to be insufficient for the formation of a complete protective Cr-oxide-rich layer. At the same time, the concentration of Mn of 11.03 at.%, which is electrochemically active in very acidic solutions, is too high. This is a major drawback of this glassy alloy with high GFA in comparison to the early generation of Fe-based glasses with low GFA, but composition which made them highly corrosion-resistant. The passivation ability of the bulk glassy alloy may be improved by further development of the alloy composition in the limits allowed for obtaining a sufficient GFA. Particularly suggested is an increase of the concentration of Cr

to a level that enables the formation of complete, very protective oxide films and a decrease of the concentration of Mn, which deteriorates the protective effect of a passive film, to a necessary minimum.

The anodic polarization behaviour and the passivation ability of the bulk glassy $(Fe_{44.3}Cr_5Co_5Mo_{12.8}Mn_{11.2}C_{15.8}B_{5.9})_{98.5}Y_{1.5}$ alloy as function of the pH value was compared to those of its crystalline counterpart and of the commercial steel X210Cr12. In acid electrolytes the glassy alloy exhibits much lower free corrosion rates than the crystalline counterpart and the conventional steel despite the higher Cr content in the steel. This is a consequence of galvanic coupling between the $M_{23}(B,C)_6$ dendrites and the η-carbide interdendritic phase in case of the counterpart alloy, causing the preferential dissolution of the η-carbide. Also in the case of the conventional steel galvanic coupling occurs between the $(Fe,Cr)_7C_3$ particles and the αFe(Cr) matrix causing preferential dissolution of the αFe(Cr) matrix. However, during anodic polarization in acid electrolytes the single-phase bulk amorphous steel, with passivating Cr and Fe contents lower than those of the conventional steel, exhibits a lower passivation tendency (but higher compared to its multiphase crystalline counterpart). With increasing pH value, the passivation ability of the glassy alloy and of the two reference materials is improved and the galvanic coupling effects abovementioned become weaker. In very basic solutions, the influence of the galvanic coupling is minimal, and, instead, the elemental composition dominates the free corrosion and the anodic behaviour. Consequently, due to the lower passivating Fe and Cr concentration, the passive film on the glassy alloy is less protective than the one on the reference steel and equally protective to the one on the counterpart.

In chloride containing near-neutral electrolytes, the single-phase bulk glassy alloy exhibits the highest pitting resistance as compared to its crystalline counterpart and to the conventional steel. Although the Y_2O_3 particles provide favourable surface sites for pit formation and, indeed, local dissolution is initiated at their interface with the glassy matrix, pit propagation does not occur from those special sites. Therefore, these particles can be considered as mostly 'inert'. The glassy alloy exhibits a high repassivation ability in chloride electrolytes which is mainly attributed to the high content of the beneficial Mo in its composition. Compared to the bulk glassy $Fe_{65.5}Cr_4Mo_4Ga_4P_{12}C_5B_{5.5}$ alloy [91, 126], the bulk glassy $(Fe_{44.3}Cr_5Co_5Mo_{12.8}Mn_{11.2}C_{15.8}B_{5.9})_{98.5}Y_{1.5}$ alloy exhibits a lower pitting resistance, but also a lower sensitivity to pitting propagation from inclusions. The difference in pitting resistance is explained by Mn destabilizing the passive film on $Fe_{65.5}Cr_4Mo_4Ga_4P_{12}C_5B_{5.5}$ and by P stabilizing the passive film on $Fe_{65.5}Cr_4Mo_4Ga_4P_{12}C_5B_{5.5}$. The lower sensitivity of the bulk glassy $(Fe_{44.3}Cr_5Co_5Mo_{12.8}Mn_{11.2}C_{15.8}B_{5.9})_{98.5}Y_{1.5}$ alloy to pitting propagation from the Y_2O_3 inclusions is due to its high repassivation ability brought by the presence of Mo in its composition.

It was demonstrated that active dissolution reactions of the bulk glassy

$(Fe_{44.3}Cr_5Co_5Mo_{12.8}Mn_{11.2}C_{15.8}B_{5.9})_{98.5}Y_{1.5}$ alloy in acidic solutions yield characteristic morphological features at the surface on micro- and nanometre scale dimensions. The features on the micro-scale dimension are not originating at the Y_2O_3 inclusions as stated by Shan et al. [26] for another Fe-based bulk glass, i.e. $Fe_{48}Cr_{15}Mo_{14}C_{15}B_6Y_2$. It was shown that these morphological features occur independently of the kind of electrolyte and the polarization conditions. Therefore, their appearance is assumed to be strongly related to characteristics of the alloy. A corrosion product layer rich in C is formed on the surface which thickens with corrosion time. The observed morphology evolution is explained by extrapolating selective dissolution concepts already known for crystalline alloys to this particular glassy alloy. In principle, the corrosion morphology evolution is governed by the interplay between the Gibbs-Thomson effect tending to flatten the surface and selective dissolution tending to roughen the surface.

Outlook This study has demonstrated the necessity of very detailed analyzing the corrosion properties of newly developed *bulk* glass-forming Fe-based alloys. They are not per-se 'highly corrosion resistant', but their corrosion behaviour depends on their particular chemical composition. Following the findings of this study several compositional modifications of the bulk glassy $(Fe_{44.3}Cr_5Co_5Mo_{12.8}Mn_{11.2}C_{15.8}B_{5.9})_{98.5}Y_{1.5}$ alloy are suggested. First of all, an increase in Cr concentration would be very beneficial for the formation of more protective passive films. Secondly, Mn is known to destabilize passive films on stainless steels and to increase their pitting susceptibility. A similar effect is predicted in the case of the bulk glassy $(Fe_{44.3}Cr_5Co_5Mo_{12.8}Mn_{11.2}C_{15.8}B_{5.9})_{98.5}Y_{1.5}$ alloy and, therefore, decreasing its concentration is recommended. Lastly, Mo is considered. On the one hand it increases the permeability of passive films on Fe-based BMGs when present in too high concentrations. On the other hand, it has a beneficial influence on the pitting resistance. It is therefore recommended to decrease its composition to an optimal value considering both aspects. However, modifying the composition of this alloy will bring also a modification in its GFA and of course this aspect has to be taken into consideration.

In order to have a more complete understanding of the corrosion behaviour of the bulk glassy $(Fe_{44.3}Cr_5Co_5Mo_{12.8}Mn_{11.2}C_{15.8}B_{5.9})_{98.5}Y_{1.5}$ alloy and to better assess its applicability, further investigations should be conducted, e.g. crevice corrosion, corrosion under mechanical load, stress corrosion cracking, corrosion with contact materials, thermal oxidation.

In-situ AFM was for the first time used to study corrosion processes for a metallic glass and it successfully proved its high capability. This method can be applied also to other glass systems or nanostructured materials.

Bibliography

[1] Lu, Z. P., Liu, C. T., Thompson, J. R. & Porter, W. D. Structural amorphous steels. *Physical Review Letters* **92**, 245503 (2004).

[2] Vecchio, K. S. & Cheney, J. US Patent 20070253856 Low Cost Amorphous Steel (2007).

[3] Wang, H. J., Shiflet, G. J., Poon, S. J., Matsuda, K. & Ikeno, S. The role of Y/lanthanides on the glass forming ability of amorphous steel. *Applied Physics Letters* **91** (2007).

[4] Demetriou, M. D., Kaltenboeck, G., Suh, J.-Y., Garrett, G., Floyd, M., Crewdson, C., Hofmann, D. C., Kozachkov, H., Wiest, A., Schramm, J. P. & Johnson, W. L. Glassy steel optimized for glass-forming ability and toughness. *Applied Physics Letters* **95** (2009).

[5] Inoue, A. & Takeuchi, A. Recent progress in bulk glassy alloys. *Materials Transactions* **43**, 1892–1906 (2002).

[6] Blink, J., Farmer, J., Choi, J. & Saw, C. Applications in the Nuclear Industry for Thermal Spray Amorphous Metal and Ceramic Coatings. *Metallurgical and Materials Transactions A - Physical Metallurgy and Materials Science* **40A**, 1344–1354 (2009). MS&T 2007 Meeting SEP 16-20, 2007 Detroit, MI.

[7] Lu, Z. P., Liu, C. T. & Porter, W. D. Role of yttrium in glass formation of Fe-based bulk metallic glasses. *Applied Physics Letters* **83**, 2581–2583 (2003).

[8] Ponnambalam, V., Poon, S. J. & Shiflet, G. J. Fe-based bulk metallic glasses with diameter thickness larger than one centimeter. *Journal of Materials Research* **19**, 1320–1323 (2004).

[9] Shen, J., Chen, Q. J., Sun, J. F., Fan, H. B. & Wang, G. Exceptionally high glass-forming ability of an FeCoCrMoCBY alloy. *Applied Physics Letters* **86**, 151907 (2005).

[10] Luo, C. Y., Zhao, Y. H., Xi, X. K., Wang, G., Zhao, D. Q., Pan, M. X., Wang, W. H. & Kou, S. Z. Making amorphous steel in air by rare earth microalloying. *Journal of Non-Crystalline Solids* **352**, 185–188 (2006).

[11] Li, H. X., Kim, K. B. & Yi, S. Enhanced glass-forming ability of Fe-based bulk metallic glasses prepared using hot metal and commercial raw materials through the optimization of Mo content. *Scripta Materialia* **56**, 1035–1038 (2007).

[12] Pan, J., Chen, Q., Li, N. & Liu, L. Formation of centimeter Fe-based bulk metallic glasses in low vacuum environment. *Journal of Alloys and Compounds* **463**, 246–249 (2008).

[13] Wang, W. H. Roles of minor additions in formation and properties of bulk metallic glasses. *Progress in Materials Science* **52**, 540–596 (2007).

[14] Hashimoto, K. 2002 W.R. Whitney Award Lecture: In pursuit of new corrosion-resistant alloys. *Corrosion* **58**, 715–722 (2002).

[15] Kilian, R. & Schultz, L. High-temperature corrosion of iron-based amorphous-alloys. *Zeitschrift Fur Physikalische Chemie Neue Folge* **157**, 165–170 (1988).

[16] Ponnambalam, V., Poon, S. J. & Shiflet, G. J. Fe-Mn-Cr-Mo-(Y,Ln)-C-B (Ln = lanthanides) bulk metallic glasses as formable amorphous steel alloys. *Journal of Materials Research* **19**, 3046–3052 (2004).

[17] Hashimoto, K. *Amorphous Metallic Alloys*, chap. Chemical properties, 471–486 (Butterworths, 1983).

[18] Scully, J. R., Gebert, A. & Payer, J. H. Corrosion and related mechanical properties of bulk metallic glasses. *Journal of Materials Research* **22**, 302–313 (2007).

[19] Archer, M. D., Corke, C. C. & Harji, B. H. The Electrochemical Properties of Metallic Glasses. *Electrochimica Acta* **32**, 13–26 (1987).

[20] Feser, R. *Encyclopedia of Electrochemistry*, vol. Corrosion and oxide films, chap. Uniform Corrosion of Metals in Acid, Neutral and Alkaline Electrolytes, 67–107 (Wiley-VCH, 2003).

[21] Martin, F. A., Bataillon, C. & Cousty, J. In situ AFM detection of pit onset location on a 304L stainless steel. *Corrosion Science* **50**, 84–92 (2008).

[22] Green, B. A., Steward, R. V., Kim, I., Choi, C. K., Liaw, P. K., Kihm, K. D. & Yokoyama, Y. In situ observation of pitting corrosion of the Zr50Cu40Al10 bulk metallic glass. *Intermetallics* **17**, 568–571 (2009).

[23] Wang, Z. M., Zhang, J., Chang, X. C., Hou, W. L. & Wang, J. Q. Structure inhibited pit initiation in a Ni-Nb metallic glass. *Corrosion Science* **52**, 1342–1350 (2010).

[24] Waseda, Y. & Aust, K. T. Corrosion behavior of metallic glasses. *Journal of Materials Science* **16**, 2337–2359 (1981).

[25] Pang, S. J., Zhang, T., Asami, K. & Inoue, A. Bulk glassy Fe-Cr-Mo-C-B alloys with high corrosion resistance. *Corrosion Science* **44**, 1847–1856 (2002).

[26] Shan, X., Ha, H. & Payer, J. H. Comparison of Crevice Corrosion of Fe-Based Amorphous Metal and Crystalline Ni-Cr-Mo Alloy. *Metallurgical and Materials Transactions A - Physical Metallurgy and Materials Science* **40A**, 1324–1333 (2009). MS&T 2007 Meeting SEP 16-20, 2007 Detroit, MI.

[27] Vishwanadh, B., Balasubramaniam, R., Srivastava, D. & Dey, G. K. Effect of surface morphology on atmospheric corrosion behaviour of Fe-based metallic glass, Fe67Co18Si14B1. *Bulletin of Materials Science* **31**, 693–698 (2008).

[28] Long, Z. L., Shen, B. L., Shao, Y., Chang, C. T., Zeng, Y. Q. & Inoue, A. Corrosion behaviour of [(Fe0.6Co0.4)0.75B0.2Si0.05]96Nb4 bulk glassy alloy in sulphuric acid solutions. *Materials Transactions* **47**, 2566–2570 (2006).

[29] Li, H. X. & Yi, S. Corrosion behaviors of bulk metallic glasses Fe66.7C7.0S3.3B5.5P8.7Cr2.3Al2.0Mo4.5 having different crystal volume fractions. *Materials Chemistry and Physics* **112**, 305–309 (2008).

[30] Angelini, E., Antonione, C., Baricco, M., Bianco, P., Rosalbino, F. & Zucchi, F. Corrosion Behavior of Fe80-XCoXB10Si10 Metallic Glasses in Sulfate and Chloride Media. *Werkstoffe Und Korrosion-Materials and Corrosion* **44**, 98–106 (1993).

[31] Davies, H. *Amorphous Metallic Alloys*, chap. Metallic glass formation, 8–25 (Butterworths, 1983).

[32] Turnbull, D. Under what conditions can a glass be formed? *Contemporary Physics* **10**, 473–488 (1969).

[33] Cahn, R. & Greer, A. *Physical Metallurgy*, vol. 2, chap. Metastable States of Alloys, 1723–1830 (Elsevier Science BV, 1996).

[34] Mader, S., Nowick, A. & Widmer, H. Metastable Evaporated Thin Films of Cu-Ag and Co-Au Alloys. I. Occurence and Morphology of Phases. *Acta Metallurgica* **15**, 203–214 (1967).

[35] Simpson, A. & Hodkinso, P. Bubble Raft Model for an Amorphous Alloy. *Nature* **237**, 320–322 (1972).

[36] Yavari, A. Small Volume Change on Melting as a New Criterion for Easy Formation of Metallic Glasses. *Physics Letters A* **95**, 165–168 (1983).

[37] Inoue, A., Wang, X. M. & Zhang, W. Developments and applications of bulk metallic glasses. *Reviews on Advanced Materials Science* **18**, 1–9 (2008).

[38] Long, Z., Wei, H., Ding, Y., Zhang, P., Xie, G. & Inoue, A. A new criterion for predicting the glass-forming ability of bulk metallic glasses. *Journal of Alloys and Compounds* **475**, 207–219 (2009).

[39] Inoue, A. & Takeuchi, A. Recent progress in bulk glassy, nanoquasicrystalline and nanocrystalline alloys. *Materials Science and Engineering A* **375-377**, 16 – 30 (2004).

[40] Siegel, U. *Strukturelle, thermische und mechanische Charakterisierung von amorphen Eisenbasislegierungen und Glasmatrixkompositen*. Ph.D. thesis, TU Dresden (2010).

[41] Greer, A. L. & Ma, E. Bulk metallic glasses: At the cutting edge of metals research. *MRS Bulletin* **32**, 611–615 (2007).

[42] Bernal, J. Geometry of the Structure of Monoatomic Liquids. *Nature* **185**, 68–70 (1960).

[43] Gaskell, P. New Structural Model for Transition Metal-Metalloid Glasses. *Nature* **276**, 484–485 (1978).

[44] Sheng, H. W., Luo, W. K., Alamgir, F. M., Bai, J. M. & Ma, E. Atomic packing and short-to-medium-range order in metallic glasses. *Nature* **439**, 419–425 (2006).

[45] Miracle, D. B. A structural model for metallic glasses. *Nature Materials* **3**, 697–702 (2004).

[46] Nakamura, T., Matsubara, E., Imafuku, M., Koshiba, H., Inoue, A. & Waseda, Y. Structural study of amorphous Fe70M10B20 (M = Cr, W, Nb, Zr and Hf) alloys by X-ray diffraction. *Materials Transactions* **42**, 1530–1534 (2001).

[47] Imafuku, M., Yaoita, K., Sato, S., Zhang, W. & Inoue, A. Effect of lanthanide element on glass-forming ability and local atomic structure of Fe-Co-(Ln)-B amorphous alloys. *Materials Transactions JIM* **40**, 1144–1148 (1999).

[48] Schroers, J. Processing of Bulk Metallic Glass. *Advanced Materials* **22**, 1566–1597 (2010).

[49] Spaepen, F. Homogeneous flow of metallic glasses: A free volume perspective. *Scripta Materialia* **54**, 363 – 367 (2006).

[50] Inoue, A., Shen, B. & Takeuchi, A. Fabrication, properties and applications of bulk glassy alloys in late transition metal-based systems. *Materials Science and Engineering A - Structural Materials Properties Microstructure and Processing* **441**, 18–25 (2006).

[51] Luborsky, F., Livingston, J. & Chin, G. *Physical Metallurgy*, vol. 3, chap. Magnetic Properties of Metals and Alloys, 2501–2565 (Elsevier Science BV, 1996), 4th edn.

[52] Inoue, A., Shinohara, Y. & Gook, J. Thermal and magnetic properties of bulk Fe-based glassy alloys prepared by copper mold casting. *Materials Transactions JIM* **36**, 1427–1433 (1995).

[53] Ponnambalam, V., Poon, S. J., Shiflet, G. J., Keppens, V. M., Taylor, R. & Petculescu, G. Synthesis of iron-based bulk metallic glasses as nonferromagnetic amorphous steel alloys. *Applied Physics Letters* **83**, 1131–1133 (2003).

[54] Gu, X. J., Poon, S. J. & Shiflet, G. J. Mechanical properties of iron-based bulk metallic glasses. *Journal of Materials Research* **22**, 344–351 (2007).

[55] Gostin, F., Siegel, U., Mickel, C., Baunack, S., Gebert, A. & Schultz, L. Corrosion behavior of the bulk glassy (Fe44.3Cr5Co5Mo12.8Mn11.2C15.8B5.9)(98.5)Y1.5 alloy. *Journal of Materials Research* **24**, 1471–1479 (2009).

[56] Stoica, M., Degmova, J., Roth, S., Eckert, J., Grahl, H., Schultz, L., Yavari, A., Kvick, A. & Heunen, G. Magnetic properties and phase transformations of bulk amorphous Fe-Based alloys obtained by different techniques. *Materials Transactions* **43**, 1966–1973 (2002).

[57] Stoica, M., Eckert, J., Roth, S., Zhang, Z., Schultz, L. & Wang, W. Mechanical behavior of Fe65.5Cr4Mo4Ga4P12C5B5.5 bulk metallic glass. *Intermetallics* **13**, 764 – 769 (2005).

[58] Pang, S., Zhang, T., Asami, K. & Inoue, A. Effects of chromium on the glass formation and corrosion behavior of bulk glassy Fe-Cr-Mo-C-B alloys. *Materials Transactions JIM* **43**, 2137–2142 (2002).

[59] Bitoh, T., Makino, A., Inoue, A. & Greer, A. Large bulk soft magnetic [(Fe0.5Co0.5)0.75B0.20Si0.05]96Nb4 glassy alloy prepared by B2O3 flux melting and water quenching. *Applied Physics Letters* **88**, 182510 (2006).

[60] Bitoh, T., Makino, A., Inoue, A. & Greer, A. Formation of Large Bulk [(Fe0.5Co0.5)0.75B0.20Si0.05]96Nb4 Glassy Alloy by Flux Melting and Water Quenching. In *Mater. Res. Soc. Symp. Proc. 903E*, vol. 903E (2006).

[61] Stoica, M., Hajlaoui, K., Lemoulec, A. & Yavari, A. New ternary Fe-based bulk metallic glass with high boron content. *Philosophical Magazine Letters* **86**, 267–275 (2006).

[62] Stoica, M., Hajlaoui, K., Das, J., Eckert, J. & Yavari, A. R. FeNbB bulk metallic glass with high boron content. *Reviews on Advanced Materials Science* **18**, 61–65 (2008).

[63] Long, Z. L., Shao, Y., Xie, G. Q., Zhang, P., Shen, B. L. & Inoue, A. Enhanced soft-magnetic and corrosion properties of Fe-based bulk glassy alloys with improved plasticity through the addition of Cr. *Journal of Alloys and Compounds* **462**, 52–59 (2008).

[64] Li, X., Chang, C. T., Kubota, T., Qin, C. L., Makino, A. & Inoue, A. Effect of Cr Addition on the Glass-Forming Ability, Magnetic, Mechanical and Corrosion Properties of (Fe0.76Si0.096B0.096P0.048)(100-x)Cr-x Bulk Glassy Alloys. *Materials Transactions* **49**, 2887–2890 (2008).

[65] Liu, F., Pang, S., Li, R. & Zhang, T. Ductile Fe-Mo-P-C-B-Si bulk metallic glasses with high saturation magnetization. *Journal of Alloys and Compounds* **483**, 613–615 (2009).

[66] Feser, R. *Encyclopedia of Electrochemistry*, vol. Corrosion and oxide films (Wiley-VCH, 2003).

[67] Landolt, D. & Frankel, G. *Encyclopedia of Electrochemistry*, vol. Corrosion and Oxide Films, chap. Kinetics of Electrolytic Corrosion Reactions, 25–49 (Wiley-VCH, 2003).

[68] Latanision, R. M., J. C. Turn, J. & Compeau, C. R. The corrosion resistance of metallic glasses. In Miller, K. J. & Smith, R. F. (eds.) *ICM3*, vol. 2 of *International Series on the Strength and Fracture of Materials and Structures*, 475–483 (Pergamon Press, 1979).

[69] Heusler, K. E. & Huerta, D. Kinetics and mechanisms of the anodic dissolution of metallic glasses. *Journal of the Electrochemical Society* **136**, 65–71 (1989).

[70] Naka, M., Hashimoto, K. & Masumoto, T. Corrosion Resistivity of Amorphous Iron Alloys Containing Chromium. *Journal of the Japan Institute of Metals* **38**, 835–841 (1974).

[71] Kaesche, H. *Corrosion of Metals. Physicochemical Principles and Current Problems* (Springer, 2003).

[72] Dutta, R. S., Savalia, R. T. & Dey, G. K. Corrosion behaviour of rapidly solidified Zr76Ni16Fe8 alloy in chloride environments. *Scripta Metallurgica Et Materialia* **32**, 207–212 (1995).

[73] Gebert, A., Eckert, J. & Schultz, L. Effect of oxygen on phase formation and thermal stability of slowly cooled Zr65Al7.5Cu7.5Ni10 metallic glass. *Acta Materialia* **46**, 5475–5482 (1998).

[74] Gebert, A., Mummert, K., Eckert, J., Schultz, L. & Inoue, A. Electrochemical investigations on the bulk glass forming Zr55Cu30Al10Ni5 alloy. *Materials and Corrosion-Werkstoffe Und Korrosion* **48**, 293–297 (1997).

[75] Vishwanadh, B., Abraham, G. J., Neogy, J. S., Dutta, R. S. & Dey, G. K. Effect of Structural Defects, Surface Irregularities, and Quenched-In Defects on Corrosion of Zr-Based Metallic Glasses. *Metalurgical and Materials Transactions A - Physical Metallurgy and Materials Science* **40A**, 1131–1141 (2009).

[76] Mudali, U. K., Baunack, S., Eckert, J., Schultz, L. & Gebert, A. Pitting corrosion of bulk glass-forming zirconium-based alloys. *Journal of Alloys and Compounds* **377**, 290–297 (2004).

[77] Janikczachor, M. An electrochemical investigation of Fe75B25-xSix amorphous alloys. *Werkstoffe Und Korrosion-Materials and Corrosion* **34**, 451–453 (1983).

[78] Halada, G., Clayton, C., Herman, H., Sampath, S. & Tiwari, R. An x-ray photoelectron spectroscopic study of the passive film formed on pure Mo and MoSi2 in 4 M HCl. *Journal of the Electrochemical Society* **142**, 74–81 (1995).

[79] Falkenberg, F., Raja, V. S. & Ahlberg, E. An alternative explanation for the apparent passivation of molybdenum in 1 mol/L hydrochloric acid. *Journal of the Electrochemical Society* **148**, B132–B137 (2001).

[80] Habazaki, H., Kawashima, A., Asami, K. & Hashimoto, K. The effect of molybdenum on the corrosion behavior of amorphous Fe-Cr-Mo-P-C alloys in hydrochloric acid. *Materials Science and Engineering A-Structural Materials Properties Microstructure and Processing* **134**, 1033–1036 (1991).

[81] Asami, K., Naka, M., Hashimoto, K. & Masumoto, T. Effect of Molybdenum on the Anodic Behavior of Amorphous Fe-Cr-Mo-B Alloys in Hydrochloric Acid. *Journal of the Electrochemical Society* **127**, 2130–2138 (1980).

[82] Pang, S. J., Zhang, T., Asami, K. & Inoue, A. Formation of bulk glassy Fe75-x-yCrxMoyC15B10 alloys and their corrosion behavior. *Journal of Materials Research* **17**, 701–704 (2002).

[83] Habazaki, H., Kawashima, A., Asami, K. & Hashimoto, K. The effect of tungsten on the corrosion behaviour of amorphous Fe-Cr-W-P-C alloys in 1 M HCl. *Journal of the Electrochemical Society* **138**, 76–81 (1991).

[84] Fang, H. Z., Hui, X. D. & Chen, G. L. Effects of Mn addition on the magnetic property and corrosion resistance of bulk amorphous steels. *Journal of Alloys and Compounds* **464**, 292–295 (2008).

[85] Wang, Z. M., Ma, Y. T., Zhang, J., Hou, W. L., Chang, X. C. & Wang, J. Q. Influence of yttrium as a minority alloying element on the corrosion behavior in Fe-based bulk metallic glasses. *Electrochimica Acta* **54**, 261–269 (2008).

[86] Wang, Z. M., Zhang, J., Chang, X. C., Hou, W. L. & Wang, J. Q. Susceptibility of minor alloying to corrosion behavior in yttrium-containing bulk amorphous steel. *Intermetallics* **16**, 1036–1039 (2008).

[87] Janikczachor, M. Effect of metalloid elements on passivity of glassy metals. *Langmuir* **3**, 910–916 (1987).

[88] Naka, M., Hashimoto, K. & Masumoto, T. Effect of metalloidal elements on corrosion-resistance of amorphous iron-chromium alloys. *Journal of Non-Crystalline Solids* **28**, 403–413 (1978).

[89] Virtanen, S., Elsener, B. & Bohni, H. Effect of metalloids on the passivity of amorphous Fe-Cr alloys. *Journal of the Less-Common Metals* **145**, 581–593 (1988).

[90] Elsener, B., Virtanen, S. & Boehni, H. Corrosion and passivation of amorphous and crystalline Fe-Cr alloys in ethanol-water-HCl mixtures. *Electrochimica Acta* **32**, 927–934 (1987).

[91] Chattoraj, I., Baunack, S., Stoica, M. & Gebert, A. Electrochemical Response of Fe65.5Cr4Mo4Ga4P12C5B5.5 Bulk Amorphous Alloy in Different Aqueous Media. *Materials and Corrosion-Werkstoffe Und Korrosion* **55**, 36–42 (2004).

[92] Elsener, B. & Rossi, A. XPS investigation of passive films on amorphous Fe-Cr alloys. *Electrochimica Acta* **37**, 2269 – 2276 (1992).

[93] Janikczachor, M. Effect of Si on the corrosion behaviour of Fe-B and Fe-Ni-B glassy alloys. *Werkstoffe Und Korrosion-Materials and Corrosion* **36**, 441–446 (1985).

[94] Janikczachor, M. Localized corrosion of Fe-B-Si glassy alloys. *Journal of the Electrochemical Society* **132**, 306–309 (1985).

[95] Scully, J. R. & Lucente, A. *ASM Handbook*, vol. 13B, chap. Corrosion of Amorphous Metals, 476–489 (2005).

[96] Pourbaix, M. *Atlas of Electrochemical Equilibria in Aqueous Solutions* (Pergamon Press, Elmsford, NY, 1966).

[97] Gohr, H. & Lange, E. Der innere elektrische Potentialabfall in der Passivitatsschicht des Eisens und die Flade-bezugsspannung (Fladepotential). *Naturwissenschaften* **43**, 12–13 (1956).

[98] Wagner, C. Models for lattice-defects in oxide layers on passivated iron and nickel. *Berichte der Bunsengesellschaft fur physicalische Chemie* **77**, 1090–1097 (1973).

[99] Nishimura, R. & Sato, N. Potential-pH diagram of Composition/Structure of Passive Films on Iron. *Journal of the Japan Institute of Metals* **47**, 1086–1093 (1983).

[100] Badawy, W. A., Al-Kharafi, F. M. & Al-Ajmi, J. R. Electrochemical Behaviour of Cobalt in Aqueous Solutions of Different pH. *Journal of Applied Electrochemistry* **30**, 693–704 (2000).

[101] Urquidi-Macdonald, M. & Macdonald, D. D. Theoretical Analysis of the Effects of Alloying Elements on Distribution Functions of Passivity Breakdown. *Journal of The Electrochemical Society* **136**, 961–967 (1989).

[102] Wegrelius, L., Falkenberg, F. & Olefjord, I. Passivation of Stainless Steels in Hydrochloric Acid. *Journal of The Electrochemical Society* **146**, 1397–1406 (1999).

[103] Schneider, A., Kuron, D., Hofmannn, S. & Kirchheim, R. AES Analysis of Pits and Passive Films Formed on Fe-Cr, Fe-Mo and Fe-Cr-Mo Alloys. *Corrosion Science* **31**, 191–196 (1990).

[104] Lunarska, E., Szklarskasmialowska, Z. & Janikczachor, M. Susceptibility of Cr-Ni-Mn stainless-steels to pitting in chloride solutions. *Corrosion* **31**, 231–234 (1975).

[105] Raja, V. S., Devasenapathi, A., Veluchamy, P. & Minoura, H. Electron spectroscopy for chemical analysis study of corrosion films formed on manganese stainless steels. *Corrosion* **55**, 1119–1126 (1999).

[106] Rietveld, H. M. A profile refinement method for nuclear and magnetic structures. *Journal of Applied Crystallography* **2**, 65–71 (1969).

[107] FIZ-Karlsruhe. ICSD. URL `http://www.fiz-karlsruhe.de/icsd.html`.

[108] Exner, H. *Physical Metallurgy*, vol. 2, chap. Qualitative and Quantitative Surface Microscopy, 943–1032 (Elsevier Science BV, 1996), 4th edn.

[109] Goldstein, J. *Scanning Electron Microscopy and X-Ray Microanalysis*, vol. 1 (Springer, 2003), 3rd edn.

[110] Rühle, M. & Wilkens, M. *Physical Metallurgy*, vol. 2, chap. Transmission Electron Microscopy, 1033–1113 (Elsevier Science BV, 1996), 4th edn.

[111] Watts, J. F. & Wolstenholme, J. *An Introduction to Surface Analysis by XPS and AES* (Wiley, 2003).

[112] Gostin, P. F., Gebert, A. & Schultz, L. Comparison of the corrosion of bulk amorphous steel with conventional steel. *Corrosion Science* **52**, 273–281 (2010).

[113] Nanoscience-Instruments. URL `http://www.nanoscience.com/education/afm.html`.

[114] Davoodi, A. *Mechanistic studies of localized corrosion of Al alloys by high resolution in-situ and ex-situ probing techniques*. Ph.D. thesis, KTH Stockholm, Sweden (2007).

[115] Outokumpu. Software: HSC Chemistry.

[116] Newsam, J., Jacobson, A., McCandlish, L. & Polizzotti, R. The Structures of the Eta-Carbides Ni6Mo6C, Co6Mo6C, and Co6Mo6C2. *Journal of Solid State Chemistry* **75**, 296–304 (1988).

[117] Miller, M. K., Liu, C. T., Wright, J. A., Tang, W. & Hildal, K. APT characterization of some iron-based bulk metallic glasses. *Intermetallics* **14**, 1019–1026 (2006). 4th International Conference on Bulk Metallic Glasses MAY 01-05, 2005 Gatlinburg, TN Sp. Iss. SI.

[118] Nouri, A. S., Liu, Y. & Lewandowski, J. J. Effects of Thermal Exposure and Test Temperature on Structure Evolution and Hardness/Viscosity of an Iron-Based Metallic Glass. *Metallurgical and Materials Transactions A - Physical Metallurgy and Materials Science* **40A**, 1314–1323 (2009). MS&T 2007 Meeting SEP 16-20, 2007 Detroit, MI.

[119] Rayson, H. *Constitution and Properties of Steels*, vol. 7 of *Materials Science and Engineering*, chap. Tool Steels, 583–640 (VCH, 1992).

[120] Itagaki, M., Suzuki, T. & Watanabe, K. Anodic dissolution of Fe-Mo in sulfuric acid solution as investigated by electrochemical impedance spectroscopy combined with channel flow double electrode. *Corrosion Science* **40**, 1255–1265 (1998).

[121] Shulga, A. & Nikishanov, V. Electrochemical-corrosion properties of carbide phases. *Protection of Metals* **27**, 169–174 (1991).

[122] Gebert, A., Kuehn, U., Baunack, S., Mattern, N. & Schultz, L. Pitting corrosion of zirconium-based bulk glass-matrix composites. *Materials Science and Engineering A-Structural Materials Properties Microstructure and Processing* **415**, 242–249 (2006).

[123] Gebert, A., Haehnel, V., Park, E. S., Kim, D. H. & Schultz, L. Corrosion behaviour of Mg65Cu7.5Ni7.5Ag5Zn5Gd5Y5 bulk metallic glass in aqueous environments. *Electrochimica Acta* **53**, 3403–3411 (2008).

[124] Tobler, W. J. & Virtanen, S. Effect of Mo species on metastable pitting of Fe18Cr alloys - A current transient analysis. *Corrosion Science* **48**, 1585–1607 (2006).

[125] Asami, K., Pang, S. J., Zhang, T. & Inoue, A. Preparation and Corrosion Resistance of Fe-Cr-Mo-C-B-P Bulk Glassy Alloys. *Journal of the Electrochemical Society* **149**, B366–B369 (2002).

[126] Gaitzsch, U., Stoica, M., Gebert, A., Roth, S., Eckert, J. & Schultz, L. Electrochemical behavior and magnetic properties of the bulk amorphous Fe65.5Cr4Mo4Ga4P12C5B5.5 alloy. In *Soft Magnetic Materials, 16th Conference* (2003).

[127] Castle, J. E. & Zhdan, P. A. Characterization of Surface Topography by SEM and SFM: Problems and Solutions. *Journal of Physics D-Applied Physics* **30**, 722–740 (1997).

[128] Kapusta, S. & Heusler, K. E. Corrosion of the glassy metals Fe80B20 and Fe40Ni40B20. *Zeitschrift Fur Metallkunde* **72**, 785–791 (1981).

[129] Kaiser, H. & Eckstein, G. A. *Encyclopedia of Electrochemistry*, vol. 4, chap. Corrosion of Alloys, 156–186 (Wiley-VCH, 2003).

[130] Wagner, C. Oxidation of alloys involving noble metals. *Journal of the Electrochemical Society* **103**, 571–580 (1956).

[131] Sieradzki, K. Curvature Effects in Alloy Dissolution. *Journal of the Electrochemical Society* **140**, 2868–2872 (1993).

Publications

Publications in refereed international journals

1. P.F. Gostin, R. Sueptitz, A. Gebert, U. Kuehn, L. Schultz, *Comparing the Corrosion Behaviour of $Zr_{66}/Ti_{66}Nb_{13}Cu_8Ni_{6.8}Al_{6.2}$ Bulk Nano Structure-Dendrite Composites*, Intermetallics, vol. 16, issue 10, pp. 1179–1184, 2008.

2. P.F. Gostin, U. Siegel, C. Mickel, S. Baunack, A. Gebert, L. Schultz, *Corrosion Behaviour of the Bulk Glassy $(Fe_{44.3}Cr_5Co_5Mo_{12.8}Mn_{11.2}C_{15.8}B_{5.9})_{98.5}Y_{1.5}$ Alloy*, Journal of Materials Research, vol. 24, issue 4, pp. 1471–1479, 2009.

3. A. Gebert, P.F. Gostin, U. Kühn, L. Schultz, *Corrosion of a Zr-based Bulk Metallic Glass with Different Surface Finishing States*, ECS Transactions, vol. 16, issue 32, pp. 1–7, 2009.

4. J. Jayamani, J.M. Park, P.F. Gostin, E. Fleury, A. Gebert, L. Schultz, *Nano-Porous Surface States of Ti-Y-Al-Co Phase Separated Metallic Glass*, Intermetallics, vol. 17, issue 12, pp. 1120–1123, 2009.

5. P.F. Gostin, A. Gebert, L. Schultz, *Comparison of the Corrosion of Bulk Amorphous Steel with Conventional Steel*, Corrosion Science, vol. 52, issue 1, pp. 273–281, 2010.

6. A. Gebert, P.F. Gostin, L. Schultz, *Effect of Surface Finishing of a Zr-Based Bulk Metallic Glass on its Corrosion Behaviour*, Corrosion Science, vol. 52, issue 5, pp. 1711–1720, 2010.

7. J. Paillier, C. Mickel, P.F. Gostin, A. Gebert, *Characterization of Corrosion Phenomena of Zr-Ti-Cu-Al-Ni Metallic Glass by SEM and TEM*, Materials Characterization, vol. 61, issue 10, pp. 1000–1008, 2010.

Contributions to international conferences and workshops

1. P.F. Gostin, U. Siegel, A. Gebert, U. Kühn, J. Eckert, L. Schultz, *Corrosion Behaviour of the Bulk Glassy $(Fe_{44.3}Cr_5Co_5Mo_{12.8}Mn_{11.2}C_{15.8}B_{5.9})_{98.5}Y_{1.5}$ Alloy*, European Congress on Advanced Materials and Processes (EUROMAT 2007), 10–13 September 2007, Nuremberg, Germany.

2. P.F. Gostin, U. Siegel, A. Gebert, U. Kühn, J. Eckert, L. Schultz, *Corrosion Behaviour of the Bulk Glassy* $(Fe_{44.3}Cr_5Co_5Mo_{12.8}Mn_{11.2}C_{15.8}B_{5.9})_{98.5}Y_{1.5}$ *Alloy*, E-MRS Fall Meeting, 17–21 September 2007, Warsaw, Poland.

3. P.F. Gostin, U. Siegel, A. Gebert, U. Kühn, J. Eckert, L. Schultz, *Corrosion Behaviour of the Bulk Glassy* $(Fe_{44.3}Cr_5Co_5Mo_{12.8}Mn_{11.2}C_{15.8}B_{5.9})_{98.5}Y_{1.5}$ *Alloy*, BMG-Europe 2007, 2–3 December 2007, Paris, France.

4. P.F. Gostin, U. Siegel, A. Gebert, U. Kühn, J. Eckert, L. Schultz, *Corrosion Behaviour of the* $(Fe_{44.3}Cr_5Co_5Mo_{12.8}Mn_{11.2}C_{15.8}B_{5.9})_{98.5}Y_{1.5}$ *Bulk Metallic Glass*, The 13th International Conference on Rapidly Quenched and Metastable Materials (RQ 13), 24–29 August 2008, Dresden, Germany.

5. P.F. Gostin, S. Baunack, U. Siegel, A. Gebert, L. Schultz, *Corrosion Behaviour of the Bulk Glassy* $(Fe_{44.3}Cr_5Co_5Mo_{12.8}Mn_{11.2}C_{15.8}B_{5.9})_{98.5}Y_{1.5}$ *Alloy*, Pacific Rim Meeting on Electrochemical and Solid-State Science (PRIME 2008), 12–17 October 2008, Honolulu, Hawaii.

6. P.F. Gostin, U. Siegel, A. Gebert, U. Kühn, J. Eckert, L. Schultz, *Corrosion Behaviour of the* $(Fe_{44.3}Cr_5Co_5Mo_{12.8}Mn_{11.2}C_{15.8}B_{5.9})_{98.5}Y_{1.5}$ *Bulk Metallic Glass and Its Crystalline Counterpart*, DPG-Frühjahrstagung, 22–27 March 2009, Dresden, Germany.

7. P.F. Gostin, C. Mickel, A. Gebert, L. Schultz, *Initial Stages of Uniform Corrosion on Metallic Glasses. In-situ AFM Investigations*, European Congress and Exhibition on Advanced Materials and Processes (EUROMAT 2009), 7–10 September 2009, Glasgow, United Kingdom.

8. P.F. Gostin, A. Gebert, L. Schultz, *In-situ AFM Observations of the Early Stages of Corrosion in Fe-Based Bulk Metallic Glasses*, 216th ECS Meeting, 4–9 October 2009, Viena, Austria.

9. P.F. Gostin, U. Siegel, C. Mickel, A. Gebert, L. Schultz, *Corrosion Behaviour of the* $(Fe_{44.3}Cr_5Co_5Mo_{12.8}Mn_{11.2}C_{15.8}B_{5.9})_{98.5}Y_{1.5}$ *Amorphous Steel*, E-MRS Fall Meeting, 13–17 September 2010, Warsaw, Poland.

Acknowledgments

Firstly, I would like to express my gratitude to Prof. L. Schultz for giving me the opportunity to work at IFW and for his guidance and support.

I am very gratefull to Dr. A. Gebert for supervision, her continuous support, advice and patience. Her critical reviews are highly appreciated. These helped me very much in improving my analytical and writing skills.

Special thanks also go to Prof. M. Calin for making my coming to IFW possible.

This work would not have been possible without the help of several colleagues at IFW. I would like to mention and thank to: C. Mickel for the TEM investigations and help with the interpretation, M. Johne and K. Hennig for technical assistence in the electrochemistry laboratories, M. Gruendlich for help with metallography, Dr. S. Baunack for AES measurements and help with the interpretation, Dr. U. Siegel for sample preparation, V. Bunea for help and advice with specialized graphics software, and Dr. M. Uhlemann and Dr. U. Wolff for help with the AFM measurements.

I would like to thank for the fruitfull discussions we had: Dr. J. Koza, Dr. J. Paillier, Dr. J. Jayamani, R. Sueptitz, Dr. U. Siegel, Dr. M. Stoica, Prof. M. Branzei, Dr. U. Kuehn, Dr. K. Werniewicz, Prof. J. Payer and Dr. T. Woodcock.

I am happy to have worked and had fun with colleagues and friends at IFW, especially: Dr. Cristina Bran, Dr. Andreia Popa, Dr. Claudia Apetrii, Dr. Mihaela Bushbeck, Dr. Jorg Bushbeck, Dr. Katarjina Werniewicz, Dr. Yulia Lyubimova, Valentin Bunea and the whole department 23.

Finally, special thanks are dedicated to those who supported and encouraged me along my path to this very important point in my carrier: my father Damian Gostin, my mother Ecaterina Ivan, Ana Moisescu, Maria Filionescu, Olivia Jidveianu and Prof. Mihai Cojocaru.

Erklärung

Hiermit versichere ich, dass ich die vorliegende Arbeit ohne die unzulässige Hilfe Dritter und ohne Benutzung anderer als der angegebenen Hilfsmittel angefertigt habe; die aus fremden Quellen direkt oder indirekt übernommenen Gedanken sind als solche kenntlich gemacht. Bei der Auswahl und Auswertung des Materials sowie bei der Herstellung des Manuskripts habe ich Unterstützungsleistungen von folgenden Personen erhalten: Prof. Dr. L. Schultz und Dr. A. Gebert. Weitere Personen waren an der geistigen Herstellung der vorliegenden Arbeit nicht beteiligt. Insbesondere habe ich nicht die Hilfe eines kommerziellen Promotionsberaters in Anspruch genommen. Dritte haben von mir keine geldwerten Leistungen für Arbeiten erhalten, die in Zusammenhang mit dem Inhalt der vorgelegten Dissertation stehen. Die Arbeit wurde bisher weder im Inland noch im Ausland in gleicher oder ähnlicher Form einer anderen Prüfungsbehörde vorgelegt und ist auch noch nicht veröffentlicht worden. Die Promotionsordnung der Fakultät Maschinenwesen der TU Dresden wird anerkannt.

Dresden, den 03.11.2010

Petre Flaviu Gostin